

Award Number:
W81XWH-09-1-0410

TITLE:
Harnessing the Power of Sight to See and Treat Breast Cancer

PRINCIPAL INVESTIGATOR:
Nimmi Ramanujam, Ph.D.

CONTRACTING ORGANIZATION:
Duke University

Durham, NC 27708

REPORT DATE:
August 2014

TYPE OF REPORT:
Annual

PREPARED FOR: U.S. Army Medical Research and Materiel Command
Fort Detrick, Maryland 21702-5012

DISTRIBUTION STATEMENT: Approved for Public Release;
Distribution Unlimited

The views, opinions and/or findings contained in this report are those of the author(s) and should not be construed as an official Department of the Army position, policy or decision unless so designated by other documentation.

REPORT DOCUMENTATION PAGE				Form Approved OMB No. 0704-0188	
Public reporting burden for this collection of information is estimated to average 1 hour per response, including the time for reviewing instructions, searching existing data sources, gathering and maintaining the data needed, and completing and reviewing this collection of information. Send comments regarding this burden estimate or any other aspect of this collection of information, including suggestions for reducing this burden to Department of Defense, Washington Headquarters Services, Directorate for Information Operations and Reports (0704-0188), 1215 Jefferson Davis Highway, Suite 1204, Arlington, VA 22202-4302. Respondents should be aware that notwithstanding any other provision of law, no person shall be subject to any penalty for failing to comply with a collection of information if it does not display a currently valid OMB control number. PLEASE DO NOT RETURN YOUR FORM TO THE ABOVE ADDRESS.					
1. REPORT DATE (DD-MM-YYYY) October 2014		2. REPORT TYPE Annual		3. DATES COVERED (From - To) 18 Sep 2013 to 17 Sep 2014	
4. TITLE AND SUBTITLE Harnessing the Power of Light to See and Treat Breast Cancer				5a. CONTRACT NUMBER	
				5b. GRANT NUMBER W81XWH-09-1-0410	
				5c. PROGRAM ELEMENT NUMBER	
6. AUTHOR(S) Nimmi Ramanujam, Ph.D. go ckn'pko o kB f wngQf w				5d. PROJECT NUMBER	
				5e. TASK NUMBER	
				5f. WORK UNIT NUMBER	
7. PERFORMING ORGANIZATION NAME(S) AND ADDRESS(ES) Duke University ÁÁÁÁÁÁÁÁÁÁÁÁ ÁÁÁÁÁÁÁÁÁÁÁÁÁÁÁÁ Durham, NC 27708				8. PERFORMING ORGANIZATION REPORT NUMBER	
9. SPONSORING / MONITORING AGENCY NAME(S) AND ADDRESS(ES) U.S. Army Medical Research And Materiel Command Fort Detrick, Maryland 21702-5012				10. SPONSOR/MONITOR'S ACRONYM(S)	
				11. SPONSOR/MONITOR'S REPORT NUMBER(S)	
12. DISTRIBUTION / AVAILABILITY STATEMENT Approved for public release; distribution unlimited.					
13. SUPPLEMENTARY NOTES					
14. ABSTRACT Our objective is to exploit the wealth of physiological, metabolic, morphological and molecular sources of optical contrast to develop novel strategies that focus on two breast cancer applications: tumor margin assessment and prediction of response to neo-adjuvant therapy. The proposed aims of this grant are expected to result in three major contributions. The first has the most immediate impact. An optically based strategy that can quickly and non-destructively detect positive tumor margins will decrease the need for re-excision surgery and thereby decrease the local recurrence rate and rate of distant metastases in women electing BCS. Gaining insight into the physiological, metabolic, morphological and molecular sources of heterogeneity within and among tumors and how they are modulated by therapy, drug resistance and metastatic potential will directly benefit prognostication, prediction of outcome and planning of cancer therapies. With these tools, clinicians and clinical researchers can get a better understanding of this disease and how it might react to a drug. Basic science researchers could use it as an informed approach to study tumor biology and assay the effect of novel therapeutic agents <i>in vivo</i> .					
15. SUBJECT TERMS optical spectroscopy, imaging, fiber-optic, molecular, screening, breast cancer					
16. SECURITY CLASSIFICATION OF:			17. LIMITATION OF ABSTRACT UU	18. NUMBER OF PAGES 81	19a. NAME OF RESPONSIBLE PERSON USAMRMC
a. REPORT U	b. ABSTRACT U	c. THIS PAGE U			19b. TELEPHONE NUMBER (include area code)

Table of Contents

INTRODUCTION	4
KEY WORDS	6
OVERALL PROJECT SUMMARY	6
KEY RESEARCH ACCOMPLISHMENTS	71
CONCLUSIONS	72
PUBLICATIONS	74
PATENTS	76
REPORTABLE OUTCOMES	76
OTHER	76
REFERENCES	76

1. INTRODUCTION:

Our objective is to exploit the wealth of physiological, metabolic, morphological and molecular sources of optical contrast to develop novel strategies that focus on two breast cancer applications: tumor margin assessment and prediction of response to neo-adjuvant therapy. The proposed aims of this grant are expected to result in three major contributions. The first has the most immediate impact. An optically-based strategy that can quickly and non-destructively detect positive tumor margins will decrease the need for re-excision surgery and thereby decrease the local recurrence rate and rate of distant metastases in women electing BCS. Gaining insight into the physiological, metabolic, morphological and molecular sources of heterogeneity within and among tumors and how they are modulated by therapy, drug resistance and metastatic potential will directly benefit prognostication, prediction of outcome and planning of cancer therapies. With these tools, clinicians and clinical researchers can get a better understanding of this disease and how it might react to a drug. Basic science researchers could use it as an informed approach to study tumor biology and assay the effect of novel therapeutic agents *in vivo*.

a. Original Statement of Work for 5 Years

Aim 1: Optical imaging of margin morphology on breast lumpectomy specimens: To evaluate the role of wide-field imaging (coverage) and high-resolution interrogation (localization) of breast margin morphology to guide surgical resection intra-operatively and pathologic assessment of the tumor margin post-operatively (Timeframe: year 1-5).

- 1a. Development of one optical spectral imaging system that integrates sensing capabilities for aims 1 and 2 and a high-resolution probe that can image absorption, scattering and fluorescence contrast (timeframe, year 1).
- 1b. Conduct clinical studies on lumpectomy margins on 200 patients (time frame, years 2-4)
- 1c. Data analysis and interpretation (timeframe, years 3-5)
 - Test the sensitivity and specificity of wide-field imaging to detect positive tumor margins
 - Test sensitivity and specificity of high-resolution probe to detect IDC and DCIS.

Aim 2: Optical quantitative biology of different sub-types of breast cancer: To investigate biomarkers of oxygenation, carotenoids (β -carotene) and ECM proteins (collagen) in human breast cancer stratified by tumor sub-type and receptor status and their association with neo-adjuvant chemotherapy response.

- 2a. Development of rotating needle compatible spectroscopy probe (timeframe, year 1).
- 2b. Conduct clinical studies to measure optical biomarkers *in vivo* in 150 patients undergoing surgery (timeframe, years 2-4).
- 2c. Conduct clinical studies to measure optical biomarkers from 75 patients before neo-adjuvant therapy

2d. Data analysis and interpretation (years 3-5):

- Determine association of biomarkers with tumor subtype
- Determine association of biomarkers with receptor status
- Determine association of biomarkers with genomic signatures
- Determine association of biomarkers with pathologic sub-total and complete response

Aim 3: Optical quantitative biology to assess therapy response in different sub-types of breast cancer: To investigate biomarkers of oxygenation and ECM proteins (collagen and $\alpha_v\beta_3$ expression) in rodent breast cancer stratified by tumor sub-type, receptor status and metastatic potential in response to targeted and chemotherapies.

- 3a. To determine if multi-parametric intra-vital optical microscopy, measuring hemoglobin saturation, total hemoglobin, redox ratio, collagen, and integrin expression can monitor tumor response to tamoxifen in parental and tamoxifen-resistant MCF-7 tumors in the mouse dorsal skin fold window chamber (timeframe, years 1-2).
 - A total of 40 athymic nude mice will be required for this study (10 mice/group).
- 3b. Monitor optical parameters in the dorsal skin fold window chamber in response to doxorubicin chemotherapy in MCF-7 parental and doxorubicin-resistant tumors (timeframe, years 2-3).
 - A total of 40 athymic nude mice will be required for this study.
- 3c. Monitor optical parameters in the dorsal skin fold window chamber in response to doxorubicin chemotherapy in tumors that express high (MDA-435) and low (MCF-7) levels of $\alpha_v\beta_3$ integrin (timeframe, years 3-4).
 - A total of 40 athymic nude mice will be required for this study.
- 3d. Data and statistical analysis (timeframe, year 5).

2. KEY WORDS

optical spectroscopy, imaging, fiber-optic, molecular, screening, breast cancer

3. OVERAL PROJECT SUMMARY:

Aim 1: Aim 1: Optical imaging of margin morphology on breast lumpectomy specimens:

Aim 1 seeks to leverage diffuse optical spectroscopy as a tool for rapidly surveying breast tumor margins. Specifically, we seek to use a wide-field high-resolution diffuse optical spectroscopy device to quantify the likelihood of residual disease at the tumor excision site. Additionally, this process must be performed rapidly to afford the surgeon enough time to act on the information. Two years ago, we focused on advancing optical imaging for breast margin assessment by analyzing excisional time, cautery and patent blue dye on underlying sources of contrast in patients undergoing breast conserving surgery. The results of this study informed the development of a 49-channel device with a large field of view. An ancillary imaging platform was developed to further improve the resolution and reduce random error introduced by the user; preliminary data from this optimized system was detailed in last year's report. Here we report a further optimized system embodiment as well as an analysis of the first subset of patient data acquired using the streamlined system. Improvements were made to the light source: the thermal source was replaced with a custom 2- channel multi-colored LED system. The high-power LEDs used afford a tenfold reduction in total acquisition time. Additionally, the acquisition software was revised to provide hi-resolution real-time optical property maps: this will aid in the designation of specific sites for pathological review and device validation.

Introduction:

We have previously demonstrated that wide-field optical imaging of tumor morphology detects positive margins (margins with IDC and DCIS) with accuracies that well exceed that of the breast surgeon. Here we further refine our understanding of the micro-architectural differences between different types of tumor margin sub-types, in particular, DCIS, towards improving sensitivity and specificity. Our approach is to image the boundaries of the excised tumor mass, which is consistent with the existing paradigm for post-operative pathologic margin assessment, using the 49-channel device to acquire wide-field images of the tumor margins. We have previously shown that both radiographic breast density, as well as neoadjuvant status, impact the spectroscopic data of the surgical margins and should be considered when assessing the margin status. In this work, we investigate the influence of additional system parameters afforded by the latest generation wide-field imaging technology, such as sampling resolution and optical changes related to the pressure at the tissue-probe interface. Furthermore, we present a follow- up study based on empirical cumulative distribution functions (eCDFs) to corroborate previous findings now in the context of improved resolution. Data acquired from the first 30 patients using the hi-resolution wide-field system are analyzed and discussed.

Part A. Advancing optical imaging for breast margin assessment: (Advancements in clinical instrumentation, an analysis of the effects of resolution, applied pressure, and system reproducibility, optical property validation of the 49-channel probe)

Breast conserving surgery (BCS) is a recommended treatment for early-stage breast cancer and for breast cancers that have been reduced in size by neoadjuvant therapy. The goal of BCS is to excise the tumor along with a margin of normal tissue, while preserving as much of the normal breast tissue as possible. Unfortunately, as many as 18-72% of patients undergoing BCS require repeat surgeries due to a close or positive surgical margin diagnosed post-operatively and thus, require a re-excision surgery to achieve cancer free margins [1-9]. The large variation in re-excisions is thought to be due to differences in surgeon's training, in the definition of a close margin, and in the perceived risk of focally positive margins versus extensive involvement [10].

Surgery to remove the cancer and obtain clear margins is a collaborative effort between the surgeon and the pathologist (and in some institutions, the radiologist). In spite of this, there can be substantial variability in the prediction of positive margins in the intra-operative and post-operative settings. Surgeons do not have adequate intra-operative assessment tools to ensure that the cancer has been completely removed at the time of first surgery. Pathologists do not have adequate tools for sampling from areas on large tumor margins. The lack of these capabilities represents a significant unmet clinical need for margin assessment for both the surgeon and pathologist.

Optical imaging of tissue is an attractive solution to this problem because it is relatively fast and non-destructive. Optical techniques can also measure features related to the histological landscape without the need for labels. Before this technology can be used in an intra-operative setting or in a post-operative setting, systematic studies have to be performed to determine which surgical and post-surgical factors affect the precision and accuracy with which this technology maps optical contrast. This is true not only for our technology but other technologies, both optical and non-optical that are intended for this application.

In the following section, we review recent technological improvements to the clinical instrumentation: we have transitioned to solely using the 49-channel wide-field imaging probe described in the previous report, we have developed and integrated a robust pressure-sensitive raster-scanning imaging platform, and we have developed an efficient, multiplexed LED-based light source. We use this technology to examine the impact of the pressure at the probe-tissue interface in the context of false-positive/ false negative rates. Furthermore, we investigate the optimal scanning resolution to maximize the likelihood of detecting small regions of focal disease with intra-operative time scales in mind. We establish the optical property extraction accuracy of the wide-field 49-channel probe is to demonstrate consistency with previous generation devices. The reproducibility of the scanning mechanism is evaluated in a clinical context; repeated scans of non-diseased breast tissue are acquired in series and post operatively compared for spatial co-registration.

Methods:

Clinical Instrumentation

The latest generation clinical system consists of a desktop computer (Dell, INC, Plano, TX) custom dual-channel high-power LED source (in-house), a thermo-electrically cooled CCD and spectrograph (Andor, Oxford Instruments, PLC, Abingdon, UK), a custom raster-scanning imaging platform (in-house), and a custom 49-channel multiplexed fiber-optic probe (Zenlux Biomedical®, RTP, NC). A diagram of the system is shown in figure 1.1. The imaging probe consists of a 7x7 grid of fiber-optic channels spaced 6mm apart, each comprised of 8 illumination fibers surrounding a single detection fiber (NA = .22, d = 200 μ m). The effective coverage area is 17cm². The source-detector separation for each channel is 700 μ m. The illumination fibers for each of 49 channels are collected and subsequently bifurcated into even and odd illumination bundles such the odd and even channels of the probe can be illuminated independently. A sequential illumination pattern of the odd and even channels is used to reduce inter-pixel crosstalk.

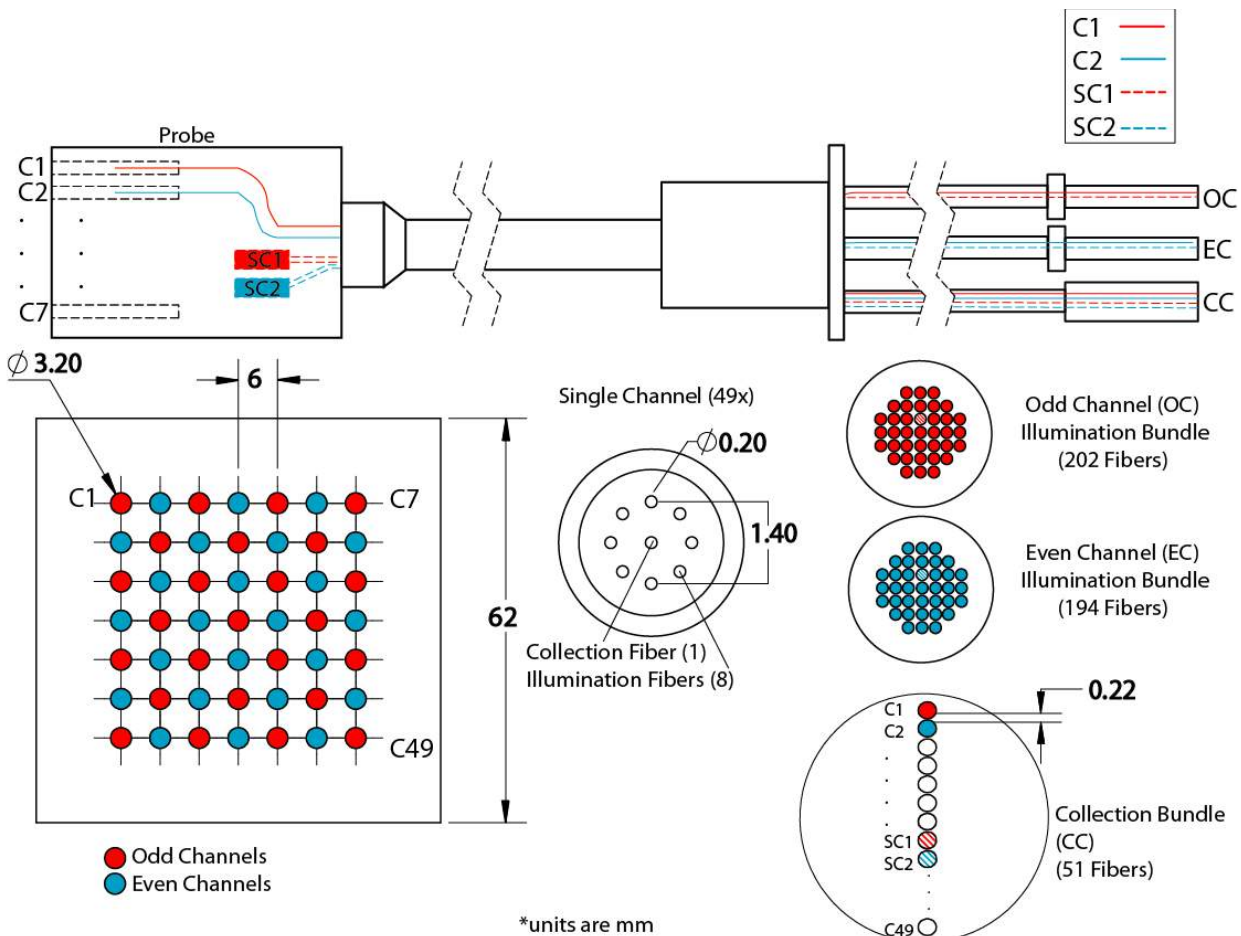


Figure 1.1 Probe Detail. Each of the 49 channels consists of a single detection fiber and 8 illumination fibers. Illumination fibers are collected and bifurcated into two fiber bundles (OC and EC) corresponding to odd (red) and even channels (blue). The 49 detection fibers are ordered in a linear array and imaged onto the CCD and spectrograph (collection bundle)..

A custom raster-scanning imaging platform was developed to improve the sampling resolution of the 49-channel device in a controlled fashion. This is achieved by incrementally translating the probe in both lateral directions using precision stepping motors and subsequently translating the probe downward to establish contact with the specimen, which is placed atop a base with pressure sensors that are continuously polled by the acquisition algorithm. In total, the imaging platform consists of a pressure sensitive base utilizing 4 discrete force sensors, a mechanism to physically hold the probe, and a custom computer controlled XYZ scanning mechanism. The scanning mechanism can reproducibly (within 1%) move the probe in each direction in increments of $10\mu\text{m}$ or greater at a rate of $.5\text{s/mm}$; providing an avenue to raster-scan samples on intra-operative time scales. A cartoon of this system setup is observed in figure 1.2.

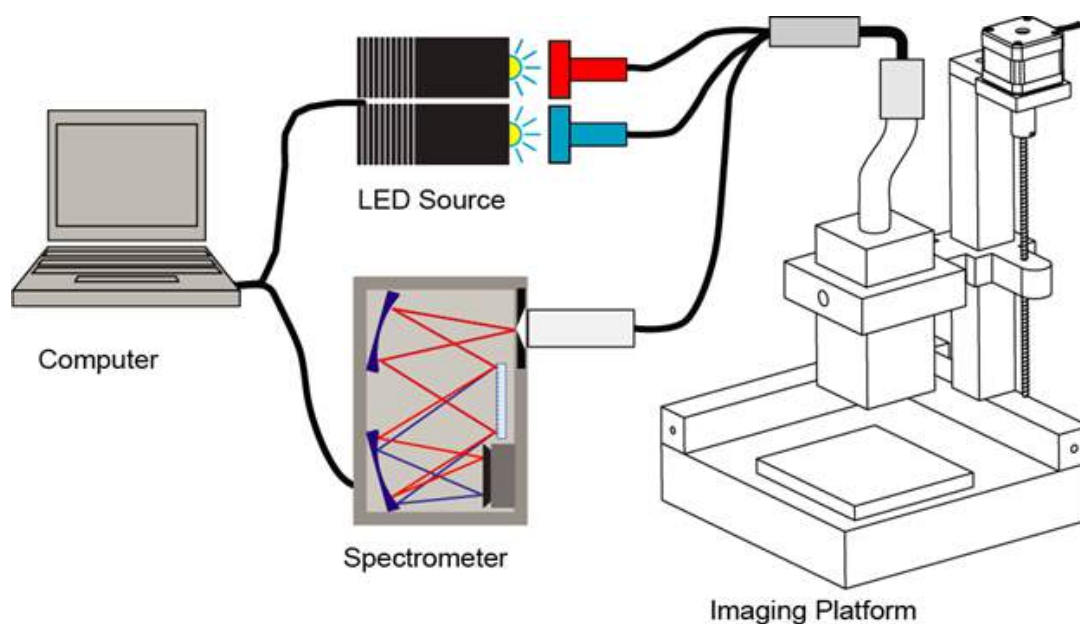


Figure 1.2 System Overview. The custom imaging platform, spectrometer, and dual channel LED source are each interfaced to the computer via USB. Located just below the probe is a pressure sensitive base on which the specimen is placed just prior to the initiation of the raster-scanning sequence. Channels 1 and 2 of the LED source illuminate the odd and even channels in sequence, respectively. Diffuse reflectance data is collected for each of the 49 channels during both scans.

A dual-channel LED source was developed to reduce total acquisition time and to increase the light source efficiency. Previously, a Xenon thermal source was used alongside a mechanical optical switch requiring a minimum of 5 seconds to toggle between channels. The new, improved source consists of two identical LED modules; each module contains two cool-white high-power LEDs (CREE, INC, XP-G2, Durham, NC), a green LED ($\lambda_c = 510\text{nm}$), and a blue LED ($\lambda_c = 470\text{nm}$) (Luxeon Star LEDs, USA). These four discrete LEDs were chosen to provide near-spectrally flat white light, an option currently not available using a single commercial LED. The improvement in speed is realized by the fact that these modules need

only be toggled off/on, avoiding the 5 second delay required by the mechanical switch. Furthermore, the LED modules improve the SNR of the system by eliminating the highly variable thermal source (7-15% variation). An improvement in efficiency is also realized due to both the higher efficiency of LEDs and the pulse-like use of the LEDs (the thermal source must remain on continuously for stability). Each of the 4 discrete LEDs in each module are coupled to a respective illumination bundles using a hexagonal polycarbonate concentrating lens (Polymer Optics, LTD, UK). The first segment of each illumination bundle consists of a liquid light guide which serves to uniformly spatially distribute the light from each of the 4 LEDs. A microcontroller based mechanical relay control unit is used to interface the computer and selectively power each LED; power toggling eliminates the possibility of stray light influence from opposing channels. The reproducibility of light intensity for this source was determined by acquiring 25 sequential measures using the 99% reflectance target at 10 separate integration times corresponding to dynamic range of the CCD. The maximum variation observed was less than 2%.

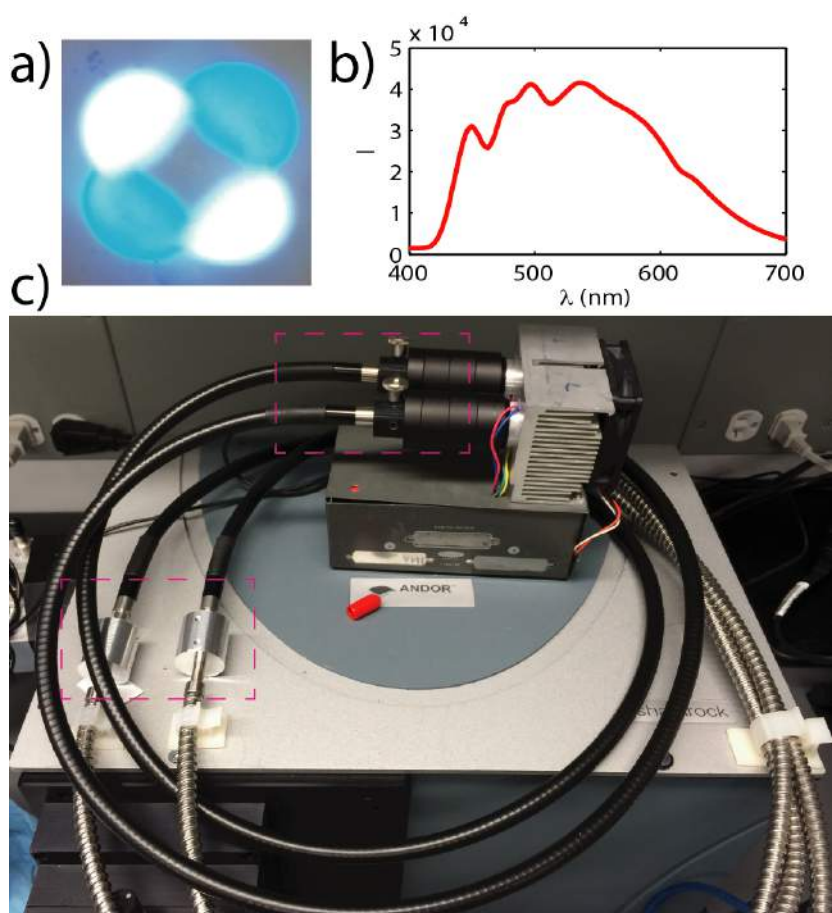


Figure 1.3 LED-Based light source a) Digital photo showing color output before mixing. b) Mixed spectral output from 400-630nm. c) LED system with boxed regions to illustrate the illumination bundle/ mixer interfaces.

Effects of Pressure and Resolution Enhancements

Raster-scanning resolution was established using a printed 1951 USAF resolution target placed atop a Spectralon target and a pliable scattering medium. The target was then measured as a function of upsample factor, hereafter referred to as (n); which is a measure corresponding to the number of evenly spaced locations between neighboring pixels. For example, an $n = 6$ would correspond to 36 (n^2) placements of the entire probe in increments of 1mm (6 measurements between 6mm spaced channels) in both the x and y directions. Each of the two samples were measured at $n = 10, 8, 5, 4, 3, 1$.

To determine the effects of pressure, we developed a layered meat model to simulate a margin-like structure. The top layer is comprised of half fat and half smooth muscle the lower layer a highly absorbing red meat, some fat is present. We placed the thin layers (bacon) on top of the meat, as illustrated in the cartoon in figure 1.4. The probe was oriented such that half of the pixels correspond to the muscle half of the top layer, while the other half was used to survey the fatty (scattering) region. We repeated this experiment for two margin thicknesses, 2 and 4mm, achieved by stacking multiple top layer samples.

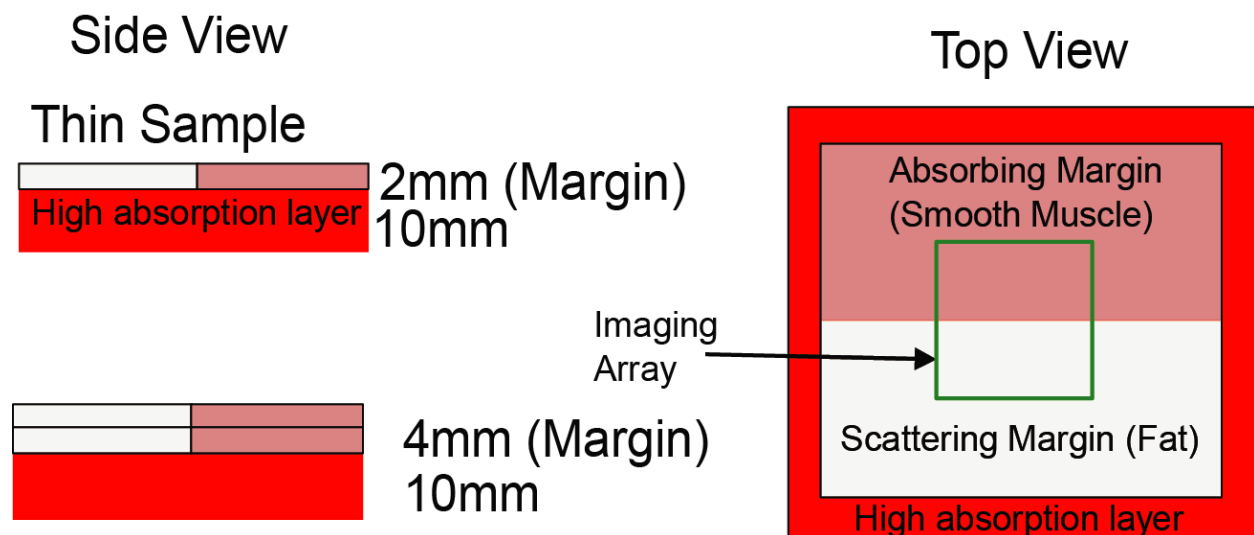


Figure 1.4 Pressure testing assay. Two margin thicknesses are simulated using meat samples with a well-defined thickness. A high-absorption thick layer rests beneath a half-scattering half-absorbing layer and serves as a source high contrast to reveal compression of the top layer.

Diffuse reflectance was recorded over a range of applied pressures in 2mmHg increments up to 16mmHg. These spectra were then inverted to obtain the constituent optical properties relevant to the samples, in this case the concentration of hemoglobin (from the absorption coefficient) and the reduced scattering coefficient, μ_s' .

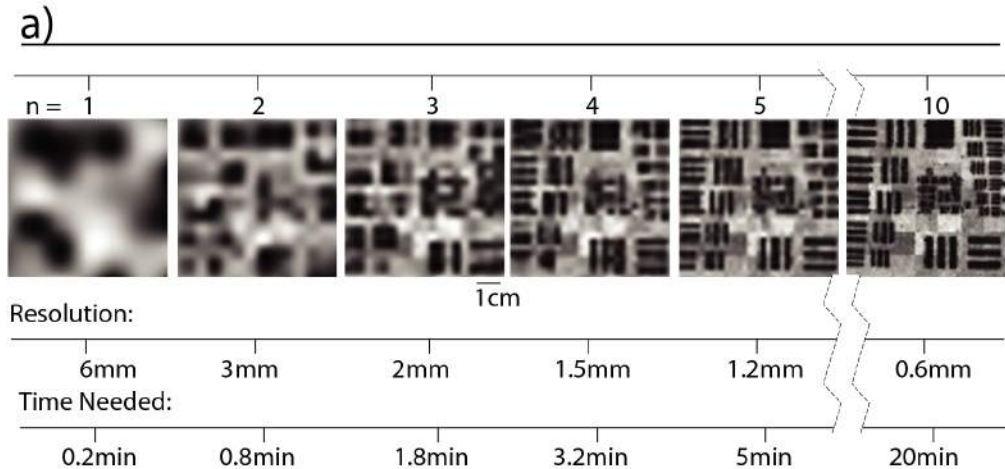
Optical Property Extraction Validation

Tissue simulating phantoms were constructed to determine the optical property extraction accuracy of the scaled Monte-Carlo reference simulation modeled for the device geometry. The phantom study was designed according the methods and protocol vetted by Bender *et al*[11] and Palmer *et al*[12, 13]. Tissue scattering and absorption were simulated using 1 μ m polystyrene microspheres (Polysciences, INC) and isolated ferrous hemoglobin (Sigma-Aldrich, INC), respectively. A total of 12 phantoms were constructed: concentrated hemoglobin was added in increasing volume 11 times to a base non-absorbing phantom with average $\mu_s' = 9.2 \text{ cm}^{-1}$ ($\lambda = 420\text{-}630\text{nm}$), resulting in average μ_a values ranging 0 to 15 cm^{-1} . Ten repeated diffuse reflectance spectra were collected for all channels for each of these 12 phantoms (1 non-absorbing, 11 absorbing). The mass of each constituent was measured and recorded at each step of the phantom fabrication process to reduce systematic and random error associated with pipetting and changes in density caused by temperature fluctuations. Likewise, the phantoms were thoroughly mixed just prior to being measured to reduce the effects of solution settling.

The inverse Monte-Carlo model previously developed by our lab was used to invert diffuse reflectance spectra to constituent optical properties (μ_a and μ_s')[11-13]. Briefly, the Monte-Carlo model utilizes a non-linear least squares fitting routine to best match a corrected reflectance spectrum to a Monte-Carlo generated reflectance look-up table generated based on the source-collection geometry and optical characteristics. Reflectance spectra are scaled by calibrating to a reference phantom with known optical properties; this, alongside a Spectralon measurement to account for the wavelength dependent source intensity, account for the entire system-specific response. A leave-one-out cross validation analysis was performed using each of the 12 aforementioned tissue simulating phantoms wherein each phantom was tested as a reference phantom against the remaining 11. Extracted values for μ_a and μ_s' were analyzed as percent error relative to the expected values for each phantom/reference phantom combination.

Results:

The optimal raster-scanning upsample factor was determined to be 8: a full scan of a single margin can be acquired in less than 15 minutes (12.8mins) at a resolution better than 1mm (.75mm). Figure 1.5 illustrates the tradeoff between resolution and time and additionally provides a meat-based example to demonstrate the clear benefit of sub-pixel sampling. Considering breast tumor margin assessment, resolution greater than 1mm is warranted to increase the probability of detection of focal disease. Small regions of focal disease are particularly important to discover as standard of care stipulates that partial mastectomy specimens be sliced at 5mm increments for histological preparation.



Sub-pixel sampling example:

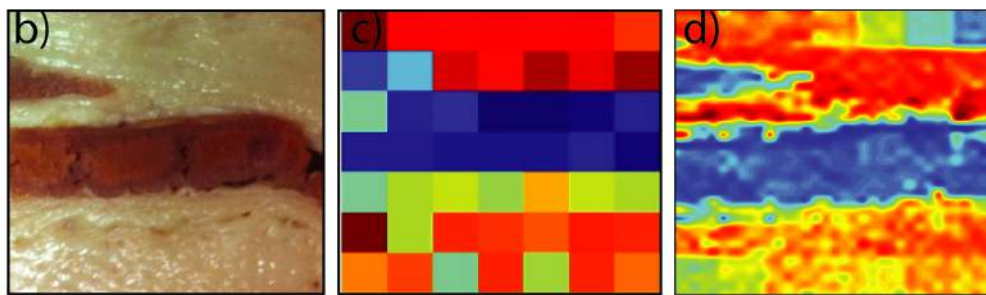


Figure 1.5 Raster-scanning Metrics. a) The tradeoff between resolution and time as a function of upsample factor for $n = 1, 2, 3, 4, 5$, and 10 . Scanned images are average reflectance values (405-630nm) measured on a resolution target (USAF 1951) with a diffuse background. b) Digital image of a meat sample with well-defined predominantly scattering and absorbing regions. c) A single diffuse reflectance acquisition averaged over 405-630nm. d) A raster-scanned image of the meat sample taken at an upsample rate of 5.

No significant difference was found for resolution target measurements taken with a diffusive (scattering) medium as the background compared to those taken with the Spectralon target as the background medium. As observed in figure 1.5, the improvement in resolution additionally provides well-defined structural information for optical property and spatial co-registration, which is useful when comparing parameter maps to actual digital images.

The effects of pressure are well demonstrated using previously described meat model to simulate a margin-like sample. Figure 1.6 indicates that for the 2mm margin, there is a narrow pressure window in which the extracted optical parameters are valid. The change between 5 and 10mmHg represents the point at which contact is established, and the change between 10 and 15mmHg represents the point at which the margin is compressed enough that you begin to sense the high-absorption layer, in this case red steak, causing the reduced scattering coefficient to be diminished. These changes are not as obvious in the absorbing region of the top layer due to the inherent absorption of the top layer; however, there is still a marked increase in measure [Hb] beyond 15mmHg, suggesting that the highly absorbing bottom layer

can still be detected in the presence of absorption in the top layer. The effects of compression are not realized in the thicker top layer specimen within the range of pressure investigated.

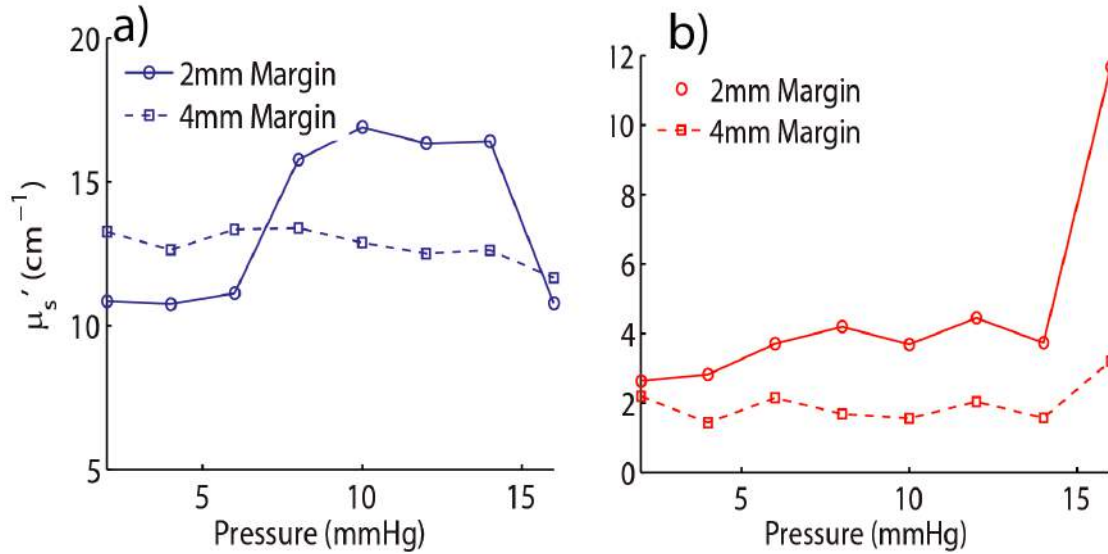


Figure 1.6. Effects of pressure. a) Changes in the reduced scattering coefficient as a function of pressure and b) the corresponding changes in the absorption coefficient.

The optical property extraction accuracy was determined to be within 8% of the expected values for μ_s' and μ_a for the entire span of phantoms measured. Figure 1.7 illustrates optical property extraction accuracy by displaying extracted values as a function of the expected values.

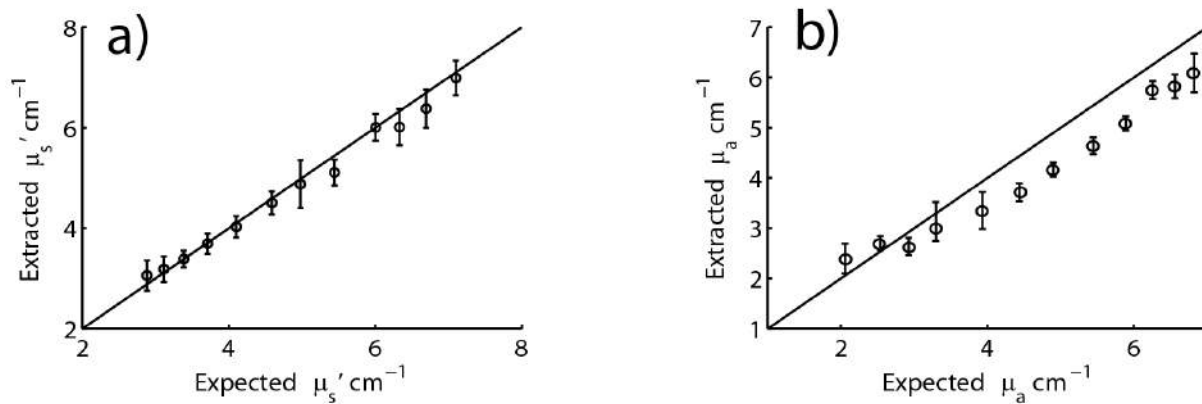


Figure 1.7. Expected vs. Extracted Optical Properties. Scatter plots of the known versus the measured values of μ_a (a) and μ_s' (b) for the phantom study set. The diagonal line indicates perfect agreement.

We have previously established error within 10% as acceptable for clinical use as statistically significant differences can be realized within this range[14]. The 49-channel wide-field probe is thus equivalently or better suited for clinical use.

Part B. Clinical Study on Margin Assessment:

In previous reports, we saw a substantial proportion of margins (1.5 on average) that presented as positive under pathological review. At Duke University Medical Center (DUMC) the treatment paradigm has significantly changed in the last two years and that number has substantially decreased. The complications associated with small, focal regions of cancerous cells at the margin edge however, remain. Moreover, these regions of positivity are unlikely to be discovered within the current clinical framework; pathologists typically sample lumpectomy specimens at 3-5mm intervals for histopathological review, leaving a substantial risk for these small regions to go undetected. The challenge for any intra-operative technique for breast tumor margin assessment is the ability to detect the signal (i.e., the histologic changes due to varying amounts of malignancy at the margin) over the noise (i.e., the normal inter-patient and intra-patient variation in breast composition). If we view the range of normal tissues in the breast as a “landscape,” then the challenge in margin assessment is to detect the presence of malignant tissue at the boundary of an otherwise “normal” margin, as a perturbation in that landscape. The clinical challenges thus warrant a device capable of both a wide coverage area as well (to survey the entire margin) and small feature recognition (to avoid missing focal regions of cancer).

We previously reported on our first generation 49channel+scanning platform device to address the under-sampling/coverage obstacles, wherein optical parameter maps were shown for an oversampled positive and negative margin. As described in the previous section, the technology has extensively matured with the capability extended to automatic digital images, precise automatic positioning, enhanced load bearing, and optimized pressure sensing. The goal of these enhancements was to further reduce systematic and user error, improve the acquisition speed and thereby sampling resolution, and to understand the effects of resolution on the ability to detect small regions of disease. In this section, we present a quantitative analysis of the hyperspectral image landscapes collected using this high-resolution device on a cohort of 30 patients.

Methods:

Patient Data Collection

Diffuse reflectance spectra were collected from excised breast tissue specimens from 30 patients. For the purposes of this work, patients undergoing breast conserving therapy (BCT) as well as breast reduction surgery were recruited. Specimens (partial mastectomies and reduction mammoplasties) from the respective patient populations were used to compare the optical property values corresponding to dysplastic tissue (partial mastectomy specimens with a positive or close margin), normal tissue (reduction mammoplasty specimens without dysplasia), and additionally normal tissue in the presence of dysplasia (partial mastectomy specimens with negative margins). Partial mastectomy specimen orientation was determined according to surgically placed reference features including: a surgical wire inserted into the center of the tumor, colored sutures, and surgical clips. Specimen faces were defined as the faces of a cube and labeled relative to the specimen orientation in situ; the six measureable faces are hereafter referred to as the superior, inferior, posterior, anterior, medial, or lateral margin. Reduction

mammoplasty specimens do not have such a reference system as they are typically not sent to post-operative pathology for assessment.

Immediately following the tissue resection, partial mastectomy specimens are sent to radiology for an intra-operative x-ray examination to verify successful removal of the intended tissue. Upon return, the specimen is then placed onto the pressure sensing base of the imaging platform and oriented accordingly. The raster-scanning procedure is initiated and diffuse reflectance spectra are collected across the visible spectrum (400-700nm). The pressure applied to the face of the specimen is dynamically controlled by a feedback loop that executes in parallel to the main acquisition software, such that subtle adjustments to the applied pressure can be made without interrupting spectrum collection. The specimen is then flipped to its opposing margin and the scan is initiated a second time. Once scanning is complete, a “site-level” inking procedure is performed wherein 6- 10 sites are marked using tattoo ink (typically orange in color) with the aid of a co-registration structure that physically relays the central location of each channel to specimen. The co-registration plate is then removed and the four corners of the margin are then marked with a different color ink (typically green). A certified pathologist uses these inked dots to provide site-level (orange dots) and gross margin level (green dots) histopathological correlation to the collected spectral channel data. Margin inking was followed by the acquisition of a digital image using an on-board digital camera mounted to the imaging platform.

Clinical Data Processing

Partial mastectomy specimens were measured on the posterior or anterior margins: the pancake-like shape of the excised tissue limited measurements to only two margins. The measurement order is determined *ad hoc* as it is not possible to measure a margin multiple times due to time restrictions, nor is it possible to know with certainty the margin that has the highest likelihood of positivity. A single margin was inked for post-operative pathological assessment in a uniformly spaced diamond pattern. Over the next year, sites will be inked according to the likelihood of being cancerous as designated by our discriminatory algorithm. For this patient data set, tissue optical property maps were reconstructed post-operatively using the inverse Monte-Carlo model discussed previously.

A dual arm cumulative distribution function (CDF) analysis was performed at the margin level, including all measured samples, and at the site-level, where parameter values corresponded only to regions marked for histological validation. The ability of our spectral mapping technique to survey shifts in of the morphological features of the normal breast was determined by analyzing the spectral information arising from inter-patient variations in mammographic breast density (MBD), which further established the morphological features to which the hyperspectral maps are sensitive. A two-sided Kolmogorov-Smirnov statistic p-value was used to determine if tissue-specific optical parameter distributions were from a common parent distribution, effectively summarizing our ability to categorically discern tissue subtypes. A conditional inference tree model (CIT) previously reported by our group [15] was used to further stratify tissue margins high and low breast density subgroups (HBD and LBD, respectively).

Patient Population

The following characteristics were recorded for each patient (if available): radiographic breast density, menopausal status, neoadjuvant treatment status (chemotherapy or endocrine therapy), age, body mass index (BMI), and surgical re-excision status. For the analyses presented herein, data was only included from patients who had not undergone prior radiation, adjuvant treatment, or surgery 1) due to limited sample sizes and 2) in order to assess differences in surgical margin status without these additional confounding factors. For mammographic breast density (MBD), each patient was assigned a value based on their pre-surgery mammogram: 1 (fatty), 2 (scattered fibrous), 3 (heterogeneously dense), or 4 (extremely dense). For the analyses in this paper an MBD score of 1 or 2 was considered to be low density, while a score of 3 or 4 was considered to be high density; the data was binned this way since the majority of the patients had 2's or 3's.

Results:

Clinical Imaging

Clinical raster-scanned images were acquired for 30 patients at an upsample rate of 8, resulting in 64 full frame spectral images (3136 full spectrum pixels) for each margin measured. A representative case is shown in figure 1.8. Average collection time for each margin image was ~12minutes; a few minutes are needed for the inking procedure. Of the 6 possible margins, 2 were measured (anterior/posterior) in most cases due to the pancake-like shape of most specimens.

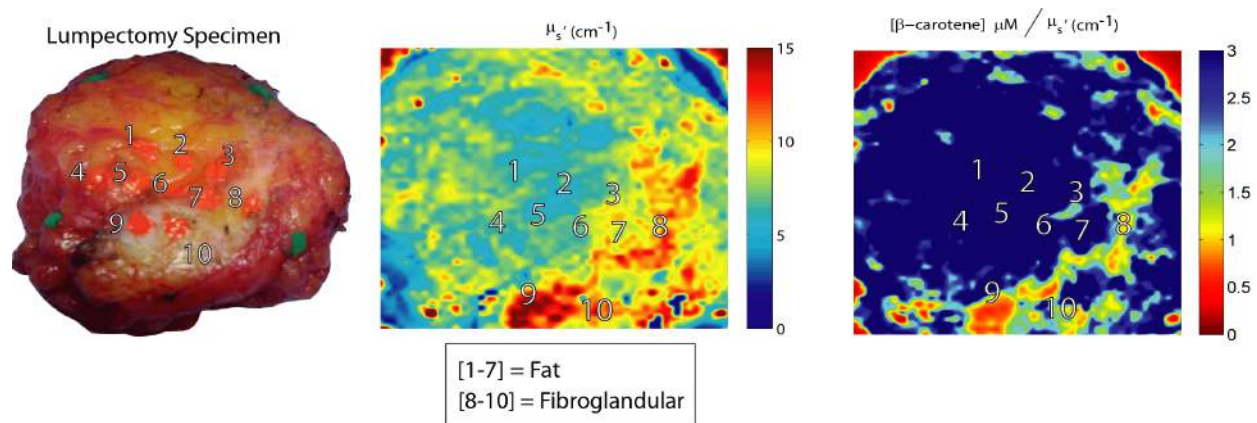


Figure 1.8 Representative clinical hi-resolution image. a) Digital photo showing inked sites. b) Raster-scanned reflectance image averaged from 430-630nm. c) Upsampled optical property map of $[\beta\text{-carotene}]/\mu_s'$. Sites labeled 1-6 (b) mostly contain fat, sites 7-10 are mostly fibroglandular tissue.

The ratio of $[\beta\text{-carotene}]/\mu_s'$ has previously been established by our group as the most valuable diagnostic parameter. In figure 1.8, the fibroglandular features are readily seen in the lower right of the $[\beta\text{-carotene}]/\mu_s'$ parameter map. Note that this region is also observed in the digital image taken with a webcam.

The utility of resolution enhancement is further demonstrated in a clinical context in figure 1.9. Moving from left to right and top to bottom, it is clear that optically relevant features are substantially obscured in the lesser upsampled images, as well as the native 49-channel probe image. This is important in the context of small regions of focal disease; cancerous features may not be discernable when volume averaging using the native 6mm probe resolution.

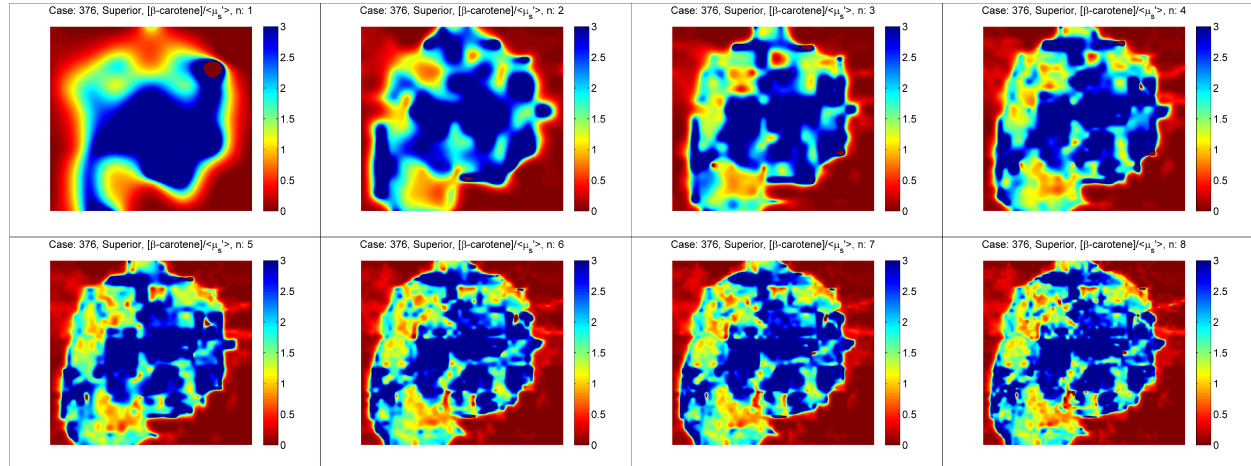


Figure 1.9 Representative downsampled images. The top left frame represents the interpolated (50x bi-cubic) parameter map of the native probe. Moving from left to right and top to bottom, the upsample rate increases from 1- 8. The final image is comprised of 64 separate full frame parameter maps.

Data Analysis

The relationship between optical parameters and benign breast tissue composition has been well established by our group in prior publications [15, 16]. Briefly, it has been determined that the ratio of $[\beta\text{-carotene}]$ to $\langle\mu_s'\rangle$ decreases as the tissue changes from predominantly adipose tissue to predominantly fibroglandular tissue components. This manifests as a left shift of the empirical CDF corresponding to all pixels with a given $[\beta\text{-carotene}] / \langle\mu_s'\rangle$ parameter map. Furthermore, the ability to quantify and distinguish these changes is greatly enhanced the patient population is stratified by breast density. In this study, we sought to replicate these results using a 30 patient cohort of benign tissue margins. Positive margins were not considered due to the extremely low incidence of positive margins currently seen at DUMC. Figure 1.10 shows representative HBD and LBD samples as well as the corresponding eCDFs.

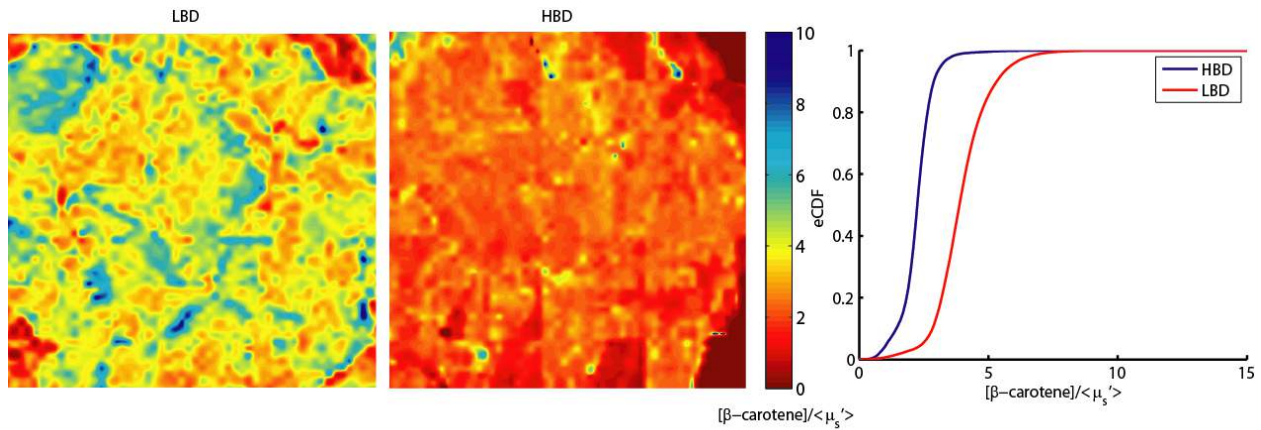


Figure 1.10 Optical differences in benign breast tissue associated with density. From left to right, a full margin image (map of $[\beta\text{-carotene}]/\mu_s'$) of a low breast density sample, a full margin image of a high breast density sample, and the corresponding cumulative distribution functions.

The lower $[\beta\text{-carotene}]/\mu_s'$ values can be explained by the proportions of tissue typical to these breast density grades. Low density breasts are likely to have higher proportions of fatty tissue and therefore present with a naturally higher β -carotene concentration (thereby increasing the ratio). Likewise, high density breasts have higher proportions of collagen and glandular tissue, which manifests as an increase in the scattering signal. These effects are well summarized by the directional shift of the eCDFs: fatty tissue associated with the LBD margin has shifted the curve to right, fibrous tissue has shifted curve corresponding to the HBD margin to the left. Figure 1.11 shows the eCDF trends for the entire patient cohort.

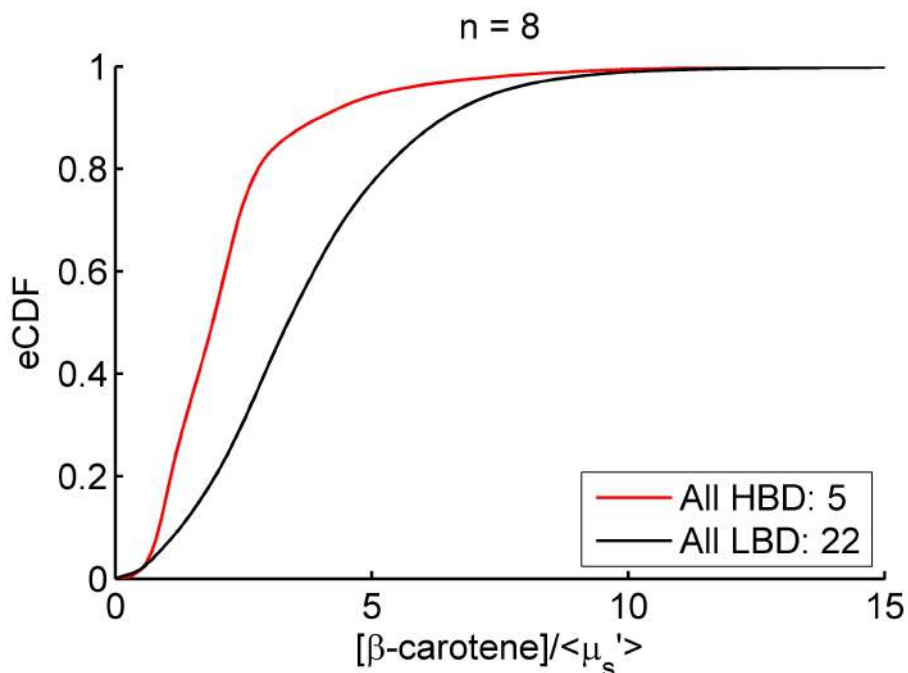


Figure 1.11 Combined CDFs for all low and high breast density samples. Empirical cumulative distribution functions (eCDFs) of all margin level data for all high and low breast density samples.

The Kolmogorov-Smirnov (KS) test was used to determine if these distributions are statistically likely to originate from a common underlying distribution. The KS test considers both the shape and size differences when comparing distributions, and is often used in the context of CDFs to quantify the distance between an empirical and a cumulative distribution function and can be considered a goodness of fit. HBD and LBD margins were found to be statistically different ($p < .02$) at the margin level for the cohort used in this analysis.

We performed a similar analysis at the site level using all available pathology-confirmed sites from the same patient data set. Site designations with $n < 5$ were excluded from this analysis due to insufficient statistical power. Of the 128 selected sites, 71 were primarily composed of fat (labeled adipose), 5 were a mixture of fibrous tissue and fat tissue (fibroadipose), 9 were a mixture fibrous and glandular tissue (fibroglandular), 31 were a mixture of fat and fibroglandular tissue, 6 sites included regions of DCIS 1-3mm from the margin surface, similarly 6 sites included some invasive carcinoma .1 to 3mm from the surface. We chose to augment our analysis of site-specific distribution dependencies by also investigating how these change when lower/higher resolutions are used. Figure 1.12 shows the site level CDFs for each of these tissue compositions at the highest and lowest resolution used in this study (.9mm/6mm).

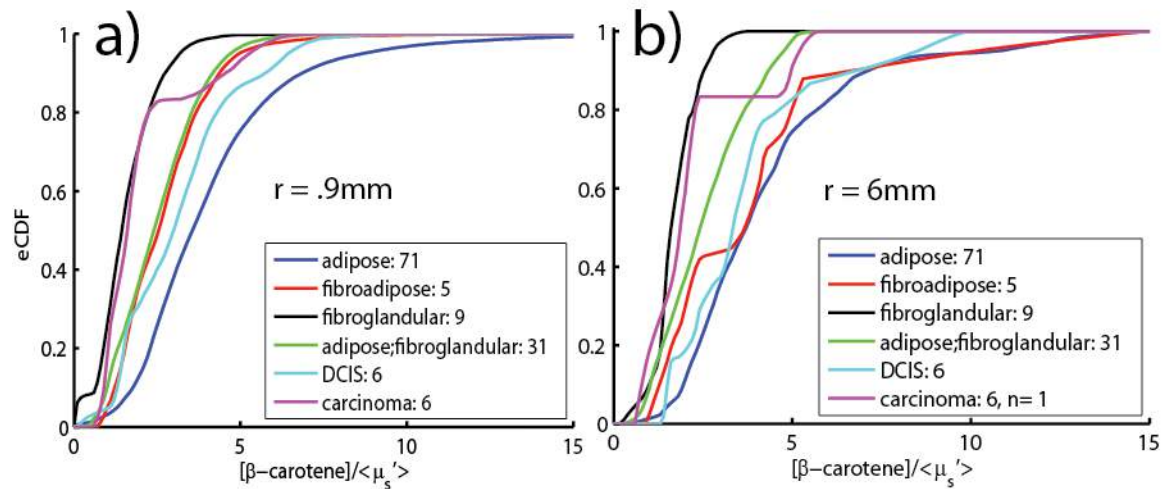


Figure 1.12 eCDFs for all site-level data. Empirical cumulative distributions for eligible pathology confirmed tissue sites. a) corresponds to distributions taken with the highest upsample ($n=8$) and correspond to the best resolution (.9mm) and, b) represents the corresponding distributions measured using the native probe resolution (6mm).

Not surprisingly we discovered that as the adipose content is increased, the CDF tends to shift to the right. At the highest resolution used, each of these tissue subtypes are statistically distinct from one another, with the exception of fibroglandular and “carcinoma” tissues ($p > .0001$). Interestingly, adipose tissues are statistically different from fibroadipose tissues at the highest upsample ($p < .0001$) but not at the lowest, suggesting that the signal from fibrous components are washed out at low resolution. Similarly, fibroglandular tissue is no longer distinguishable from the fibroglandular/adipose mix as you decrease in resolution. The inability to distinguish pure fat from other tissue types suggests that sub-pixel sampling is imperative to accurately diagnose the margin landscape moving forward

Plans for year 6: In year 6, we will primarily focus on patient accrual and the development of the diagnostic algorithm in the context of our hi-resolution device. We will build on our current CIT model to optimally separate tissue subtypes and to select sites chosen for pathological validation.

Aim 2: Optical quantitative biology of different breast cancer subtypes.

Part A – Duke University

The objective of the work in Aim 2 is to use optical techniques to measure markers of the tumor microenvironment in women with cancers representing a wide variety of subtypes, and to determine whether these optical measures can be used for real time diagnosis or to predict eventual chemotherapy response in a subset of the patients who are measured prior to commencement of chemotherapy. One such approach that we have discussed in previous years is to use a high resolution microendoscope (HRME) combined with a morphological stain called acriflavine to visualize the tissue morphology in real time. In previous years we demonstrated the feasibility of using the HRME for detection of residual carcinoma in the normal tissue milieu and validated our unique image analysis approach on preclinical murine tumor margin specimens and small cohort of clinical mastectomy samples. We also completed a large study using the HRME to capture morphologically based information from biopsy specimens. Here we focus primarily on our quantitative approach for diagnosing HRME images of heterogeneous breast tissue acquired from biopsy specimens. In Year 5, we continued to image biopsy specimens, have identified several quantitative endpoints to distinguish malignant from benign tissues, and have built an initial diagnostic classification model.

Microscopy is a powerful technique that can provide visualization of tissue morphology at the point of care. Various microscopy techniques including reflectance and fluorescence [17-21], confocal [22-26], and optical coherence tomography [27-32] have been used to visualize micro-anatomic tissues at the point of care, much like what a pathologist visualizes when looking at tissue sections. Previously, our group used a high resolution fluorescence microendoscope in combination with a topical contrast agent called acriflavine to enable visualization of the microanatomical features in resected tumor surgical margins [33]. This study was carried out using genetically engineered mice with conditional mutations in *p53* and either *K-ras* or *B-raf* after they developed primary sarcomas [34, 35]. A primary sarcoma model was chosen because

it more closely mimics the tumor invasion into adjacent skeletal muscle found in human sarcomas as compared to xenograft models. We developed a strategy for isolating nuclei from the heterogeneous sarcoma margins, using a technique called sparse decomposition (SD) [33], which has been used in the image processing community for image compression, enhancement, and restoration. The SD image processing algorithm was first optimized through using simulations of mouse tumor, muscle, adipose, and tumor + muscle tissues and then using tested on images of excised sarcoma margins in mice [33]. SD accurately isolated nuclei from images of tumor, muscle, adipose, and tumor + muscle tissue types and differences in both nuclear density and size could be leveraged to identify pathologically confirmed positive tumor margins as verified with pathology [33].

The goal of our current study was to test the robustness of our quantitative microscopy tool box to detect the presence of malignancy in breast biopsies. A logistic regression model optimized on individual pure images for which we had a corresponding pathology diagnosis was validated on an independent testing set and then prospectively applied to the panel of images obtained from the breast biopsies. The sensitivity and specificity of site level imaging for differentiating positive from negative images was 100% and 84%. When applied prospectively to biopsy mosaics the sensitivity and specificity was 73% and 65%, respectively. These results indicate a robust approach for the detection of microscopic disease. This method is particularly well suited for applications to different organ sites given that (1) it leverages the micro-anatomical changes in pathological tissue and (2) it can be applied to highly heterogeneous tissues consisting of multiple tissue types.

Methods:

Imaging system and contrast agent: A high resolution fluorescence microendoscope that has been described previously [36] was used to capture images of sarcoma margins. Briefly, the microendoscope contained a 455 nm light emitting diode, excitation filter, dichroic mirror, 10x objective, emission filter, and CCD camera. The light was directed to the sample through a flexible fiber bundle composed of 30,000 fibers that yielded a circular field of view of approximately 750 μm in diameter. The resolution of the system was approximately 4.4 μm . The system was optimized to be used for use with a contrast agent called acriflavine, which reversibly associates with nucleic acids, such as RNA and DNA, and has also been shown to stain muscle fibers and collagen [37, 38]. Acriflavine was dissolved in phosphate buffered saline solution (0.01% w/v, Sigma-Aldrich) and was topically applied to the tissue immediately before placing the fiber bundle in contact with the tissue and acquiring images.

Imaging protocol: Patients undergoing a biopsy procedure at Duke University were consented. After the biopsy was removed from the patient, acriflavine was applied to the surface of the specimen. The distal end of the HRME fiber bundle was placed in contact with the tissue and images were acquired. The biopsy was scanned length-wise by systematically moving the probe in 1 mm increments over the tissue surface. Once one side was scanned, the biopsy was rotated 180 degrees and the length-wise scanning process was repeated. In order to improve the accuracy and reproducibility of these movements the fiber bundle was secured in a custom

probe holder fiber chuck which was mounted on an x-y translation stage. Between each probe placement the distal end of the probe was cleaned with 55% ethanol.

Pathologic co-registration: After the imaging session the surface of the specimen was inked for pathologic co-registration. In order to maintain the proper orientation of the specimen for pathological evaluation, each end was inked with a different color. After imaging and inking was complete, the tissue was returned for standard pathologic processing, and the resulting hematoxylin and eosin (H&E) stained slides were reviewed by an expert oncology pathologist who was blinded to the results of HRME imaging. A diagnosis for each end of the biopsy as well as a diagnosis for the middle portion of the biopsy was given.

Sparse decomposition (SD) for nuclei segmentation: All image processing and analysis was completed in MATLAB (2013b, Mathworks Inc., Natick, MA). Images were cropped in order to discard the rim of the fiber bundle. Additionally, a low pass Gaussian filter was applied to remove the fiber core pattern that was superimposed onto the images. Next nuclei were segmented through applying a technique called sparse decomposition (SD), which has been described previously [33]. Briefly, SD is a computational technique that leverages the morphological information present in the fluorescent images of acriflavine stained microanatomy and separates distinct structures into mathematically discrete components. SD was used here to separate nuclei from muscle and adipose structures in heterogeneous images. The key assumptions were that (1) each tissue type has a different dictionary in which it can be represented sparsely and (2) if the dictionaries are dissimilar enough, then sparsity can be used to separate the different tissue components. For example, the spatial (or pixel) dictionary was used to capture nuclei because nuclei are small and spatially sparse. The discrete cosine transform (DCT) dictionary, which is a variant of the Fourier transform, was used to capture fibrous components because fibrous tissue is characterized by periodic fibers. Lastly, the curvelet dictionary was used to capture the outlines of adipose cells because adipose cells are characterized by smooth localized curves [39].

After SD was applied to isolate nuclei, variables such as the nuclear size and density were quantified by computing the circle transform [40] (CT) to detect approximately circular objects (i.e. nuclei). CT was chosen to quantify nuclear variables because it can distinguish overlapping circular nuclei and is easy to tune.

Calculation of nuclear variables: Nuclear variables were designed to capture features that pathologists typically use to distinguish between normal and diseased tissue. Diseased features typically include increased nuclear density or clusters of nuclei and pleomorphism (the variation in size and shape of nuclei) [41, 42]. Specifically nuclear variables include nuclear density (abbreviated as density), which is the number of nuclei in a specified area, and nuclear diameter (abbreviated as diameter), which is defined as the diameter given by the output of CT.

Model development with site level data set: In order to develop a model to distinguish between positive and negative biopsies, a site level data set was used to examine trends corresponding to the pathology diagnosis, which was obtained for each individual image. Specifically, the images that are located at the ends of each biopsy (for which we have an approximate image level pathology diagnosis) were examined in order to establish expected trends in nuclear

diameter and density. Images were reviewed for quality control. Images were removed from the data set if there was little to no acriflavine staining present, the image was out of focus, or an artifact, such as a large bubble obscured the image. Additionally benign images from malignant biopsies were removed in order to ensure that benign images in this data set truly only contained benign pathologies. Lastly, in order to assemble a cohort of pure adipose images, images that were considered adipose, but clearly contained other tissue types, were removed from the data set.

A univariate and multivariate analysis was completed carried out in which all variables were initially considered for the site level data set. Logistic regression models were built in SAS software using the PROC LOGISTIC statement. The data set was randomly divided into training and testing sets in order to evaluate the performance of the models. For each model, receiver operator characteristic (ROC) curves were constructed for both the training and testing sets using a web-based tool. The area under the curve (AUC) associated with each ROC curve was determined and tabulated.

Application of optimized models to the biopsy level data set: The models developed using the site level data set were directly applied to the biopsy mosaics. The probability that each image was malignant was determined and the distributions of probability values are shown in the results section as cumulative distribution functions (cdfs). An optimal observation point for distinguishing between malignant and benign biopsies was chosen based on what value yielded the most significant differences between malignant and benign sites from the site level data set. The model that yielded the highest AUC for the biopsy data set was selected and used to examine which biopsies were correctly and incorrectly classified. A cut point on the ROC curve was selected based on the quantity $F = (1 - \text{sensitivity})^2 + (1 - \text{specificity})^2$, which is minimized at the optimal cut point.

Results:

Demographic information: The breakdown of biopsies specimens imaged in this study is shown in Table 2.1. A total of 53 patients are included in this analysis. The demographic information, such as age, BMI, receptor status, menopausal status, and breast density are included in Table 2.1 in addition to the primary histology diagnosis. Of the 53 biopsies, 22 were malignant and 31 were benign specimens. The 22 malignant are comprised of 17 invasive ductal carcinomas (IDC), 2 invasive lobular carcinomas (ILC), 3 ductal carcinomas in situ (DCIS). Of the 31 benign biopsies, 6 contained primarily adipose or fibroadipose (FA) tissue, 19 contained primarily fibroglandular, fibrous, or glandular tissue, and 6 were either fibroadenomas or papillomas.

Table 2.1. Patient Demographics

Characteristic	Biopsies
# of patients	53
Avg. age (range)	53.6 (19 - 84)
Avg. BMI (range)	32.3 (17.6 – 61.7)
Tumor receptor status	
ER +, -	16 (72.7%), 5 (22.7%)

PR +, -	15 (68.2%), 6 (27.3%)
HER-2/neu +/-	10 (52.6%), 9 (47.4%)
Triple negative	4 (21.1%)
Primary histology	
Malignant	22 (41.5%)
<i>Invasive ductal carcinoma (IDC)</i>	17 (32.1%)
<i>Invasive lobular carcinoma (ILC)</i>	2 (3.8%)
<i>Ductal carcinoma in situ (DCIS)</i>	3 (5.7%)
Benign	31 (58.5%)
<i>Adipose, fibroadipose</i>	6 (11.3%)
<i>Fibroglandular, fibrous, glandular</i>	19 (35.9%)
<i>Fibroadenoma, papilloma</i>	6 (11.3%)
Menopausal Status	
Pre	18 (34%)
Peri	1 (1.9%)
Post	34 (64.2%)
Breast density	
1	1 (1.9%)
2	16 (30.2%)
3	25 (47.2%)
4	5 (9.4%)

Site level analysis: Representative images taken from the site level data set are shown in Figure 2.1 A. For the overlay, nuclei that were larger than 7 μm in diameter were false colored red and nuclei that were less than or equal to 7 μm in diameter were false colored green. The threshold of '7 μm ' was chosen because two distinct populations in nuclear diameter were observed previous studies [33].

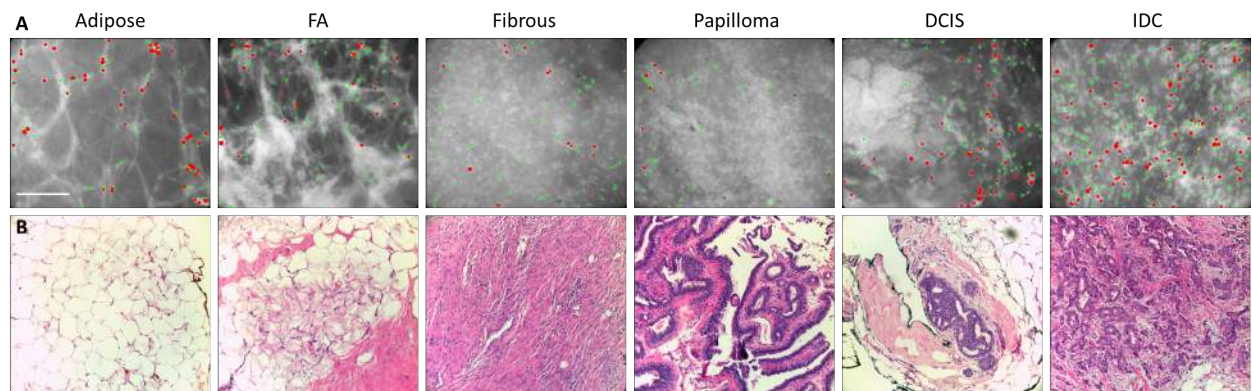


Figure 2.1. Application of sparse decomposition (SD) and circle transform (CT) to representative images taken from the site level data set. The original images were analyzed using SD, and nuclei were subsequently quantified with CT. An overlay is shown in A in which the smaller nuclei (<7 μm diameter) are false colored green and the larger nuclei (≥ 7 μm

diameter) are false colored red. Images of the corresponding H&E site are shown in B. Scale bar is 200 μm .

Figure 2.2 A, B, and C shows boxplots of density for all nuclei, as well as the smaller nuclei (green), and larger nuclei (red). As expected, each density boxplot shows higher densities for the malignant compared to the benign tissue types. The density of the smaller nuclei (green) yields the most significant differences between malignant and benign images ($p = 0.000016$). A scatterplot of the density of the larger nuclei (red) versus the density of the smaller nuclei (green) shown in D illustrates that the density of the smaller nuclei (green) leads to more separation between malignant and benign sites. No significant differences in average diameter were seen between malignant and benign images ($p = 0.54$, data not shown); therefore, diameter was not included in subsequent analysis.

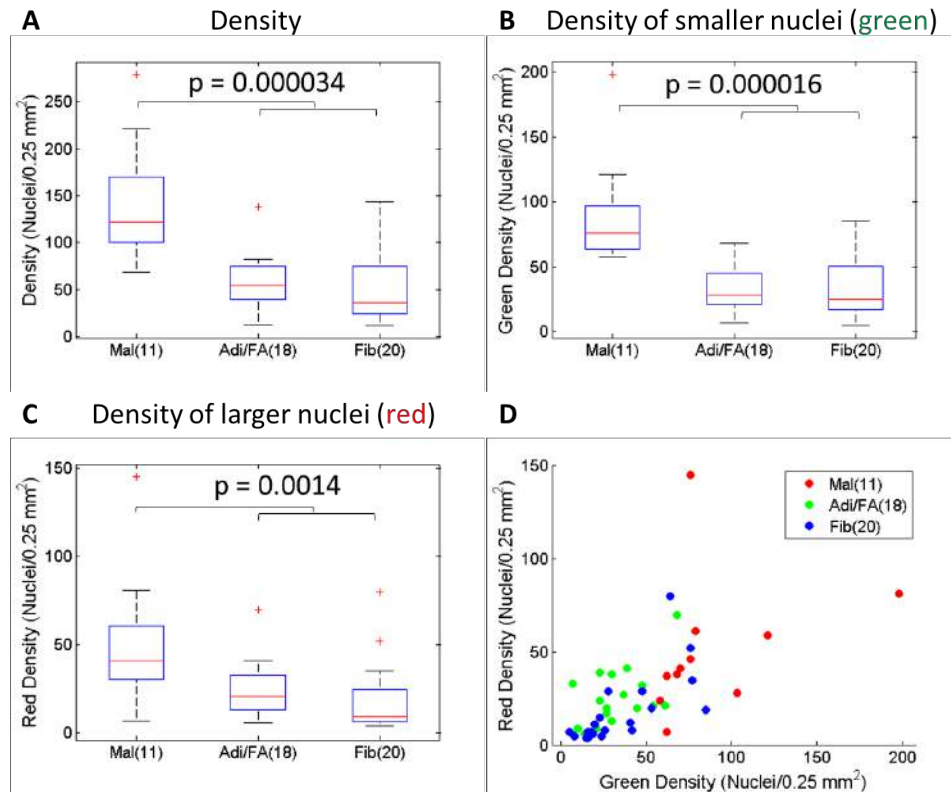


Figure 2.2. Variables calculated for the site level data set. Variables were calculated from 11 malignant (Mal), 18 adipose and fibroadipose (Adi/FA), and 20 fibrous (Fib) images. Boxplots were created for the density of all nuclei, the density of the smaller nuclei (green), and the density of the larger nuclei (red) and are shown in A, B, and C respectively. P values calculated from Wilcoxon rank sums are shown in each boxplot. A scatterplot of the density of the larger nuclei (red) versus the density of the smaller nuclei (green) is shown in D.

Next, the variables illustrated in Figure 2.2 were used to construct univariate and multivariate logistic regression model. In order to evaluate the performance of each mode, the site level data

was broken into a training set and testing set. The number of sites that fell into each set is shown in Table 2.2.

Table 2.2. Site level training and testing sets

Primary histology	All site level	Training set	Testing set
# of sites	50	25	24
Malignant	11 (22.0%)	5 (20.0%)	6 (25.0%)
<i>Invasive ductal carcinoma (IDC)</i>	9 (18.0%)	4 (16.0%)	5 (20.8%)
<i>Invasive lobular carcinoma (ILC)</i>	0 (0.0%)	0 (0.0%)	0 (0.0%)
<i>Ductal carcinoma in situ (DCIS)</i>	2 (4.0%)	1 (4.0%)	1 (4.2%)
Benign	39 (78.0%)	20 (80.0%)	18 (75.0%)
<i>Adipose, fibroadipose</i>	18 (36.0%)	10 (40.0%)	8 (33.3%)
<i>Fibroglandular, fibrous, glandular</i>	20 (40.0%)	10 (40.0%)	10 (41.2%)
<i>Fibroadenoma, papilloma</i>	1 (2.0%)	0 (0.0%)	0 (0.0%)

Models were constructed using the density variables shown in Figure 2.2. ROC curves are shown for both the training and testing data sets in Figure 2.3. All variables performed comparably on the training set. The variable that had the smallest difference between the training and testing set was the density of the smaller nuclei (green).

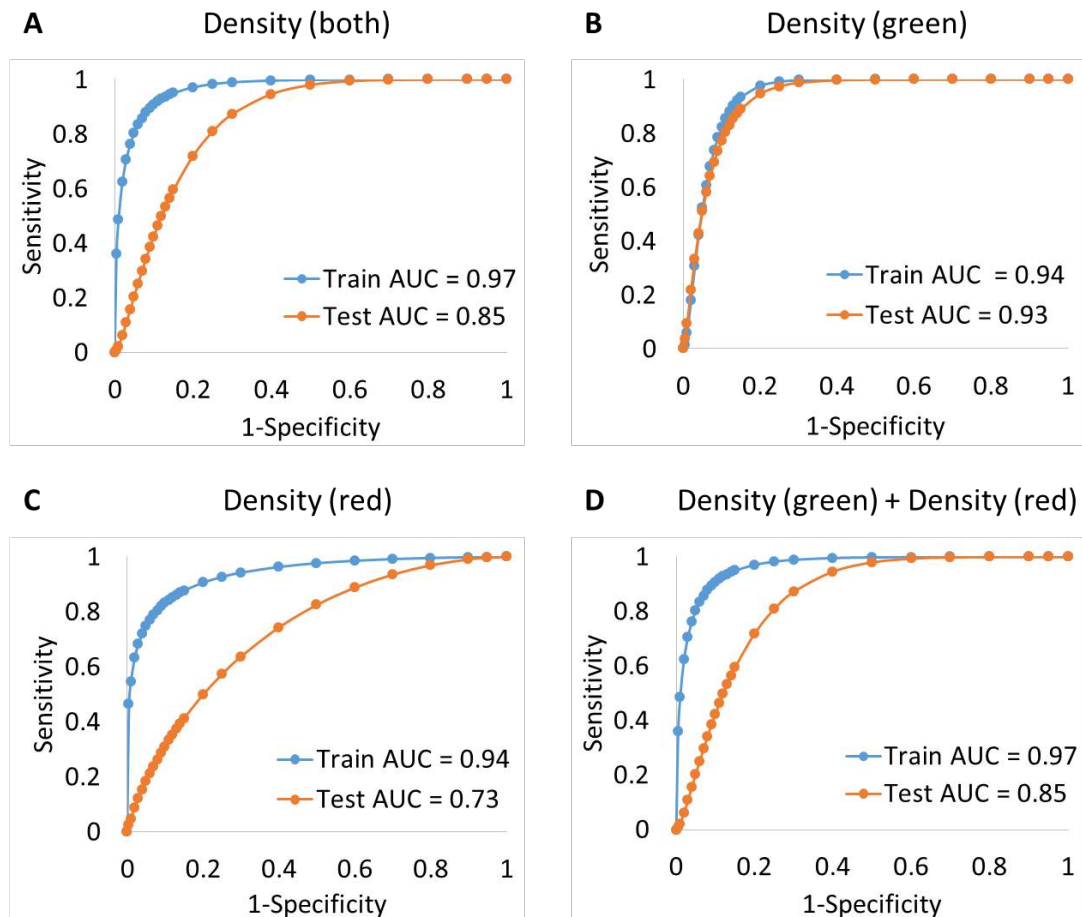


Figure 2.3. Models developed based on the site level data set. The receiver operator curves (ROCs) for all models are shown in A-D. Each plot contains the ROC curve associated with the training and testing data sets. The area under the curve for the training set (Train AUC) and the AUC associated with the testing set (Test AUC) are shown on each plot. The density of the smaller nuclei (green), the density of the larger nuclei (red), and the density of all nuclei are referred to as Density (green), Density (red), and Density (both) respectively.

Biopsy level analysis: Next the models developed for the site level data set were applied to the biopsy mosaics. Figure 2.4 shows a representative example of a malignant and benign biopsy from our study. Each side of the biopsy was scanned length-wise—side 1 corresponds to the top row and side 2 corresponds to the bottom row. In many cases, when the biopsy was rotated to image the other side, the tissue either slightly shrank or expanded; therefore, the same number of images was not always obtained for each side. Black images merely serve as place holders to indicate when this occurs in a biopsy mosaic. A three prong diagnosis was given for each biopsy. In the malignant example in Figure 2.4 A, the left hand side contains IDC, the middle contains IDC and fibrous tissue, and the right hand side contains adipose tissue and inflammation. The probability that each image is malignant (based on the Density (green) model shown in Figure 2.3 B) was determined and the distribution of probability values is shown as a cumulative distribution function (cdf) in Figure 2.4 C. The vertical black line in Figure 2.4 C corresponds to the optimal threshold value (25%), which was determined with the site level ROC curves in Figure 2.3 B. All of the images above 25% are circled in red in Figure 2.4 A and B.

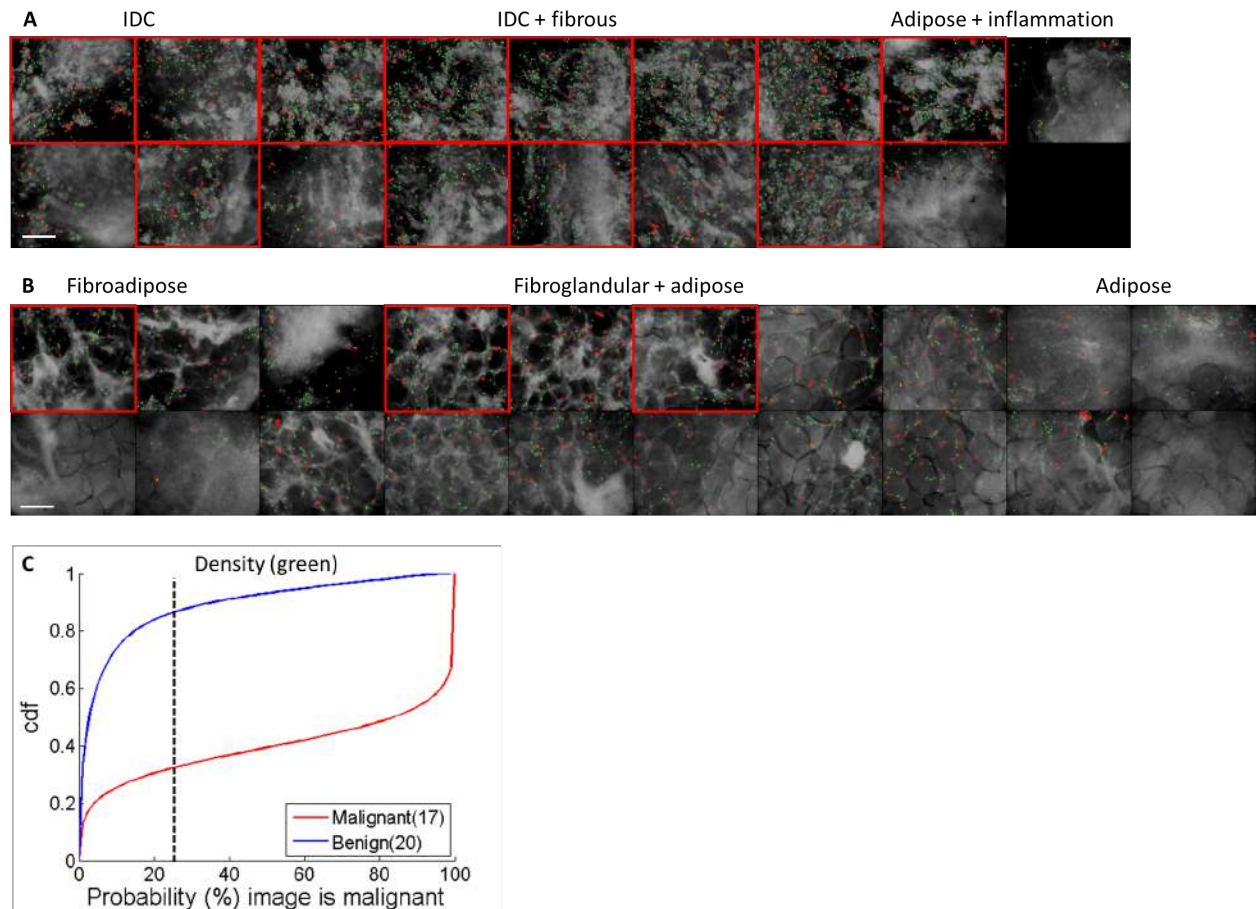


Figure 2.4. The application of an algorithm based on sparse decomposition (SD), and circle transform (CT) applied to representative breast biopsy mosaics. Positive and negative biopsies are shown in A and B respectively. Scale bar is 200 μm . The density (green) model developed on the site level data above was applied to the representative breast biopsy mosaics in A and B. The probability that each image is malignant was determined and the distribution of probability values is shown as a cumulative distribution function (cdf) in C. The vertical black line corresponds to the optimal threshold value (25%), which was determined with the site level ROC curves in Figure 4B. All of the images above 25% are circled in red in A and B.

The models developed on the site level data in Figure 2.3 were applied to each image in the biopsy mosaics. The probability that each image is malignant was determined and the distributions of probability values are shown as cumulative distribution functions (cdfs) in Figure 2.5 A-D. The dotted black line corresponds to the optimal threshold value (25%), which was determined with the site level ROC curves in Figure 2.3 A-D.

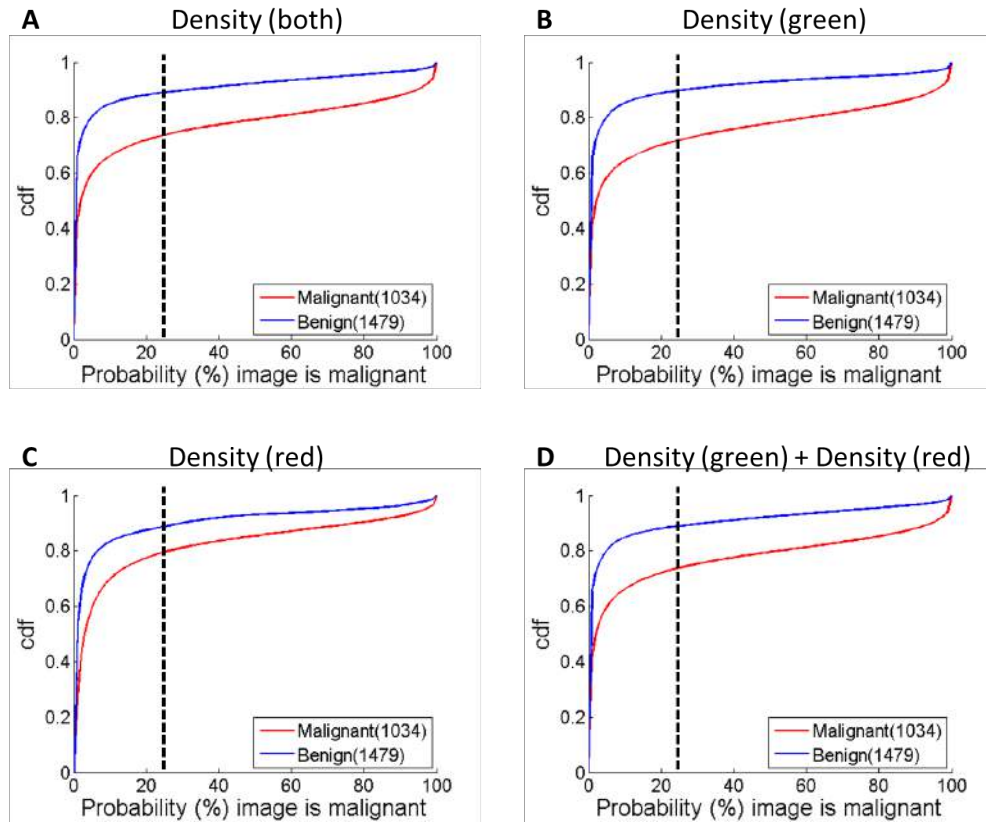


Figure 2.5. Variables calculated for the biopsy level data set. Variables were calculated from 22 malignant and 31 benign biopsies. The models developed on the site level data in Figure 2.3 were applied to each image in the biopsy mosaics. The probability that each image is malignant was determined and the distributions of probability values are shown as cumulative distribution functions (cdfs) in A-D. The vertical black lines correspond to the optimal threshold value (25%), which was determined with the site level ROC curves in Figure 2.3 A-D.

The optimal observation points were used to generate a ROC curve associated with each model and are shown in Figure 2.6. As seen, the AUC associated with the density of the smaller nuclei (green) is the highest (AUC = 0.73).

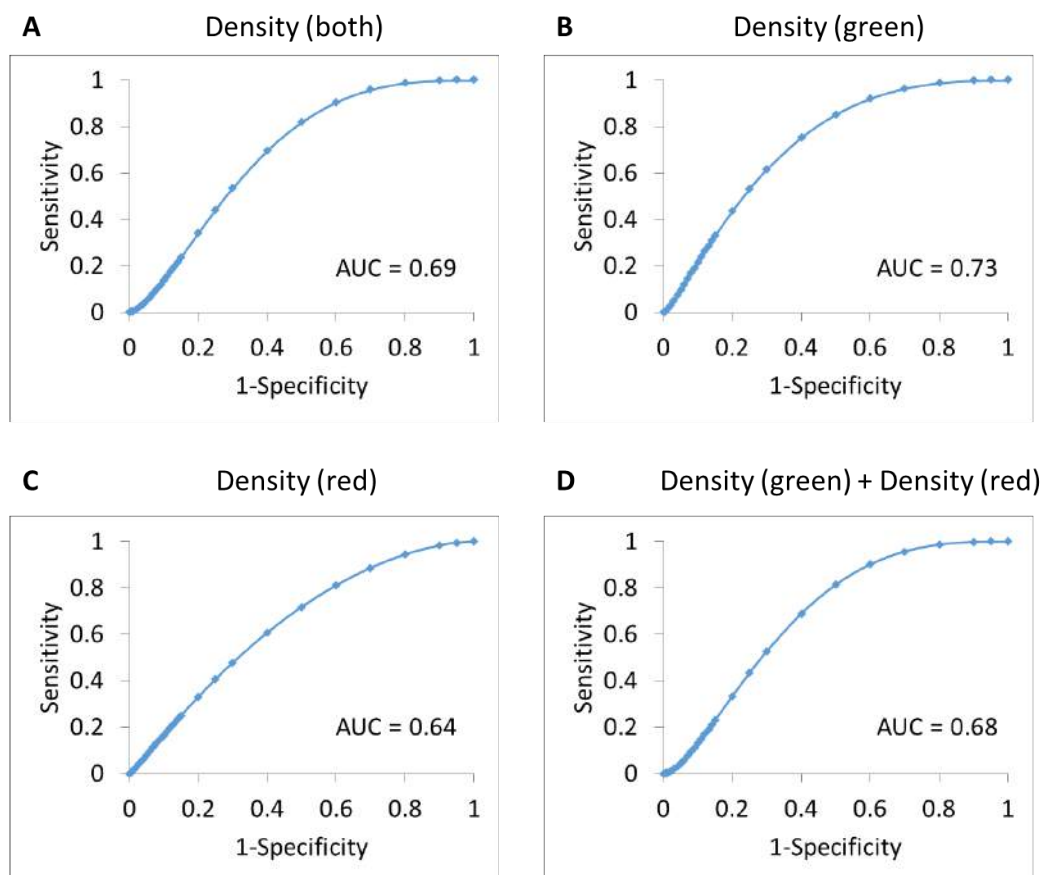


Figure 2.6. The receiver operator characteristic (ROC) curves associated with the optimal threshold value for each model shown in Figure 2.5 are shown here. The area under the curve (AUC) is shown on each plot. The density of the smaller nuclei (green), the density of the larger nuclei (red), and the density of all nuclei are referred to as Density (green), Density (red), and Density (both) respectively.

The optimal cut point on the density (green) ROC curve in Figure 2.6 B yielded 16 TP, 6 FN, 20 TN, and 11 FP, resulting in a sensitivity of 73% and a specificity of 65%. The number that fell within each pathology category is shown in Table 2.3. As seen, the largest number of FNs were from the IDC and DCIS categories and the largest number of FPs were from the fibrous category.

Table 2.3. Number of true positive (TP), false negative (FN), true negative (TN), and false positive (FP) biopsies associated with Density (green)

Category	Total	TP	FN	TN	FP
Malignant	22	16	6	0	0
<i>Invasive ductal carcinoma (IDC)</i>	17	14	3	0	0
<i>Invasive lobular carcinoma (ILC)</i>	2	2	0	0	0
<i>Ductal carcinoma in situ (DCIS)</i>	3	0	3	0	0
Benign	31	0	0	20	11
<i>Adipose, fibroadipose</i>	6	0	0	3	3

<i>Fibrogladular, fibrous, glandular</i>	19	0	0	14	5
<i>Fibroadenoma, papilloma</i>	6	0	0	3	3

Correctly and incorrectly classified representative malignant biopsies that contain IDC are shown in Figure 2.7 A and B respectively. The probability that each image is malignant (based on the density (green) model) was determined and the distributions of probability values are shown as cumulative distribution functions (cdfs) in Figure 2.7 C. As seen, a large proportion of the images have a very high probability of being malignant based on the density (green) model developed in the previous figures. Conversely no images within the incorrectly classified biopsy have a probability greater than 30% that they are positive. This is likely due to the large variation in the staining of these samples. Particularly, there is quite a bit of haze from background staining in B, which is preventing SD+CT from segmenting individual nuclei.

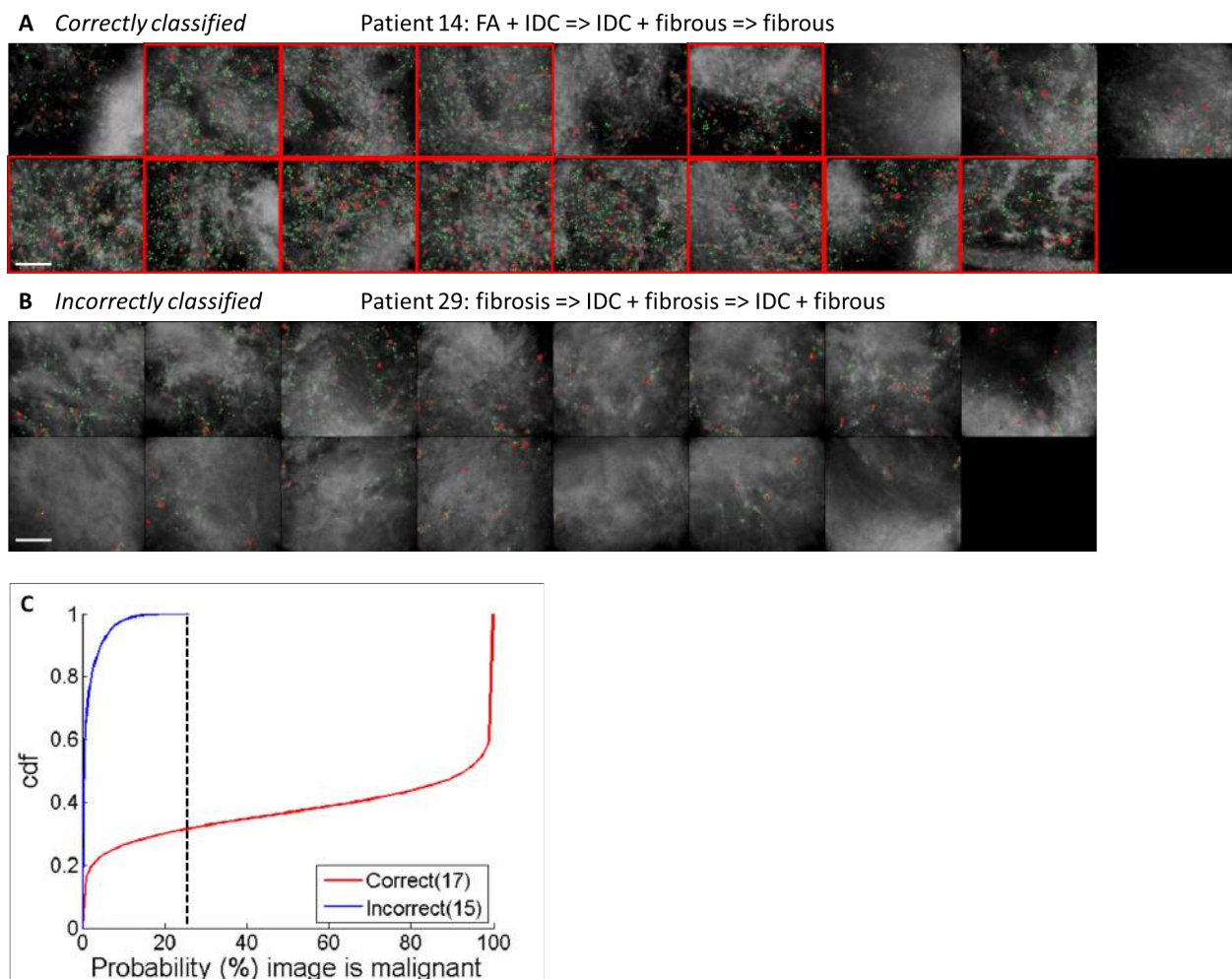


Figure 2.7. Correctly and incorrectly classified representative malignant biopsies that contain IDC are shown in A and B respectively. Scale bar is 200 μ m. The probability that each image is malignant (based on the Density (green) model) was determined and the distributions of probability values are shown as cumulative distribution functions (cdfs) in C. The vertical black

line corresponds to the optimal threshold value (25%), which was determined with the site level ROC curves in Figure 2.3 B. All of the images above 25% are circled in red in A and B.

Similarly correctly and incorrectly classified representative benign biopsies that contain mostly adipose or fat tissue are shown in Figure 2.8. As seen, there are large differences in staining between these two samples. In particular in the incorrectly classified benign sample in Figure 2.8 B there is quite a bit of cellular fibrous tissue in between the adipocytes that is picking up the stain and consequently a large number of nuclei are segmented with SD+CT. This is reflected in the probability distributions—the correctly classified distribution goes straight up (in other words no images have a large probability of being malignant) while the incorrectly classified distribution looks very similar to the malignant distributions seen above.

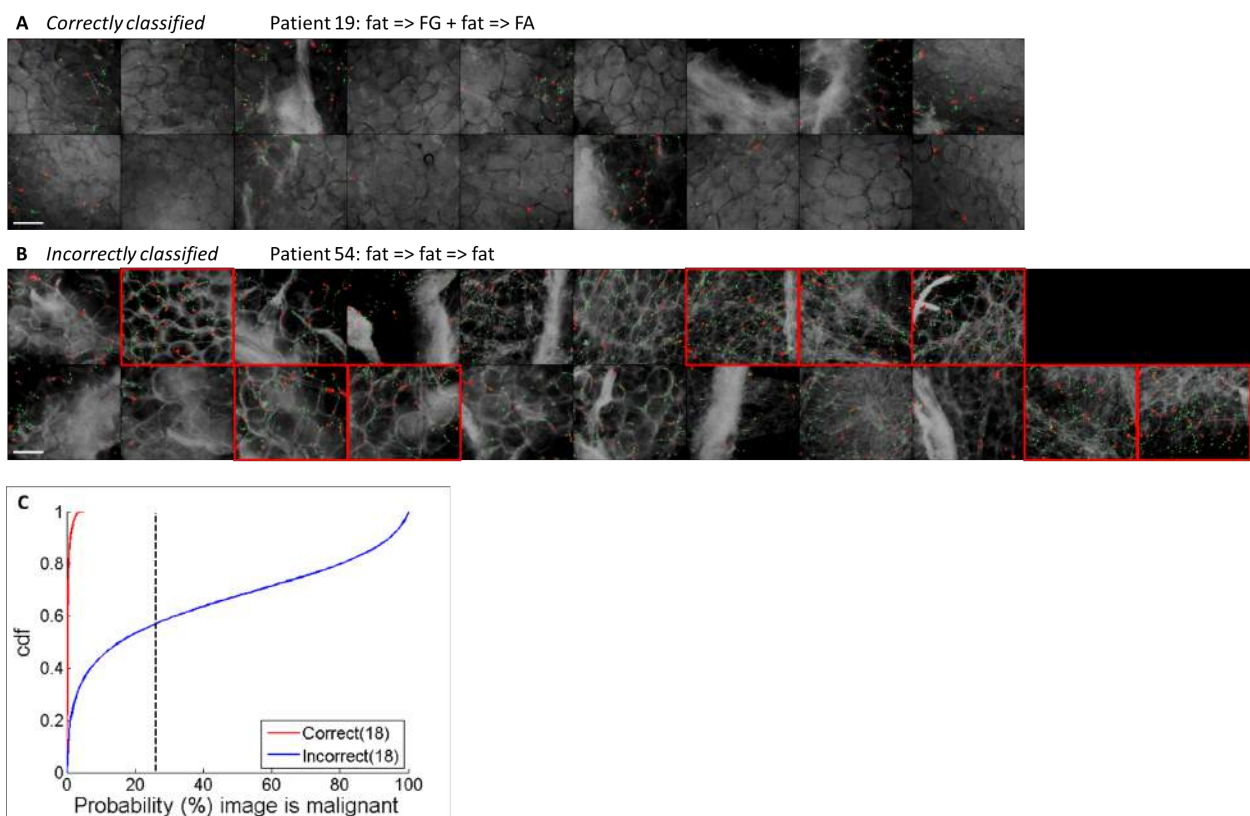


Figure 2.8. Correctly and incorrectly classified representative benign biopsies that contain mostly adipose or fat tissue are shown in A and B respectively. Scale bar is 200 μ m. The probability that each image is malignant (based on the Density (green) model) was determined and the distributions of probability values are shown as cumulative distribution functions (cdfs) in C. The vertical black line corresponds to the optimal threshold value (25%), which was determined with the site level ROC curves in Figure 2.3 B. All of the images above 25% are circled in red in A and B.

Conclusions:

In conclusion, high resolution fluorescence imaging of acriflavine stained tissue combined with an algorithm that leverages sparse decomposition analysis provides a rapid, non-destructive and automated strategy for quantitative pathology of thick tissues with non-uniform background heterogeneity. Density (green) achieved the highest AUCs on the site level testing set (AUC = 0.93) and the highest AUC on the biopsy level data set (AUC = 0.73). This provides a powerful alternative to complicated and time-intensive immunohistochemistry techniques, which require fixing, sectioning, and staining and which can only be diagnosed by a highly trained pathologist.

Plans for year 6:

During year 6, we plan to finalize our diagnostic model to yield the optimal separation between positive and negative biopsies. This includes further identifying why biopsies are being incorrectly classified, and potentially iterating on our model building in order to achieve optimal performance. Together, this work will yield an optimized set of tools that are capable of imaging thick tissue at high resolution with no tissue processing and that can automatically segment and quantify those specimens.

Part B – Rice University

We are also collaborating extensively with Rice University to optimize our microscopic imaging and image analysis approach. Specifically, Rice is also working with acriflavine staining and fluorescence microscopy, but are focusing more on quantification of ductal and adipose features that could work in conjunction with our nuclei segmentation approach to yield optimal diagnosis of breast morphology.

Introduction:

Breast cancer is a leading cause of cancer mortality in women worldwide [43, 44], and although most patients are diagnosed with localized cancer, tumor size and presence of metastasis remain the main prognostic factors for survival [44, 45]. Current imaging tools provide limited ability to detect early lesions and to image relevant biomarkers *in situ*. Thus developing novel strategies for early detection of invasive and metastatic disease may have a significant impact on reducing patient morbidity and improving survival.

Traditional methods for early detection of breast cancer, including physical examination, mammography, ultrasound, and magnetic resonance imaging (MRI), are limited by low sensitivity and specificity for pre-malignant lesions [46-52]. In addition, these imaging methods do not give molecular information. As a result, histologic assessment is currently the reference standard for early diagnosis of breast cancer lesions and assessment of relevant biomarkers, which also typically requires immunohistochemical (IHC) staining. Both histologic assessment and IHC require biopsy, take extensive time to perform, and may need to be repeated in cases where lesions are missed due to sampling error. Histologic assessment has a limited ability to

monitor response to targeted therapy, because of the need to obtain tissue specimens and the extensive time required to prepare and review tissue specimens.

Optical imaging approaches have the potential to address the limitations of traditional methods to detect breast cancer and monitor response to therapy and can provide the ability to image lesions in real time with minimal invasion [53-63]. With the introduction of fiber optic probes, images can be acquired intraoperatively or through needles with high spatial resolution to visualize subcellular morphology and tumor microenvironment [54, 55, 64]. It is also possible to add molecularly targeted, optically active contrast agents to image changes in biomarker expression [65]. A number of high resolution imaging approaches have been proposed to characterize breast lesions, including confocal reflectance and fluorescence microscopy, fiber optic microendoscopy (FOME).

The long term objective of this work is to develop and apply imaging systems and molecular contrast agents which can be used in patients to 1) improve early detection and rapid assessment of breast cancer lesions, 2) aid in selection of targeted therapeutics, and 3) monitor the efficacy of these therapeutics in real-time.

Progress to Date:

Rice's progress to date is split into three sections, each of which describes the methods, results, and preliminary conclusions involved. Sections include the following:

- 1) *Feasibility of optical imaging techniques for imaging human breast tissue: 2011-2014*
- 2) *Adipocyte segmentation study: 2012-2014*
- 3) *Evaluation of invasive tumor cellularity in inflammatory breast cancer core needle biopsy specimens: 2013-2014*

Feasibility of optical imaging techniques for imaging human breast tissue: 2011-2014:

Breast cancer development is a complex process which occurs when atypical ductal hyperplasia progresses to low grade ductal carcinoma *in situ* (DCIS), a malignant precursor to invasive breast cancer [66]. Identification of DCIS is important for preventing the development of invasive breast cancer; however, it is difficult to distinguish DCIS – a malignant lesion - from ductal hyperplasia – a non-neoplastic lesion [67].

The current standard for breast lesion assessment is histologic assessment of tissue specimens stained with hematoxylin and eosin (H&E), which is limited by extensive preparation steps and time requirements. There is an unfulfilled need for clinical imaging tools to evaluate tumor margins, residual tumor in the resection bed, adequacy of core needle biopsy specimens for biobanking or genetic studies, and to monitor disease regression in response to treatments that are being tested in animal studies. Optical imaging techniques such as confocal fluorescence microscopy have the potential to meet these needs [17, 61, 63, 65, 68, 69]. Confocal

fluorescence microscopy can be used in a clinical setting to acquire high resolution images of breast tissue architecture at near video rate. In addition, it can be performed on fresh tissue, and require minimal tissue preparation. The objective of this study was to determine whether images of fresh human breast tissue acquired with confocal fluorescence microscopy provide sufficient information to enable discernment of neoplastic and non-neoplastic breast features.

To meet this objective, the aims of this study were to:

- a. Characterize the microscopic architecture of normal, benign and neoplastic breast biopsies visible using confocal fluorescence microscopy
- b. Evaluate diagnostic accuracy of confocal fluorescence microscopy to assess breast architecture compared to the standard for breast lesion assessment: histology with H&E staining
- c. Quantitatively analyze metrics of morphologic changes associated with progression from non-proliferative and hyperplastic ducts to DCIS and to compare performance of these metrics for classification of DCIS in confocal and histologic images.

Methods:

- 1) We continued to use a commercial confocal microscope (Vivascope 2500, Caliber Imaging and Diagnostics, Inc.) to image resected breast tissue and needle biopsy specimens (n = 139 specimens from 73 patients). There were 253 ROIs identified which had corresponding breast architecture in confocal fluorescence and histologic images. The images were assembled into the existing library, which we have previously used to facilitate comparison between high resolution optical images and the corresponding histological sections (Figure 2.9).
- 2) We developed a computerized algorithm to automate segmentation of ducts and lumens in confocal fluorescence images (Figure 2.10).
 - a. To enhance image contrast, a low pass filter was applied to images followed by adaptive histoequalization.
 - b. To segment duct walls, images were converted from grayscale to binary with a user-defined threshold tool. The threshold was set at a value which segmented the duct wall based on fluorescence intensity. Thresholds were chosen so that binary ducts showed comparable thickness to the ducts observed in the corresponding raw confocal image.
 - c. An interactive polygon selection tool was used to segment duct walls from surrounding features with similarly high fluorescence intensity.
- 3) Following automated segmentation of ducts and lumens, we used the computerized algorithm described previously to quantitatively analyze duct morphology in confocal images using parameters of ducts and lumens, including:
 - i. duct wall width (mean, standard deviation, and variance)
 - ii. number of lumens contained within the duct wall

- iii. major and minor dimensions of ducts and lumens
 - iv. duct and lumen area
 - v. duct and lumen area fitted to an ellipse
 - vi. duct and lumen eccentricity
 - vii. duct and lumen solidity
- 4) The best performing parameters for classifying DCIS from non-neoplastic ducts were identified using linear discriminant analysis and each parameter's performance was assessed using sensitivity, specificity, and area under the curve (AUC). Mean parameter values were compared between histologic types of ducts using a Student t-test for samples with unequal variances.
- 5) To optimize classification of duct histologic types, we used a classification regression tree analysis, which identified parameters and cutoff values for those parameters that would classify DCIS from non-neoplastic ducts with the highest accuracy.

Results:

- 1) Parameters of ducts segmented by the automated algorithm were quantified in confocal images (n = 51 sites) acquired from 12 patients. The parameter which best classifies DCIS from non-neoplastic ducts in confocal images is number of lumens, which separates DCIS from non-neoplastic ducts with a sensitivity of 88% and a specificity of 88%, corresponding to an area under the curve of 0.92 (Figure 2.11). DCIS lesions had a significantly higher average number of lumens compared to non-hyperplastic ducts and hyperplastic ducts: $p < 0.001$ by Student t-test (Figure 2.12). The parameter which best classifies non-hyperplastic ducts from DCIS and hyperplasia is median duct wall width; sensitivity of 75% and specificity of 100%, which corresponds to an area under the curve of 0.91 (Figure 2.13). Hyperplastic ducts and DCIS lesions have significantly higher average median duct wall width than non-hyperplastic ducts: $p < 0.05$ for hyperplastic ducts and $p < 0.01$ for DCIS lesions (Figure 2.14).

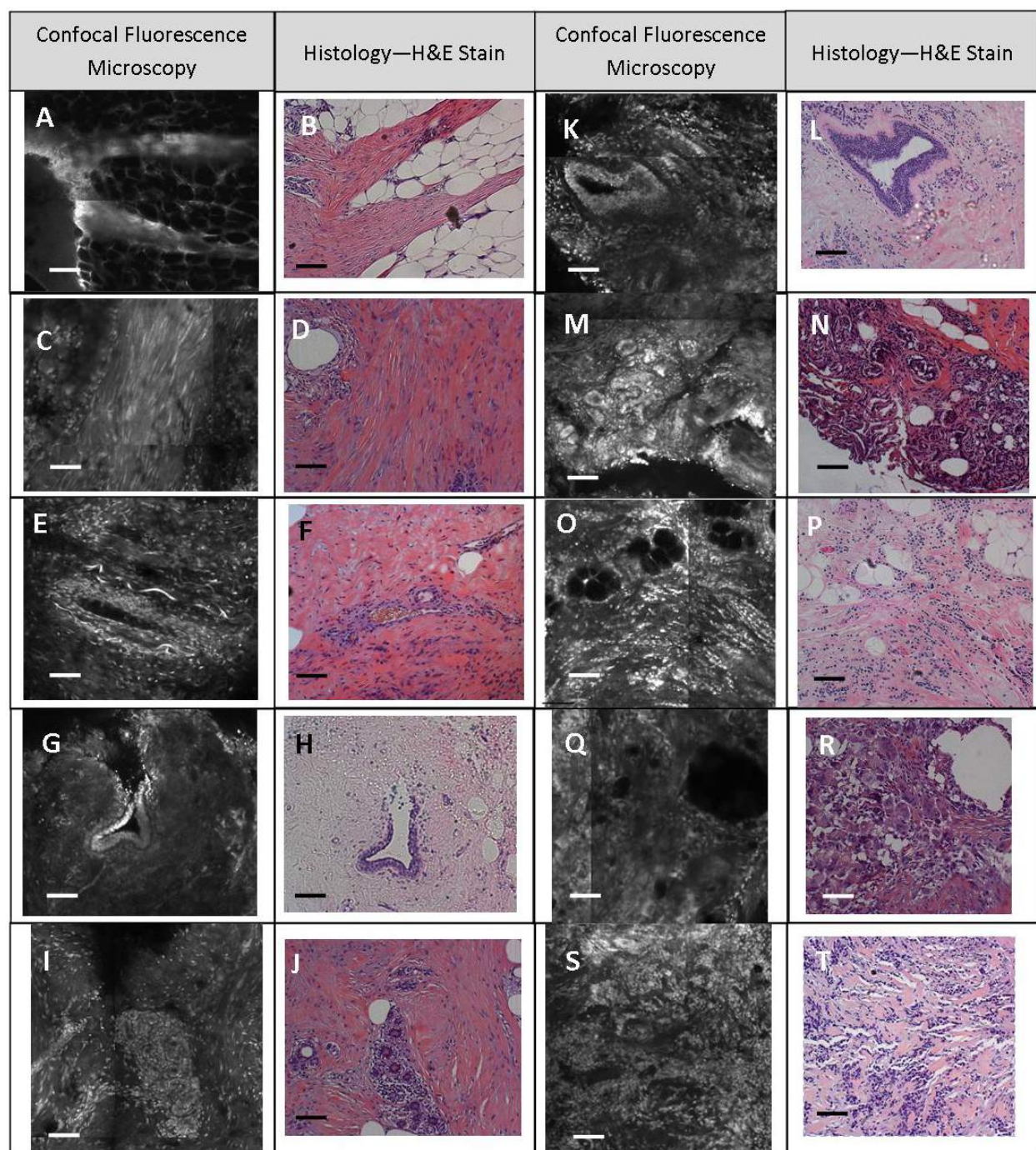


Figure 2.9 Representative images in library of breast features identified in confocal and histologic images. Architecture indicative of normal breast tissue (A-J), benign changes (K-N), and neoplastic disease (O-T) were identified at corresponding sites in histologic and confocal images. Normal breast tissue features identified include: adipose tissue (A,B), fibrous tissue (C,D), blood vessels (E,F), non-hyperplastic ducts (G,H), and lobules (I,J). Some features identified were indicative of benign changes, including usual ductal hyperplasia (K,L) and sclerosing adenosis (M,N). Neoplastic disease types identified include invasive lobular

carcinoma (O,P), invasive ductal carcinoma (Q,R), and inflammatory breast cancer (S,T). Scale bars are 100 μ m.

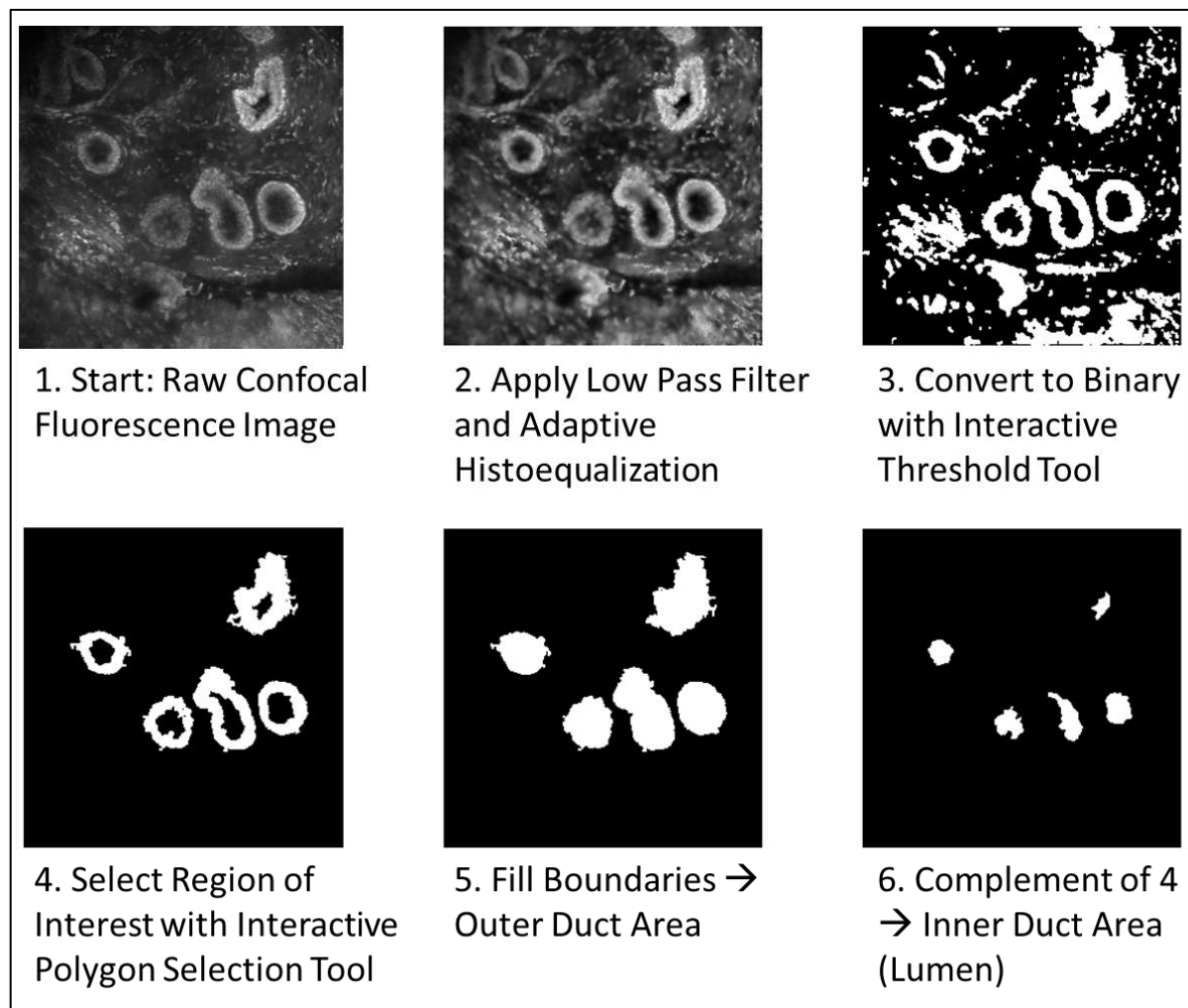


Figure 2.10 Automated algorithm to segment ducts in confocal images. (1) Raw image acquired from confocal fluorescence microscope with 750 x 750 μ m field of view. (2) Wiener low pass filter and adaptive histoequalization applied to (1). (3) Convert (2) from grayscale to binary image with interactive threshold tool. (4) Select Region of Interest (ROI) around ducts with interactive polygon selection tool. (5) Fill boundaries of ducts identified in (4) to segment the outer boundaries of the duct. (6) Select the complement of (4) to segment the inner boundaries of the duct (lumen).

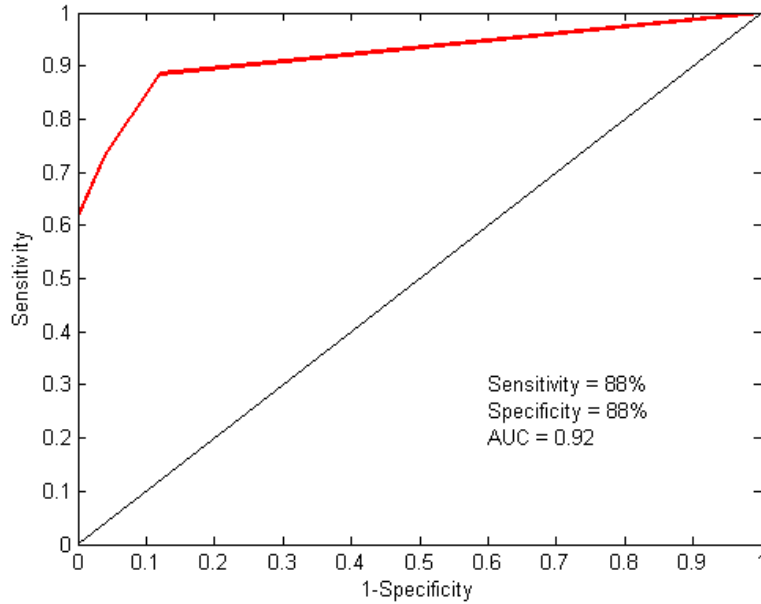


Figure 2.11 Number of lumens as a parameter to classify DCIS in confocal images. The parameter that results in the best separation between DCIS and non-neoplastic ducts is the number of lumens, with a cutoff of 2 lumens (sensitivity = 88%, specificity = 88%, AUC = 0.92).

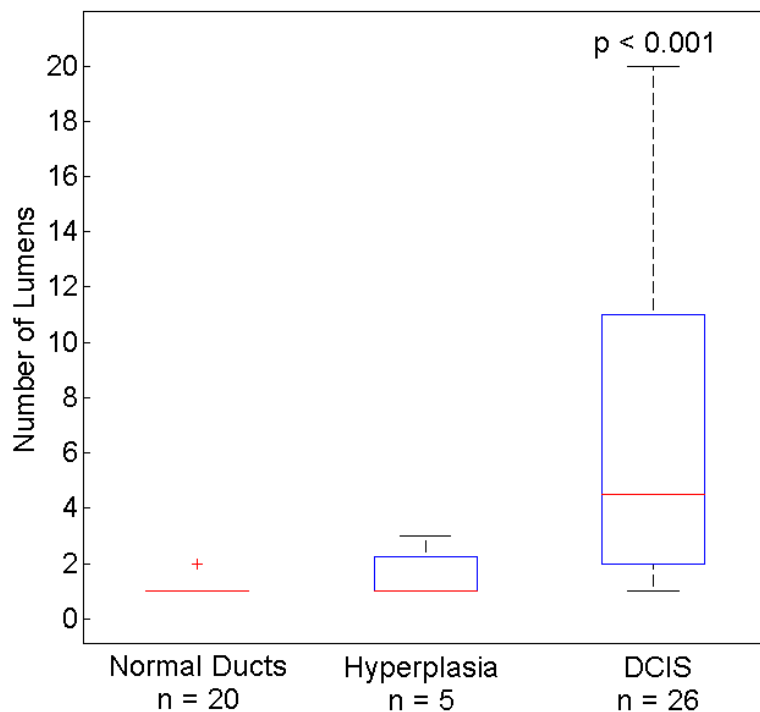


Figure 2.12 Boxplot representing the number of lumens segmented with the duct-based segmentation algorithm. DCIS lesions have a significantly higher number of lumens than non-hyperplastic ducts and hyperplasia ($p < 0.001$).

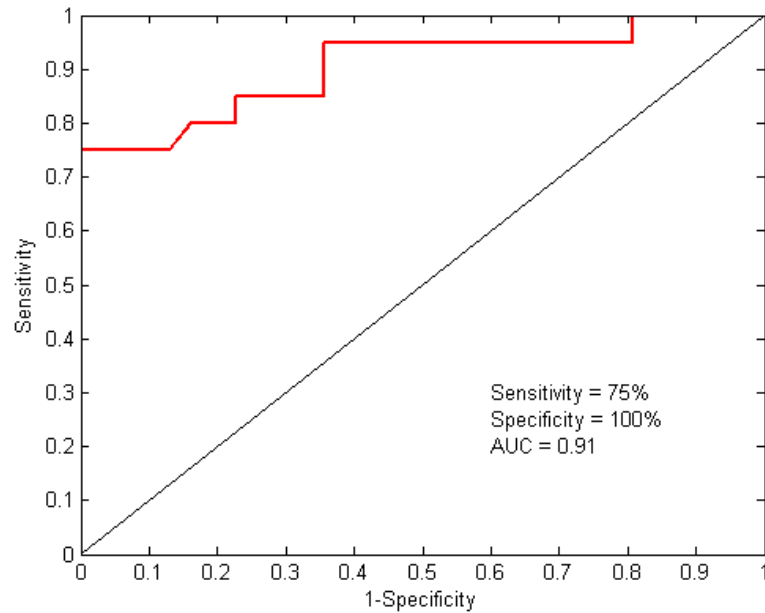


Figure 2.13 Median duct wall width as a parameter to classify non-hyperplastic ducts in confocal images. The parameter that results in the best separation between non-hyperplastic ducts and DCIS lesions and hyperplasia is median duct wall width, with a cutoff of 26.7 μm (sensitivity = 75%, specificity = 100%, AUC = 0.91).

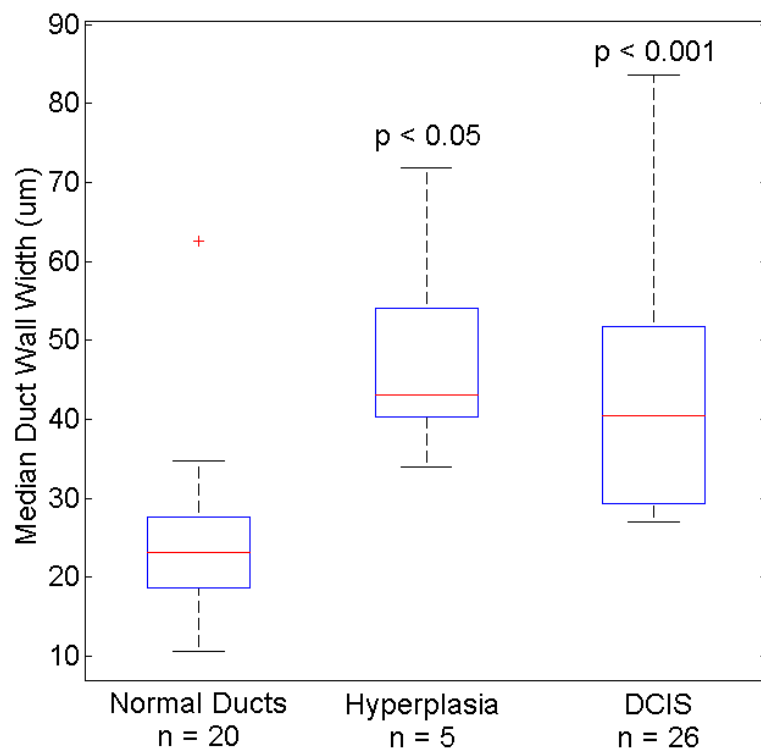


Figure 2.14 Boxplot representing the median duct wall width measured with the duct-based segmentation algorithm. Median duct wall widths are significantly higher in hyperplastic ducts ($p < 0.05$) and DCIS lesions ($p < 0.001$) than in non-hyperplastic ducts.

- 2) Using classification regression tree analysis, we developed a model to classify ducts by histologic type (Figure 2.15). The two parameters which resulted in the most accurate classification of DCIS through the classification regression tree model are median duct wall width with a cutoff value of 26.7 μm and number of lumens with a cutoff value of 2 lumens. Using this model, DCIS was classified with 88.5% sensitivity and 92% specificity, and 88% of the 51 sites were correctly classified.

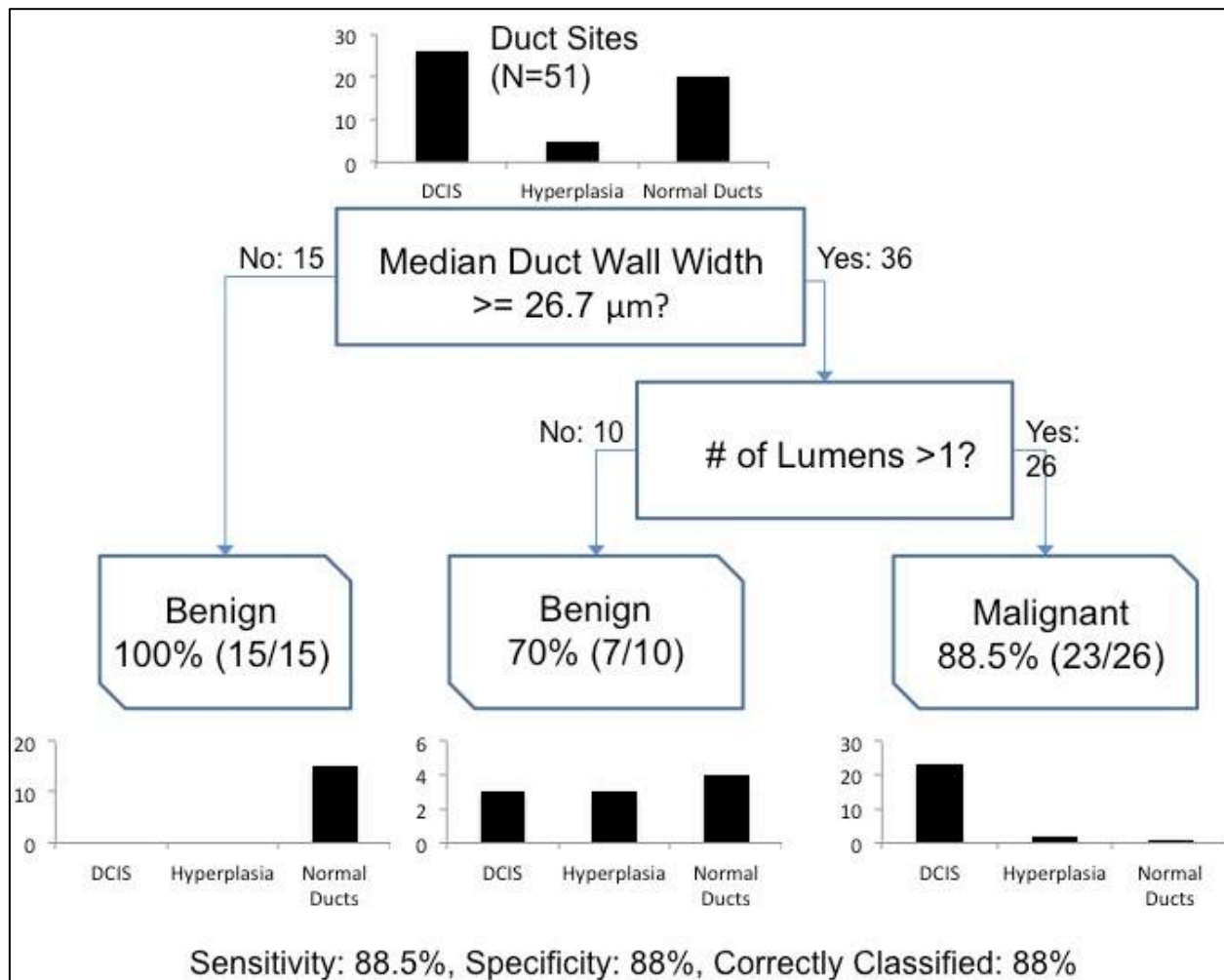


Figure 2.15 Classification regression tree model developed to optimize classification of DCIS from non-neoplastic ducts.

Conclusions:

In this study, we developed an automated algorithm to segment breast ducts observed in confocal fluorescence images. Using the previously developed computerized algorithm, we quantitatively analyzed parameters of ducts segmented from confocal images.

Our findings suggest that quantitative analysis of duct morphology in confocal fluorescence images could potentially provide an objective method to assess duct histology and classify DCIS from benign ducts. This study has potential for use in clinical and research settings, including applications in 1) assessment of tumor margin status, and 4) evaluation of disease regression and progression in animal studies.

Adipocyte segmentation study: 2012-2014:

Extensive literature has shown that stromal components in the tumor microenvironment play a role in breast carcinoma progression and invasion [70-73]. It has recently been suggested that adipocytes located adjacent to tumors participate in crosstalk with invasive cancer cells through bi-directional paracrine signaling pathways, which affect processes such as tissue remodeling, adipogenesis and energy metabolism, oncogenesis, inflammation, and immune response [70]. The objective of this study is to use confocal fluorescence microscopy to evaluate morphological characteristics of adipocytes adjacent to neoplastic and non-neoplastic breast tissue to determine if there is a correlation between adipocyte morphology and clinical diagnosis.

Methods:

- 1) The confocal fluorescence images of tissue specimens acquired in the previous study were used as the basis for quantitative evaluation of the morphology of adipocytes adjacent to invasive ductal carcinoma, DCIS, and normal collagen.
- 2) We used the previously developed algorithm to segment and analyze adipocyte cells in confocal fluorescence images adipose tissue in specimens with invasive ductal carcinoma, DCIS, and normal collagen (Figure 2.16). The following parameters of adipocyte cells were measured for each cell within a 750 x 750 μm site:
 - i. Cell area: adipocyte area based on segmentation
 - ii. Ellipse area: ellipses were fitted to each cell within a site
 - iii. Major dimension: larger dimension of the ellipse fitted to each cell
 - iv. Equivalent diameter: the diameter of a circle with the same area as the segmented adipocyte
 - v. Cell eccentricity: ratio of the distance between the focus of the ellipse and its major dimension
 - vi. Cell solidity: proportion of pixels in the convex hull which are also within the segmented adipocyte
- 3) Mean parameter values were compared between adipocytes measured in sites near invasive ductal carcinoma, DCIS, and normal collagen using a Student t-test for samples with unequal variances.

Results:

- 1) Adipocytes were segmented and analyzed in tissue specimens acquired from 14 patients (Table 2.4). A single site consists of a 750 x 750 μm confocal microscope field of view. Regions consist of groups of 2-4 adjacent sites, where one site is located at the edge of invasive ductal carcinoma, DCIS, or normal collagen, and the additional sites are located in a single file line extended from the first site and into adipose tissue (Figure 2.16). At each site adipocytes were segmented using the previously described algorithm (Figure 2.17).

Table 2.4 Summary of Patients, Regions, and Sites for Adipocyte Data

Diagnosis		Patients	Regions	Sites	Adipocytes
<i>IDC tumor</i>	<i>Neoplastic</i>	14	40	135	6675
<i>DCIS</i>	<i>Neoplastic</i>	2	9	160	1438
Collagen	Benign	14	41	160	5940
All		14	90	326	14053

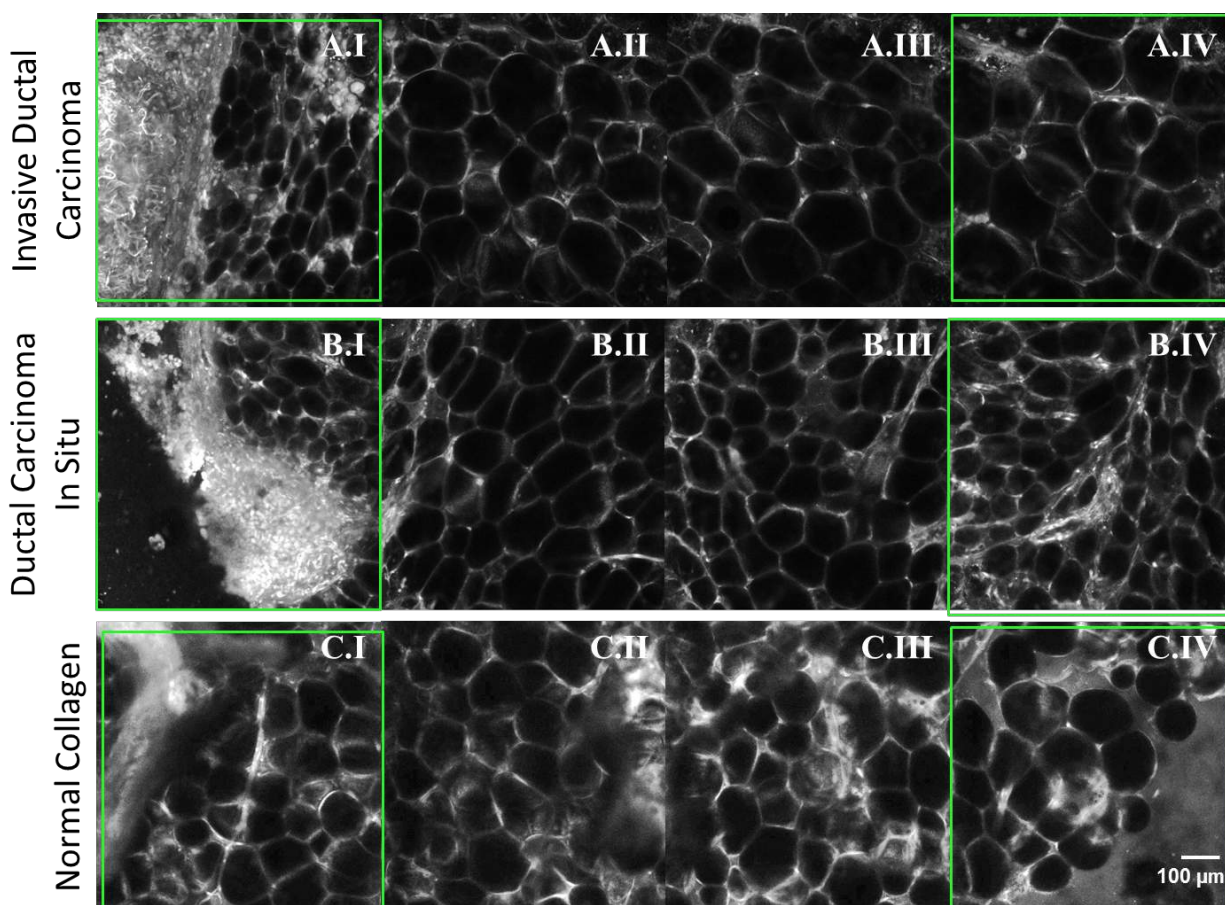


Figure 2.16 Representative images of confocal images of breast tissue, in which adipocytes were measured. Adipocytes were measured in regions consisting of 2-4 sites (750 x 750 μm), at sites located near IDC (A.I-IV), DCIS (B.I-IV), and normal collagen (C.I-IV). where the first site is located adjacent to invasive ductal carcinoma, DCIS, or normal collagen (A.I, B.I, C.I) and

additional sites are oriented in a straight line into adipose tissue (A.II-IV, B.II-IV, C.II-IV). Scale bar is 100 μ m.

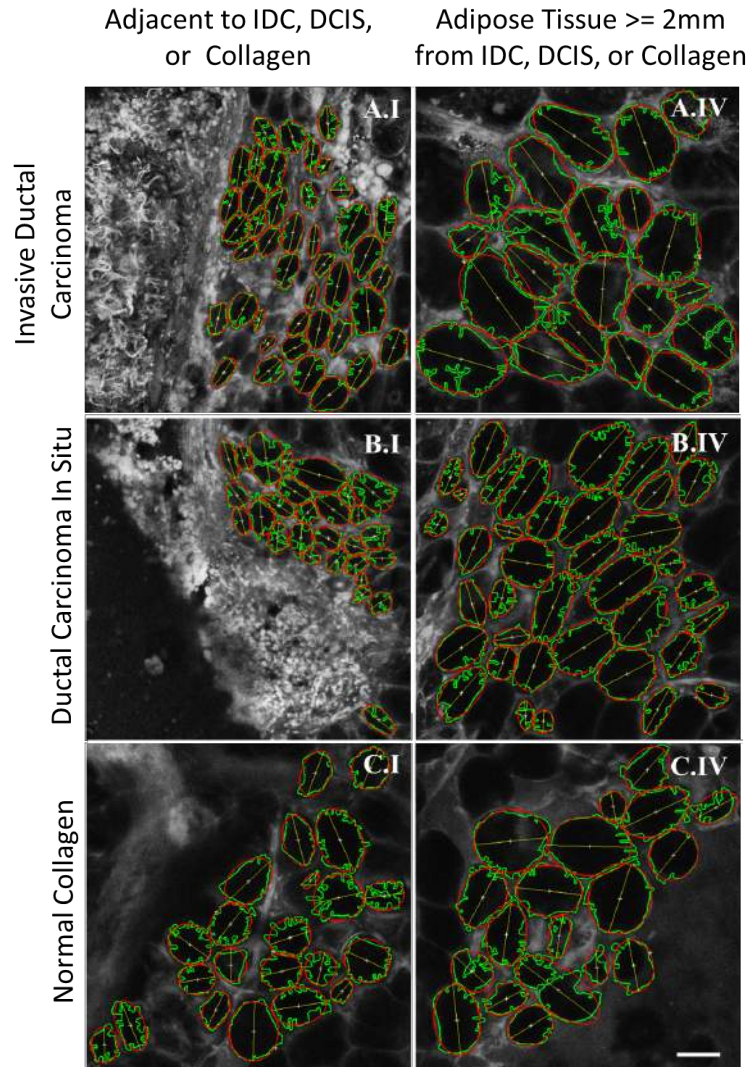


Figure 2.17 Representative sites showing segmented adipocytes. Adipocytes were segmented using the previously described algorithm, which identified adipocyte outlines (green lines) and approximated the adipocyte outlines by fitting an ellipse to each adipocyte (red ellipses). Adipocytes were analyzed at locations adjacent to invasive ductal carcinoma (IDC), ductal carcinoma in situ (DCIS), and normal collagen (A.I, B.I, C.I) and at sites extending laterally into adipose tissue. The sites furthest from the edge of IDC, DCIS, and collagen were ≥ 2 mm away (A.IV, B.IV, C.IV).

- 2) All parameters except average solidity showed a significant difference in average value from the sites adjacent to IDC, DCIS, and collagen (Figure 2.16: A.I, B.I, C.I) to the next site further from the margins of non-adipose tissue (Figure 2.16: A.II, B.II, C.II). The parameters that showed the most significant differences between adipocytes adjacent to

neoplastic sites compared to adipocytes adjacent to collagen were average ellipse area (Figure 2.18) and average equivalent diameter (Figure 2.19).

- 3) Average ellipse area measured the average area of ellipses fitted to the segmented adipocytes. Significantly larger values for average ellipse area were observed between:
 - i. Sites adjacent to IDC, DCIS, and collagen and the second site extending into adipose tissue (Figure 2.18: A.I vs A.II, B.I vs. B.II, and C.I vs. C.II)
 - ii. Sites adjacent to IDC, DCIS, and collagen and the forth site extending into adipose tissue (Figure 2.18: A.I vs A.IV, B.I vs. B.IV, and C.I vs. C.IV)
 - iii. Sites adjacent to IDC and sites adjacent to collagen (A.I vs. C.I)
 - iv. Sites adjacent to DCIS and sites adjacent to collagen (B.I vs. C.I)
- 4) There were no significant differences in values for average ellipse area observed between
 - i. Sites adjacent to IDC and sites adjacent to DCIS (A.I vs. B.I)
 - ii. The sites measured furthest from IDC margins and sites adjacent to collagen (A.IV vs. C.I)
 - iii. The sites measured furthest from DCIS margins and sites adjacent to collagen (B.IV vs. C.I)

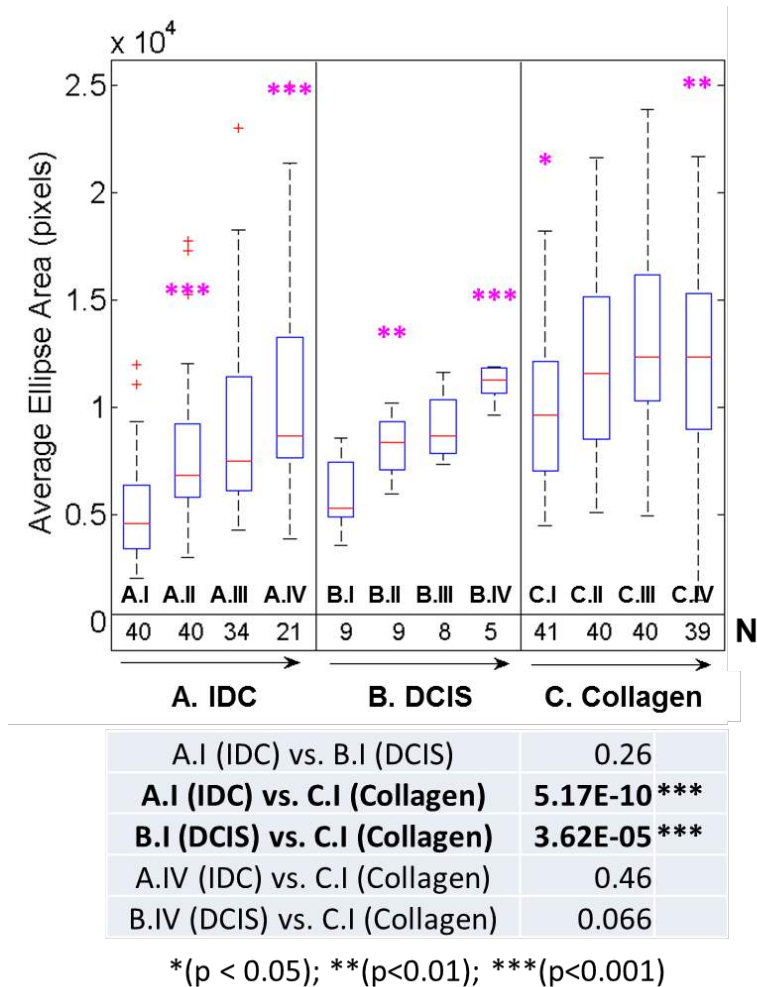


Figure 2.18 Boxplot of average area of ellipses fitted to adipocytes (pixels) for fields of view measured near IDC (A), DCIS (B), and Collagen (C). N indicates the number of fields of view in which adipocytes were measured. Student t-tests were performed to compare the average ellipse area for fields of view at different locations relative to IDC (A.I-IV), DCIS (B.I-IV), and collagen (C.I-IV) margins. P-values < 0.05 indicate significant differences in average ellipse area between different fields of view (*p < 0.05, **p < 0.01, ***p < 0.001).

- 5) Average equivalent diameter is a measure of the diameter of a circle with the same area as the adipocyte. Significantly larger values for average equivalent diameter were observed between:
 - i. Sites adjacent to IDC, DCIS, and collagen and the second site extending into adipose tissue (Figure 2.18: A.I vs A.II, B.I vs. B.II, and C.I vs. C.II)
 - ii. Sites adjacent to IDC, DCIS, and collagen and the forth site extending into adipose tissue (Figure 2.18: A.I vs A.IV, B.I vs. B.IV, and C.I vs. C.IV)
 - iii. Sites adjacent to IDC and sites adjacent to collagen (A.I vs. C.I)
 - iv. Sites adjacent to DCIS and sites adjacent to collagen (B.I vs. C.I)
 - v. The sites measured furthest from DCIS margins and sites adjacent to collagen (B.IV vs. C.I)

- 6) There were no significant differences in values for average ellipse area observed between
- vi. Sites adjacent to IDC and sites adjacent to DCIS (A.I vs. B.I)
 - vii. The sites measured furthest from IDC margins and sites adjacent to collagen (A.IV vs. C.I)

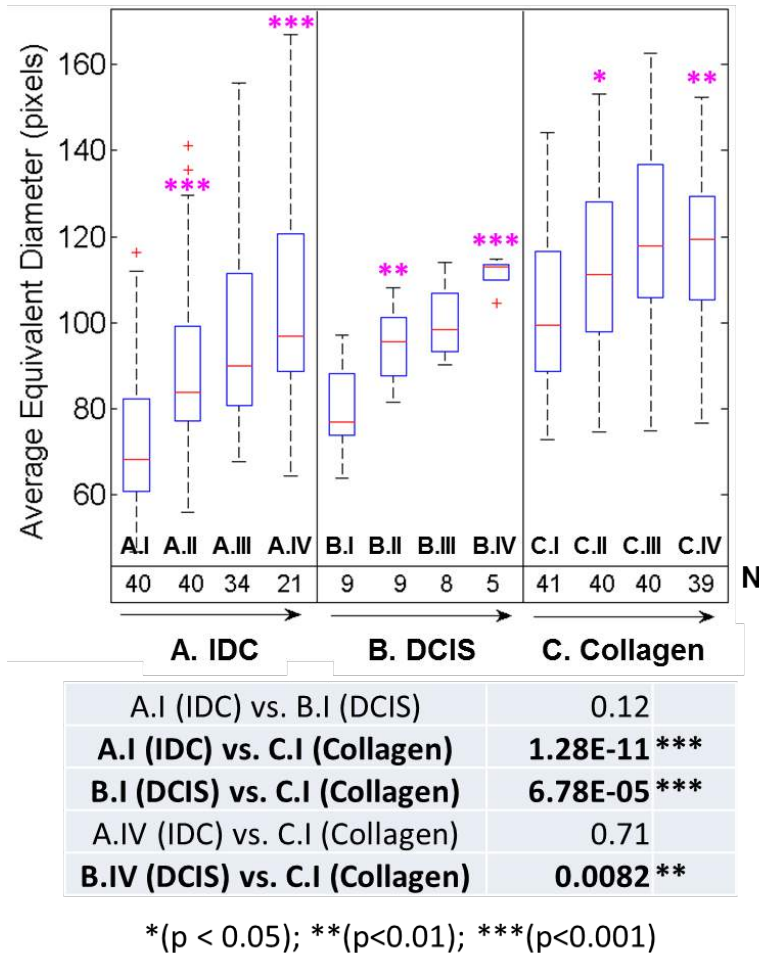


Figure 2.19 Boxplot of average equivalent diameters (pixels) of adipocytes in fields of view measured near IDC (A), DCIS (B), and Collagen (C). N indicates the number of fields of view in which the equivalent diameter of adipocytes was measured. Student t-tests were performed to compare the average equivalent for fields of view at different locations relative to IDC (A.I-IV), DCIS (B.I-IV), and collagen (C.I-IV) margins. P-values < 0.05 indicate significant differences in average equivalent between different fields of view (*p < 0.05, **p < 0.01, ***p < 0.001).

Conclusions:

We show that adipocytes adjacent to invasive ductal carcinoma and DCIS have similar physical characteristics: 1) adipocyte area and diameter are significantly lower immediately adjacent to neoplastic lesions than 2 mm from the margins of neoplastic lesions; 2) adipocyte area and diameter are significantly lower adjacent to neoplastic lesions than in normal tissue adjacent to

collagen; 3) there is no significant difference in adipocyte area or diameter between adipocytes adjacent to invasive ductal carcinoma and DCIS; and 4) there is no significant difference in adipocyte area between cells 2 mm from the margins of neoplastic lesions and cells immediately adjacent to normal collagen.

The findings of this study indicate that adipocyte area and diameter could potentially be used as architectural biomarkers to characterize the malignant potential of a lesion. Additional work should be done to evaluate clinical factors and/or genetic/epigenetic factors that correlate with adipocyte size.

Evaluation of invasive tumor cellularity in inflammatory breast cancer core needle biopsy specimens: 2013-2014:

Inflammatory breast cancer is a rare and aggressive type of breast cancer, which typically presents with erythema and edema [74]. Tissue sampling with image-guided core needle biopsy (CNB) is a particularly problematic issue with inflammatory breast cancer, because most cases do not present with a discrete mass [75]. A method is needed to evaluate specimen accuracy immediately following CNB. In this study, our objective was to determine if confocal fluorescence microscopy can provide images with sufficient detail to evaluate the adequacy of CNB specimens with inflammatory breast cancer.

Methods:

- 1) Fresh CNB specimens were acquired within 30 minutes of the biopsy procedure. Specimens were stained with 0.01% proflavine for 1 minute prior to imaging. Grayscale confocal fluorescence images of CNB specimens were acquired and specimens were then submitted for routine histologic preparation and processing.
- 2) Grayscale confocal images of CNB specimens were false colored to resemble histologic staining by combining experimentally-determined color values for hematoxylin and eosin (H&E) [76].
- 3) To assess if images had sufficient detail to evaluate CNB specimen adequacy, a breast-dedicated pathologist evaluated invasive tumor cellularity in grayscale and false colored confocal fluorescence images and in histologic images with H&E staining.
- 4) We quantified agreement between estimates of invasive tumor cellularity with a kappa coefficient.

Results:

- 1) We acquired images of 23 CNB specimens from 23 patients with suspected inflammatory breast cancer (Figure 2.20). Confocal fluorescence images of CNB specimens were acquired in an average time of less than 2 minutes.

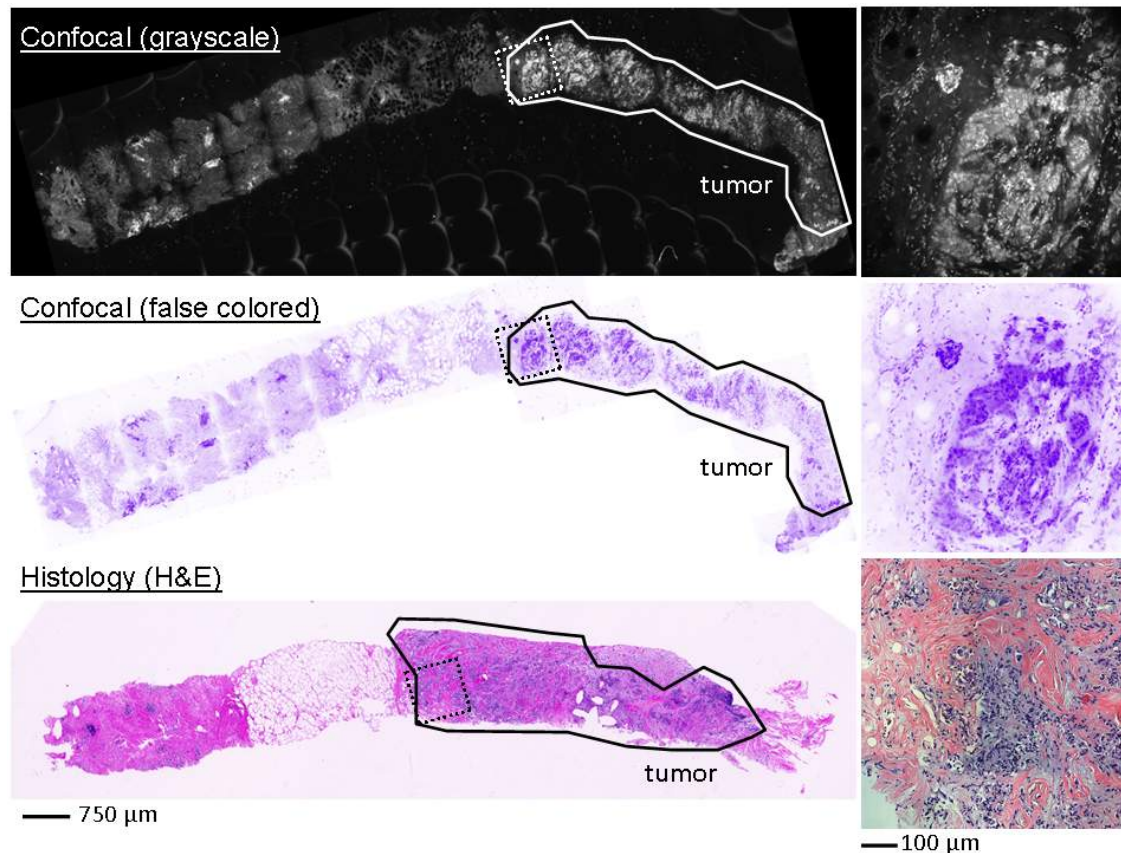


Figure 2.20 Representative core with invasive tumor and non-neoplastic tissue; 25% cellularity estimated by author S.K. in histologic image (standard H&E staining), 30% cellularity estimated in grayscale confocal fluorescence image (0.01% proflavine staining), 25% cellularity estimated in false colored confocal fluorescence image derived from grayscale image (0.01% proflavine staining). The solid outlined region indicates areas of the CNB specimen that contain invasive tumor. The scale bar at left is 750 µm. The insets at right show the border between neoplastic and non-neoplastic tissue in the CNB specimen. The locations of the insets are indicated in each core by a square with dashed lines. The scale bar at right is 100 µm.

- 2) Scatterplots of tumor cellularity estimates (Figure 2.21) show that estimated cellularity values were more consistent between histologic and grayscale confocal images ($R^2 = 0.88$) than between histologic and false colored confocal images ($R^2 = 0.61$).
- 3) The kappa coefficient calculated for agreement between histologic and grayscale confocal images indicates moderate agreement based on defined categories for kappa values [77]; $\kappa = 0.48 \pm 0.09$ ($p < 0.001$). Agreement between histologic and false colored confocal images was fair and not statistically significant; $\kappa = 0.28 \pm 0.26$ ($p = 0.14$).

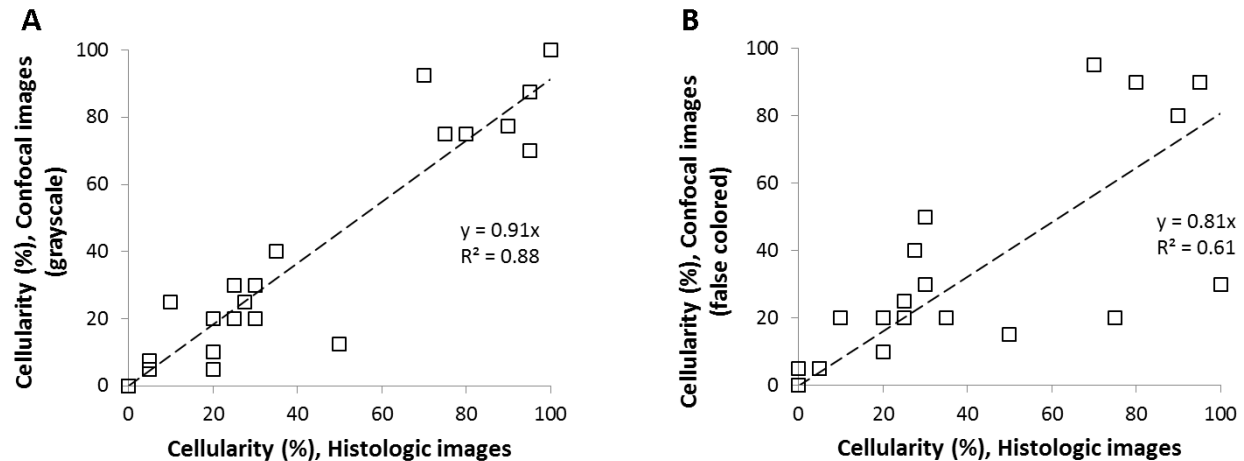


Figure 2.21 Scatterplots illustrating agreement on estimated invasive tumor cellularity between image types. Each data point represents a CNB specimen. Dashed lines represent the linear fit of the data. Pearson coefficients (R^2) quantify the linear fit of invasive tumor cellularity data. A: Invasive tumor cellularity estimates from grayscale confocal images and histologic images. B: Invasive tumor cellularity estimates from false colored confocal images and histologic images.

Conclusions:

We show that grayscale confocal images of CNB specimens require an average of only 2 minutes for acquisition. Evaluation of invasive tumor cellularity CNB specimens shows that grayscale confocal images have moderate agreement of estimated tumor cellularity compared with histologic images. We show that confocal fluorescence microscopy could potentially be used for assessment of CNB specimen adequacy, so that additional could be performed without need for a repeat visit.

Plans for year 6:

Our goals for year 6 are to:

1. Finalize our decision tree model to optimize classification of DCIS from benign ducts in confocal fluorescence images. This goal will include an evaluation of which types of ducts are being incorrectly classified.
2. Continue our analysis of adipocyte physical characteristics at sites at the margins of neoplastic and non-neoplastic tissue. We will measure adipocyte parameters at additional sites in confocal images and assess clinical parameters, including critical hormone status (i.e. estrogen receptor negative, HER2 positive, and triple negative receptor status), histologic degree of differentiation, lymph node status, and presence of distant metastases, which may be correlated with the quantified adipocyte characteristics.
3. Recruit additional readers to review the three types of images of CNB specimens in order to assess readers' performance in estimating invasive tumor cellularity in different types of images and to compare inter- and intra-reader agreement.

Our long term goal is to develop tools to facilitate early diagnosis of breast cancer by improving the ability to identify in real time whether breast biopsies have adequately sampled the lesion under investigation and to facilitate effective surgical treatment by improving the ability to adequately survey the tumor bed for residual DCIS disease.

Aim 3: *Optical quantitative biology to assess therapy response in different sub-types of breast cancer:*

The current goals of Aim 3 include adding new endpoints for more precise cancer metabolism imaging and transitioning our imaging method into a clinically translatable optical spectroscopy system. In Year 5, we have worked toward the goals presented in our previous report's Year 5 plans. We presented the results and published a conference proceeding detailing a fluorophore delivery correction method proposed in the Year 4 report (Frees, *Proc. SPIE 8947, Imaging, Manipulation, and Analysis of Biomolecules, Cells, and Tissues XII* 2014). A complete manuscript has since been prepared and submitted for review. We had previously shown that uptake of a fluorescent glucose marker, 2-NBDG, was influenced by the rate at which it was delivered to tissue. We performed *in vivo* experiments in non-tumor tissue to understand the factors affecting 2-NBDG delivery and validated that a delivery correction factor " R_D " was able to account for these experimental and physiological variables.

We have also demonstrated the feasibility of a fluorescent marker of mitochondrial membrane potential- TMRE- to further inform on cell phenotype. A combination of 2-NBDG, oxygen, and TMRE would be a reporter on both cell metabolism and overall cell "health"- namely, whether or not the cell is undergoing apoptosis, which may cause a loss of mitochondrial membrane potential. The combination of cell metabolism and apoptotic state would be a powerful endpoint for determining a tumor's response to therapy. We used optical imaging to show that

Our long-term goal is to transition our metabolic imaging method into primarily a spectroscopy/spectral imaging platform to enable clinical translation. This year, we have made great progress toward this goal by optimizing 2-NBDG and oxygenation optical spectroscopy in 4T1 and 4T07 murine mammary tumor xenografts. We have now shown that 2-NBDG fluorescence, corrected for absorption and scattering effects of tissue, is greater in tumor than in non-tumor tissue *in vivo*. A manuscript has recently been prepared and submitted on the optical spectroscopy results.

Here, we show our work in Aim 3 in two sections – High-resolution imaging and optical spectroscopy.

Part A: High resolution imaging of tumor microenvironment

Introduction:

Due to advances in genetic profiling, a host of targeted therapies has been developed to pinpoint specific mutations in cancer [78, 79]. For example, several drugs have been developed that inhibit PI3K signaling, which is dysregulated in cancers of the breast, colon, and ovary, among others [80-83]. Some of these targeted therapies can improve tumor perfusion, and hence, delivery of imaging agents such as FDG, while independently modifying intrinsic glucose demand [84]. On the other hand, highly angiogenic tumors or tumors with aberrant vascular signaling may have limited capacity for nutrient or drug delivery [85]. The limited delivery of FDG, for example, could lead to an incorrect perception that the tumor's demand for glucose is low.

Understanding a tumor's metabolic phenotype free of delivery effects has two important implications for cancer therapy. First, understanding a tumor's phenotype can help avoid overtreatment and aid in selection of an appropriate therapy (treatment planning). Second, cancer therapies such as small molecules or radiation may alter the tumor's metabolic state (response monitoring).

Our ultimate goal is to understand a tumor's "baseline" (pre-treatment) metabolic phenotype and understand how the phenotype relates to aggressiveness. Further, we are interested in the relationship between metabolic changes and long-term response to therapy. In this report, we show the progress we have made and the future work we have planned toward our goal.

Methods:

Cell Culture Maintenance and Seahorse Assay

Two murine mammary carcinoma cell lines, 4T1 and 4T07, were used in this study. Though arising from the same tumor, the cell lines have distinct different metastatic potential [86]. 4T1 cells have been shown to metastasize throughout the body to organs such as the lung, liver, bone and brain. 4T07 is able to seed into the lung and liver but it fails to engraft to form metastatic nodules. Both cell lines were cultured in Dulbecco's Modified Eagle Medium (DMEM, Gibco, Carlsbad, California) supplemented with 10% fetal bovine serum and 1% antibiotics and kept free from contaminants. Cells were passaged every 2-3 days and kept incubated at 37.0°C and 5.0% O₂.

A Seahorse Glycolytic Stress Test [Seahorse Biosciences, Massachusetts, USA] was used to measure the metabolic properties of 4T1 and 4T07 cells. Oxygen consumption rate (OCR) and extracellular acidification rate (ECAR) were measured every 11 minutes. OCR was calculated based on changes in dissolved oxygen in the cell media and ECAR was calculated based on detection of changes in free proton concentration in the cell media. Between minute 22 and minute 33 of the assay, 25mM glucose was injected to each well. Between minute 55 and minute 66, 1uM oligomycin was injected to each well. Oligomycin inhibits oxygen consumption used for ATP synthesis through phosphorylating respiration [87]. Results for each well were

normalized to the number of cells in each well. Results represent the average of 12 total wells for each cell line: assays were performed on 3 different days and each assay contained 4 replicate wells of each cell line.

Dorsal Window Chamber Implantation

All animal work was performed according to the recommendations of the Guide for the Care and Use of Laboratory Animals of the National Institutes of Health. The Duke University Institutional Animal Care and Use Committee approved all experiments (Protocol Number: A170-12-06). Female nu/nu athymic mice (NCI, Frederick, Maryland), 8-10 weeks old and weighing between 20-25g, were used for all *in vivo* studies. Murine dorsal window chambers were implanted according to the sterile procedure detailed by Palmer [88]. Briefly, mice were anesthetized via i.p. administration of ketamine (100 mg/kg) and xylazine (10 mg/kg) and implanted with a titanium dorsal window chamber (APJ Trading Co, Inc, Ventura, California). For tumor development, a 20 μ L suspension (20,000 cells) of 4T1-RFP or 4T07 cells was injected into the dorsal skin fold. No cells were injected into the mice in the normal (non-tumor) group. A glass coverslip (diameter = 12 mm, No. 2, Erie Scientific, Portsmouth, New Hampshire) was placed in the dorsal chamber to cover the exposed tissue. Animals were housed on-site at Duke University under standard 12-hour light/dark cycles. During housing, all animals were provided *ad libitum* access to food and water.

Imaging Procedure

During the 6-hour period prior to imaging, animals were fasted but allowed access to water. Immediately before imaging, blood glucose was measured from the tail vein using a FreeStyle Lite Blood Glucose Meter (Abbott Laboratories, Illinois, USA). Mice were then anesthetized with 2% v/v isoflurane mixed with air, which was reduced to 1-1.5% v/v isoflurane for maintenance. The mouse was kept on a heated stage for the duration of imaging. Prior to fluorophore injection trans-illumination images were recorded for vascular characterization. Background fluorescence images corresponding to endogenous fluorescence from cellular FAD and stromal collagen at 525nm were also recorded prior to injection [89]. A 100 μ L injection of 6mM 2-NBDLG, 6mM 2-NBDG, or 10mM 2-NBDG in sterile saline was then administered via tail vein. 2-NBDG fluorescence was excited at 470nm and collected at 525nm. Fluorescence from the tracer was recorded for 60 minutes: continuously for the first 10 minutes, every 30 seconds for the next 30 minutes and every 3 minutes for the final 20 minutes of imaging. For TMRE imaging, the procedure was consistent with 2-NBDG imaging, except the injection contained 0.1mL of 25 μ M TMRE delivered via tail vein. TMRE fluorescence was excited at 545nm and collected at 590nm.

For the hyperemia study, which was conducted to extend the range of red blood cell velocities, mice were subjected to an hour of breathing hypoxic gas (10% O₂, balance N₂) and then allowed to breathe room air for 10 minutes. Imaging began immediately following the 10-minute reoxygenation period using the imaging protocol described above. Mice receiving two perturbations (6mM and 10mM, 2-NBDG and 2-NBDLG, or baseline and post-hypoxia imaging) were imaged on two consecutive days to allow for 2-NBDG clearance and ample recovery from

anesthesia. An overview of methods is shown in Figure 3.1.

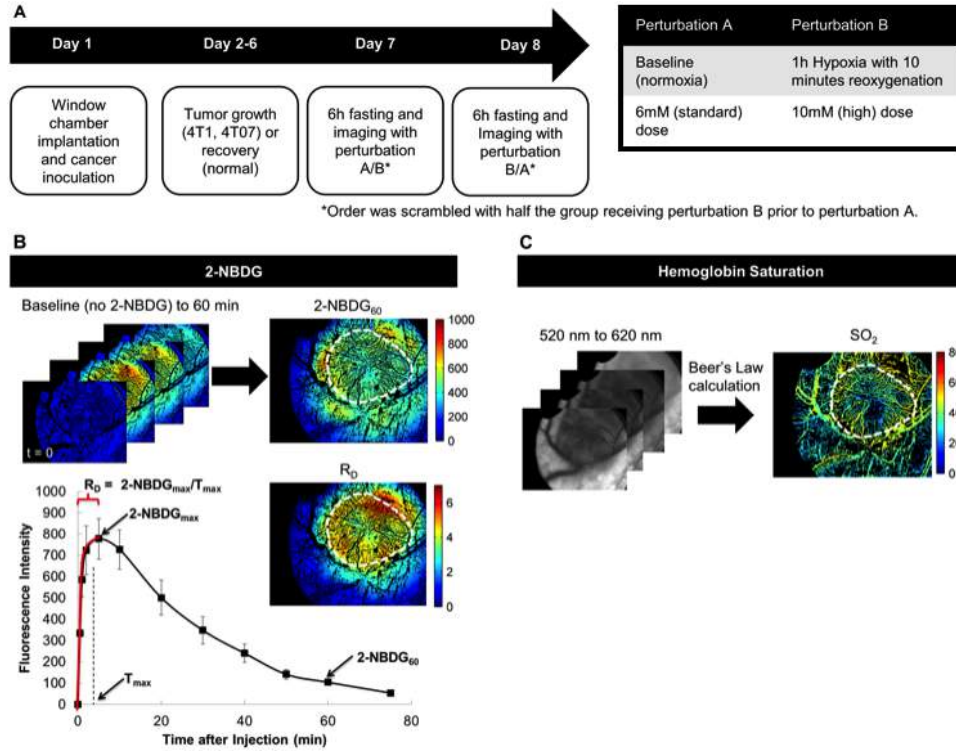


Figure 3.1- Outline of methods. (A) Timeline of imaging events. Mice that were imaged under two imaging conditions were imaged on subsequent days. The order of imaging was scrambled to minimize order effects. (B) A 6mM injection of 2-NBDG was given and imaged for at least 60 minutes, and the mean of the tumor region for each image was used to construct a kinetic curve. Images for the endpoints 2-NBDG₆₀ (2-NBDG intensity at 60 minutes) and the rate of delivery of 2-NBDG ($R_D = 2\text{-NBDG}_{60}/T_{\max}$) are shown. (C) Trans-illumination images were collected in 10nm increments from 500-600nm and used to calculate hemoglobin saturation (SO₂).

Calculation of Vascular and Metabolic Parameters

Trans-illumination images were collected in 10nm increments from 500-600nm and used to create an image cube (x,y,λ). Our procedure was previously described in detail [90]. A modified form of the Beer-Lambert law uses the extinction coefficients of [HbO₂] and [dHb] to calculate the concentrations of each absorber at each pixel. We then calculate total hemoglobin content, [THb] ([HbO₂]+[dHb]), and SO₂ ([HbO₂]/[THb]) at each pixel. The presence or absence of [THb] was used to segment the images into vascular and tissue space, respectively.

After 2-NBDG injection, fluorescence images were collected) for a period of 75 minutes. A kinetic uptake curve was created from the (x,y,t) data for each (x,y) pixel location. As shown in Figure 1, the initial rate of delivery (R_D) and glucose uptake (2-NBDG₆₀) were calculated from the time course for each pixel. R_D was calculated from the rise to the initial peak of the curve as $(I_{\max}-I_0)/T_{\max}$, where subscript 0 corresponds to a baseline image captured prior to 2-NBDG

injection. 2-NBDG₆₀ is defined as glucose uptake. We showed previously that 2-NBDG fluorescence at 60 minutes is confined to the intercellular space [90].

For 4T1 and 4T07 tumors, each endpoint (2-NBDG₆₀, R_D, 2-NBDG₆₀/R_D) was additionally parsed by SO₂. For each 2-NBDG₆₀, R_D, or 2-NBDG₆₀/R_D image, every tissue pixel in the tumor area was assigned to an SO₂ group according to the SO₂ of the nearest vascular pixel. In a given image, there were as many as five SO₂ groups: 0-10% SO₂, 10-20% SO₂, 20-40% SO₂, 40-60% SO₂, and 60-80% SO₂. The distribution of pixels for each endpoint was then represented as a survival curve (1-cumulative distribution) stratified by SO₂. Curves were then averaged within a tumor type (4T1 or 4T07). Each curve shown in Figure 5 then represents the mean of distributions of 2-NBDG₆₀, R_D, or 2-NBDG₆₀/R_D pixels at a given SO₂ level from up to 8 mice.

The blood flow imaging procedure has previously been described in detail [91]. In short, a video of individual red blood cells flowing through vessels in a non-tumor bearing window chamber was collected, taking advantage of the absorption properties of hemoglobin. A cross-correlation was performed between subsequent frames to track red blood cell movement. For each mouse, we calculated both blood velocity and 2-NBDG delivery (R_D) in the image region surrounding the vessel with the fastest blood velocity. This allowed us to achieve a wide range of blood velocities over which to correlate blood velocity with R_D. For a given mouse, the same region was selected in corresponding blood velocity and 2-NBDG images, and kept consistent between days.

Results:

Delivery-corrected 2-NBDG-uptake inversely correlates with blood glucose concentration

Figure 3.2 describes the relationship between the rate of 2-NBDG kinetics and the administered 2-NBDG dose. Figure 3.2A shows representative images of 2-NBDG uptake over 60 minutes in a normal mouse injected with either 6mM 2-NBDG or 10mM 2-NBDG on consecutive days. Figure 3.2B summarizes the results of imaging 6mM and 10mM doses in the same cohort of mice. The table shows the ratio of endpoints comparing the 10mM and 6mM groups. Each ratio was calculated on a per-mouse basis, the ratios for each mouse were averaged, and values are presented as mean ratio \pm standard error. The expected ratio of 10mM/6mM endpoints is 1.67 if all differences between groups are attributable to differences in injected dose. At 5 minutes post-injection, the fluorescence ratio of the dose groups (10mM/6mM) closely approached the expected ratio of 1.67 ($p < 0.01$), indicating that early time points report primarily on delivery. The ratio of R_D (calculated as R_{D(10mM)}/R_{D(6mM)}}) showed similar results.}

We hypothesized that correcting 2-NBDG uptake for variations in R_D due to inter-mouse variation and injected 2-NBDG dose would better represent glucose uptake. First, in Figure 3.2C we confirmed that while R_D and 2-NBDG uptake at 5 minutes post-injection (2-NBDG₀₅) are highly correlated ($R = 0.77$, $p < 0.001$), R_D and 2-NBDG at 60 minutes post injection are independent endpoints ($R = 0.20$, $p = \text{N.S.}$, not shown). To validate that delivery-corrected 2-

NBDG uptake more accurately represents glycolytic uptake, we investigated the correlation of $2\text{-NBDG}_{60}/R_D$ with blood glucose concentration in normal mice. Figure 3.2D shows a significant inverse correlation between $2\text{-NBDG}_{60}/R_D$ and blood glucose ($R=-0.61$, $p=0.02$).

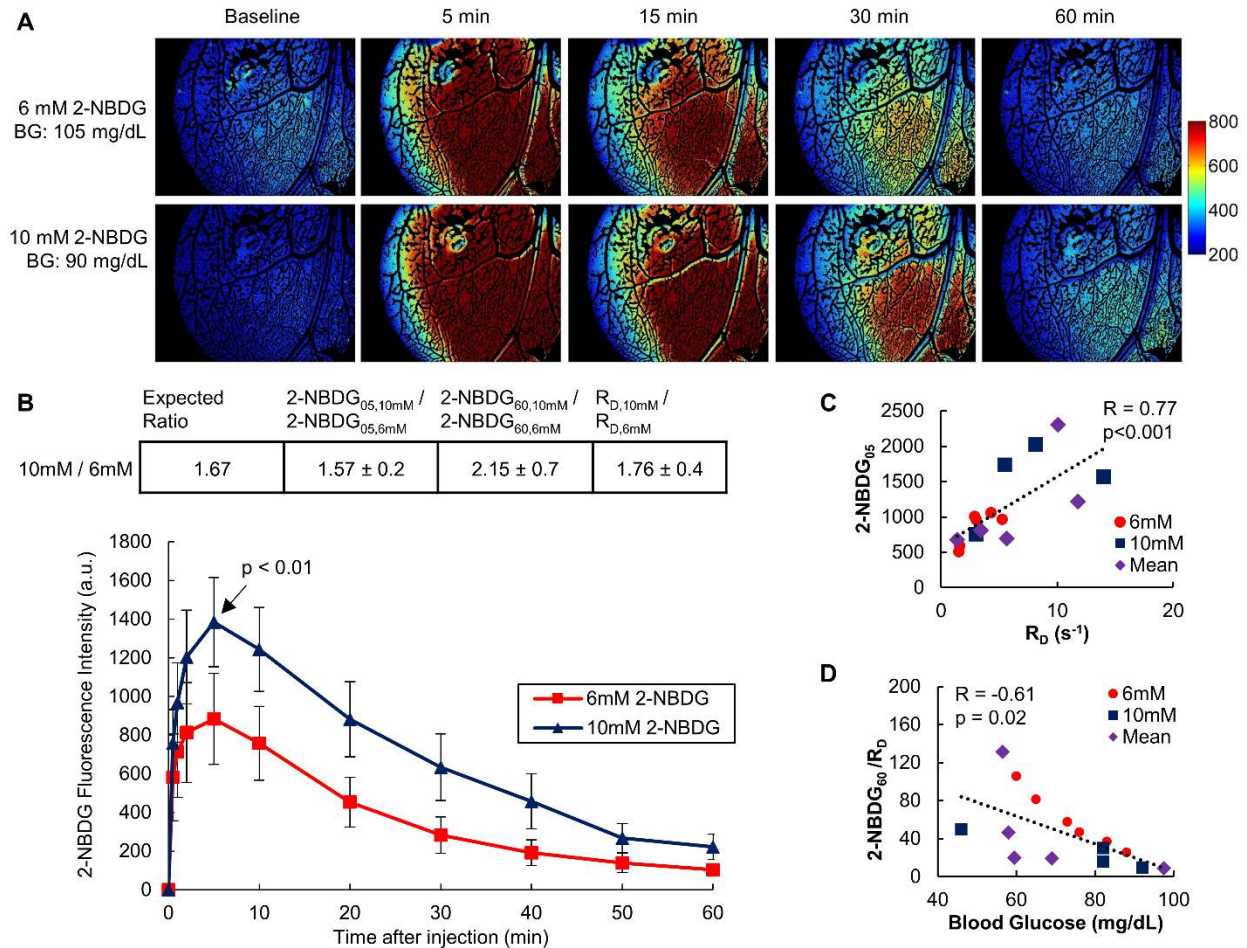


Figure 3.2. Delivery-corrected 2-NBDG uptake inversely correlates with blood glucose concentration. (A) Representative images show the kinetics of 2-NBDG uptake *in vivo* in non-tumor window chambers. The same mouse was given 6mM or 10mM 2-NBDG on subsequent days and imaged for 60 minutes following injection. (B) Averaged 2-NBDG kinetics for a cohort of mice injected with 0.1mL of either 6mM or 10mM 2-NBDG. At 5 minutes post-injection (2-NBDG_{05}), the fluorescence ratio of the dose groups ($2\text{-NBDG}_{05,10\text{mM}}/2\text{-NBDG}_{05,6\text{mM}}$) was proportional to molarity ($p<0.01$). The table shows the expected ratio of 10mM/6mM fluorescence, if all differences in fluorescence were due to dose. $2\text{-NBDG}_{05,10\text{mM}}/2\text{-NBDG}_{05,6\text{mM}}$ corresponds to the ratio of 10mM and 6mM fluorescence intensities at $t = 5$ min. The ratio $R_{D,10\text{mM}}/R_{D,6\text{mM}}$ corresponds to the rate of 2-NBDG delivery for 10mM and 6mM. Each group in panel B contains the same $n=7$ subjects. p values are from a student's paired t-test. Error bars show standard error. Values in table are mean \pm standard error. (C) R_D was strongly correlated with 2-NBDG fluorescence at 5 minutes ($p<0.001$). R_D did not correlate with 2-NBDG_{60} (not shown). (D) $2\text{-NBDG}_{60}/R_D$ was inversely correlated with baseline blood glucose in normal mice ($R=-0.61$, $p=0.02$). 2-NBDG_{60} was also correlated with blood glucose ($R=-0.52$, $p=0.05$, not

shown). For animals that received both 6mM and 10mM doses, the average values of the endpoints (2-NBDG_{05} , 2-NBDG_{60} , and $2\text{-NBDG}_{60}/R_D$) for both doses were used in calculating the correlations. These subjects are denoted by “mean” in the legend. $n=15$ mice for (C) and (D).

The rate of 2-NBDG delivery, R_D , is positively correlated with blood velocity.

The results presented in Figure 3.3 show the relationship between red blood cell velocity and the rate of 2-NBDG delivery, R_D , in corresponding image regions. Each mouse was imaged at baseline under normoxic condition (21% inspired O_2) and after 10 minutes of re-oxygenation from breathing hypoxia (10% inspired O_2). Mice were randomly assigned to undergo baseline or post-hypoxia (hyperemia) imaging first. Figure 3.3A shows representative images of a mouse at baseline and after hypoxia. There is a clear increase in flow velocity as well as R_D after hypoxia. Figure 3.3B shows that hypoxia was successfully used to significantly increase blood velocity in the tissue ($p<0.02$). Flow velocity increased in all mice after hypoxia. A corresponding significant increase in R_D was seen after hypoxia ($p<0.02$). Only one mouse did not show an increase in R_D . In Figure 3.3C, flow velocity and R_D show a strong correlation after hypoxia ($R=0.87$, $p<0.05$). At baseline, the trend was similar, but the range of flow velocities was truncated compared to the group that underwent hypoxia.

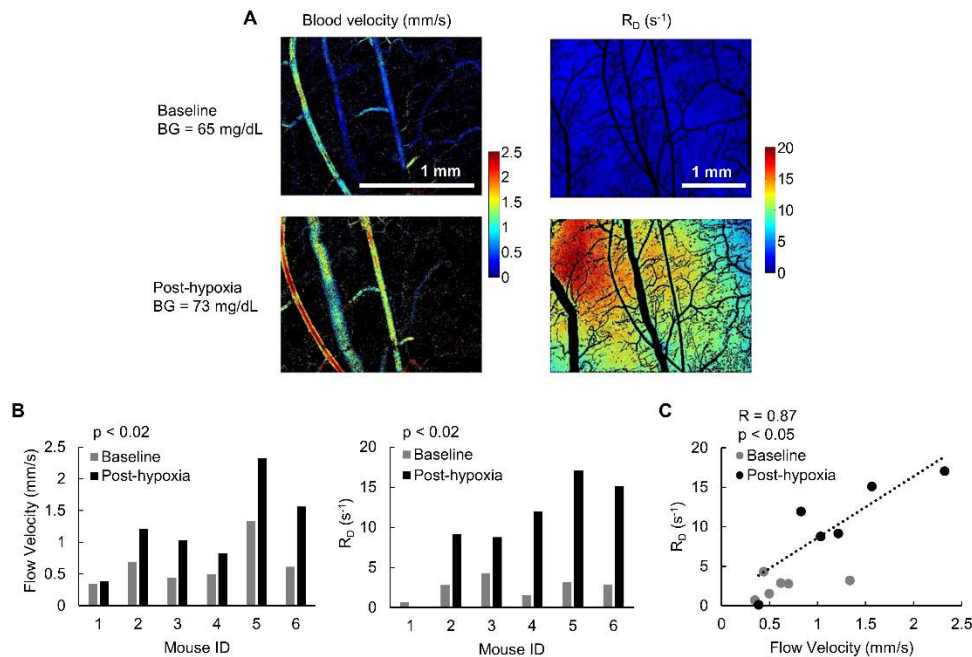


Figure 3.3. The rate of 2-NBDG delivery, R_D , is strongly correlated with blood velocity. (A) Representative images of blood velocity and the rate of 2-NBDG delivery (R_D) in a normal mouse at baseline and during reoxygenation after 1 hour of hypoxia. (B) Paired data for a set of mice at baseline and after 1 hour of hypoxia. After hypoxia, flow velocity and R_D increased significantly ($p<0.02$ for both). $N=6$ mice. (C) The rate of 2-NBDG delivery (R_D) is highly correlated with blood velocity ($R=0.87$, $p<0.05$). The trendline corresponds to the trend for post-hypoxia data only.

Delivery-corrected glucose uptake reveals distinct glycolytic phenotypes in metastatic (4T1) and non-metastatic (4T07) mammary tumors.

We used 2-NBDG₆₀/R_D to compare tumors with different metabolic phenotypes: metastatic 4T1 tumors and nonmetastatic 4T07 tumors. Figure 3.4 shows representative images of SO₂ and 2-NBDG₆₀/R_D from window chambers with 4T1 or 4T07 tumors. Figure 3.4B shows that averaging over the entire tumor regions (or regions of normal tissue) resulted in a significantly higher 2-NBDG₆₀/R_D for 4T1 than for 4T07 ($p < 0.01$). A Seahorse Glycolysis Stress Test was used on 4T1 and 4T07 cells to compare with the results of *in vivo* metabolic imaging. The glycolytic capacity, defined as the extracellular acidification rate (ECAR) after blockade of respiration by oligomycin, was significantly greater for 4T1 than for 4T07. These results are consistent with the intravital microscopy data, in which 4T1 tumors took up significantly more 2-NBDG than 4T07 tumors, both on average (Fig. 3.4B) and at each SO₂ level (Fig. 3.5B).

An elevated level of glucose uptake may lead to the assumption that the tissue is hypoxic and therefore increasingly dependent on glycolysis, but no significant difference in SO₂ was seen between groups (Fig. 3.4C). Additionally, vascular density, the total length of vessels per unit volume, was indistinguishable between 4T1 and 4T07 tumors, implying that differences in SO₂ may be attributable to changes in oxygen consumption. Results of the Seahorse Glycolytic Stress Test show that oxygen consumption rate (OCR) is comparable for 4T1 and 4T07 tumors ($p = \text{N.S.}$).

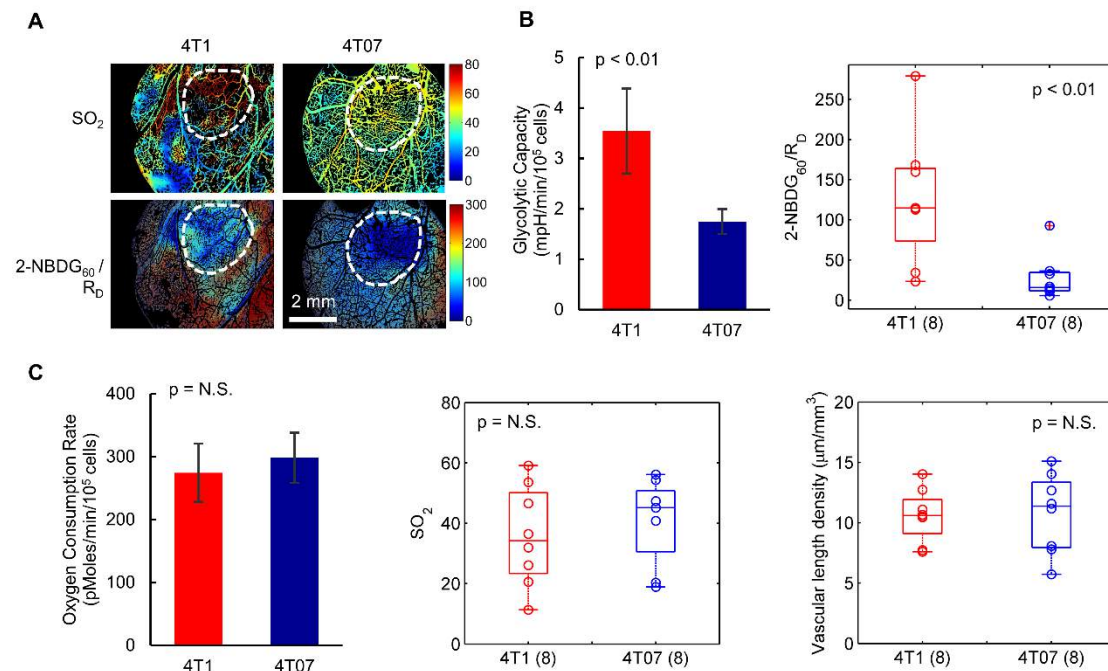


Figure 3.4. Delivery-corrected glucose uptake reveals distinct glycolytic phenotypes in metastatic (4T1) and non-metastatic (4T07) mammary tumors. (A) Representative images of vascular oxygen saturation (SO₂) and delivery-corrected 2-NBDG (2-NBDG₆₀/R_D) for a 4T1 tumor and a 4T07 tumor, *in vivo*. (B) 2-NBDG₆₀/R_D showed contrast in glucose uptake between

metastatic 4T1 and non-metastatic 4T07 tumors *in vivo* ($p < 0.01$). A Seahorse Glycolysis Stress Test also revealed that the glycolytic capacity, defined as extracellular acidification rate (ECAR) after blockade of respiration by oligomycin, was significantly greater for 4T1 than for 4T07 ($p < 0.01$). (C) Mean vascular oxygen saturation (SO_2) was comparable for 4T07 and 4T1 tumors in window chambers ($p = N.S.$). Vascular density was indistinguishable between tumor lines ($p = N.S.$). A Seahorse Glycolysis Stress Test showed that oxygen consumption rate (OCR) is comparable for 4T1 and 4T07 tumors ($p = N.S.$). Number of mice per group indicated by group name on axis. For Seahorse results, $n = 12$ cell samples from 3 distinct assays. Midline of box plots show median, box edges correspond to 25th and 75th percentiles, and scatter points show all data values.

The ratio 2-NBDG₆₀/R_D facilitates assessment of glucose uptake in heterogeneous regions of metastatic mammary tumors.

Tumor oxygenation plays an important role in metabolism, and varies not only across tumor lines but also within a tumor [92, 93]. We parsed our delivery-corrected glucose demand endpoint with vascular oxygenation to investigate metabolic heterogeneity in tumors. First we compared 4T1 and 4T07 tumors with mean vascular oxygenation values in different SO_2 ranges, shown in Figure 3.5A. After correcting for delivery, the hypoxic 4T1 tumor (mean $SO_2 = 11\%$) showed localized regions of high 2-NBDG₆₀/R_D uptake not seen in the 4T1 with intermediate SO_2 (mean $SO_2 = 36\%$) nor in the well-oxygenated 4T07. The well-oxygenated 4T07 tumor (mean $SO_2 = 59\%$) showed an appreciably decreased 2-NBDG₆₀/R_D compared to either of the 4T1 tumors. The emerging trend suggested that 2-NBDG/R_D increased as average SO_2 decreased.

We then analyzed each tumor at five levels of vascular oxygenation (SO_2) to identify if hypoxic regions were responsible for increased mean glucose uptake in 4T1 tumors relative to 4T07 tumors. Figure 3.5B shows 2-NBDG₆₀, R_D, and 2-NBDG₆₀/R_D for 4T07 tumors and 4T1 tumors, respectively, across vascular oxygenation levels: 0-10% SO_2 , 10-20% SO_2 , 20-40% SO_2 , 40-60% SO_2 , and 60-80% SO_2 . Each curve represents the mean of distributions at a given SO_2 level from up to 8 mice (group numbers listed in parentheses in legend). Interestingly, only two 4T07 mice exhibited vessels with the lowest levels of oxygenation (0-10% SO_2 and 10-20% SO_2), and therefore were not shown. Similarly, only two 4T1 mice exhibited vessel regions of 60-80% SO_2 and were therefore excluded.

Within the 4T1 tumors, hypoxic regions had decreased 2-NBDG delivery compared to well-oxygenated regions ($p < 0.01$, 0-10% SO_2 v. 40-60% SO_2). There was no difference in uptake between other $SO_{2,4T1}$ groups. R_D was also lowest in hypoxic regions of 4T1 ($p < 0.05$ or $p < 0.01$ for $0 < SO_{2,4T1} < 10$ vs. $20 < SO_{2,4T1} < 40$ or $40 < SO_{2,4T1} < 60$, respectively). The ratio 2-NBDG₆₀/R_D within 4T1 significantly decreased as vascular oxygenation increased reflecting the Pasteur effect ($p < 0.01$ for $0 < SO_{2,4T1} < 10$ vs. $40 < SO_{2,4T1} < 60$). 4T07 tumors showed a different trend in uptake. 2-NBDG₆₀ increased from the highest to the lowest SO_2 levels of 4T07 tumors ($p < 0.01$ for $20 < SO_{2,4T07} < 40$ vs. $60 < SO_{2,4T07} < 80$) and there was no difference in R_D across $SO_{2,4T07}$ levels. After correction, 2-NBDG₆₀/R_D in 4T07 followed a similar trend as in 4T1. 2-NBDG₆₀/R_D was lowest for $60 < SO_{2,4T07} < 80$ compared to both other $SO_{2,4T07}$ ($p < 0.01$).

Comparison between tumor lines showed that 2-NBDG₆₀ was higher for all 4T1 groups than for all 4T07 ($p<0.01$). On the other hand, delivery (R_D) for the best oxygenated 4T07 groups ($40<SO_{2,4T07}<60$ and $60<SO_{2,4T07}<80$) was greater than for all 4T1 groups ($p<0.01$ for all groups except $40<SO_{2,4T1}<60$ vs. $60<SO_{2,4T07}<80$ where $p<0.06$). At all SO_2 levels, 2-NBDG₆₀/ R_D of 4T1 tumors exceeded that of 4T07 tumors ($p<0.01$ for all $SO_{2,4T1}$ compared to all $SO_{2,4T07}$). This analysis confirmed that 4T1 tumors display increased glucose metabolism regardless of oxygen status, not only in response to hypoxia. On the other hand, the low demand for and sufficient delivery of 2-NBDG to 4T07 made them statistically indistinguishable from normal tissue (not shown).

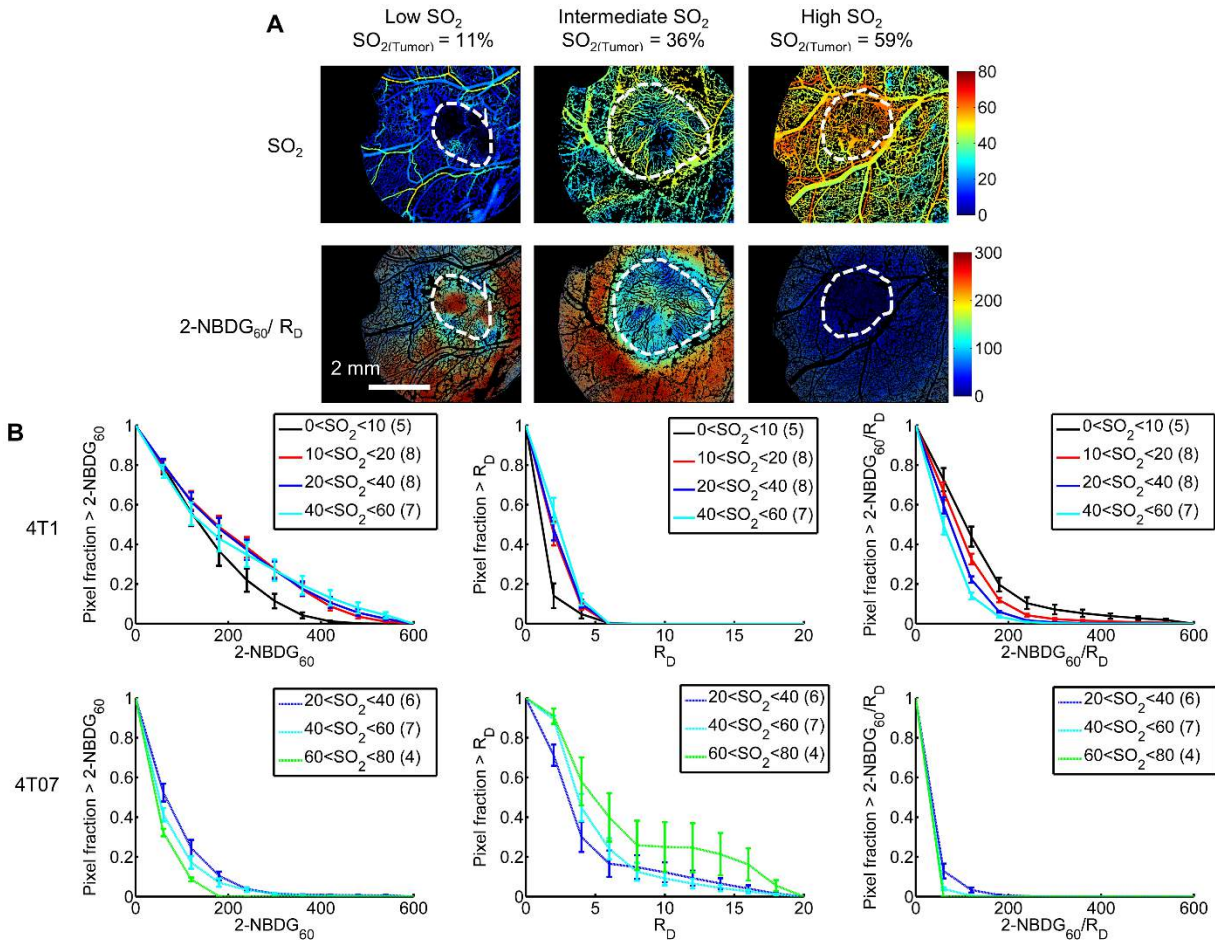


Figure 3.5. The ratio 2-NBDG/ R_D facilitates assessment of glucose demand in heterogeneous regions of metastatic mammary tumors. (A) Representative images of vascular oxygenation (SO_2) and delivery-corrected 2-NBDG ($2-NBDG_{60}/R_D$) for a 4T1 tumor with low mean SO_2 , a 4T1 tumor with intermediate mean SO_2 , and a 4T07 with high mean SO_2 . (B) Survival curves (1-cumulative distributions) show 2-NBDG₆₀, R_D , and 2-NBDG₆₀/ R_D for regions of distinct SO_2 (%) in 4T07 and 4T1 tumors. For 4T1, 2-NBDG₆₀ is lower for $0<SO_{2,4T1}<10$ regions than for any other $SO_{2,4T1}$ ($p=N.S.$). Significantly lower rates of R_D are seen for the $0<SO_{2,4T1}<10$ group than for well-oxygenated 4T1 regions ($p<0.05$ or $p<0.01$ for $0<SO_{2,4T1}<10$ vs. $20<SO_{2,4T1}<40$ or $40<SO_{2,4T1}<60$, respectively). After correction for low R_D , 2-NBDG₆₀/ R_D

increased slightly but significantly in hypoxic regions ($p < 0.01$ for $0 < \text{SO}_{2,4\text{T}1} < 10$ vs. $40 < \text{SO}_{2,4\text{T}1} < 60$). For 4T07, 2-NBDG uptake for the highest $\text{SO}_{2,4\text{T}07}$ regions decreased compared to the lowest $\text{SO}_{2,4\text{T}07}$ ($p < 0.01$ for all $20 < \text{SO}_{2,4\text{T}07} < 40$ vs. $60 < \text{SO}_{2,4\text{T}1} < 80$). R_D is indistinguishable between $\text{SO}_{2,4\text{T}07}$ levels. After correction by R_D , $2\text{-NBDG}_{60}/R_D$ is lowest for $60 < \text{SO}_{2,4\text{T}07} < 80$ ($p < 0.01$). Comparison between 4T1 and 4T07 shows that 2-NBDG_{60} is higher for all $\text{SO}_{2,4\text{T}1}$ than all $\text{SO}_{2,4\text{T}07}$ ($p < 0.01$). On the other hand, R_D for the best oxygenated 4T07 groups ($40 < \text{SO}_{2,4\text{T}07} < 60$ and $60 < \text{SO}_{2,4\text{T}07} < 80$) is greater than for all 4T1 groups ($p < 0.01$ for all groups except $40 < \text{SO}_{2,4\text{T}1} < 60$ vs. $60 < \text{SO}_{2,4\text{T}07} < 80$ where $p < 0.06$). After correction by R_D , $2\text{-NBDG}_{60}/R_D$ is higher for all $\text{SO}_{2,4\text{T}1}$ than all $\text{SO}_{2,4\text{T}07}$ ($p < 0.01$ for all $\text{SO}_{2,4\text{T}1}$ compared to all $\text{SO}_{2,4\text{T}07}$). Number of mice per group indicated by group name in legend.

The mitochondrial membrane potential probe TMRE responds to hypoxic perturbation in vivo in non-tumor tissue.

We saw that TMRE signal decreased in each of four window chambers under hypoxic conditions compared to normoxic conditions. Representative images are shown in [Figure 3.6](#). Interestingly, the kinetics we have seen for TMRE are very different from previously observed 2-NBDG kinetics. Fluorescence peaks quickly, followed by a decrease and subsequent rise to a plateau. We further saw that the biggest difference in signal was observed 48 minutes post-injection. The ratio of (hypoxia fluorescence at 48 min)/(normoxia fluorescence at 48 min) was very consistent across mice; the ratio was 0.36 ± 0.04 (Mean \pm S.D.), and the decrease from normoxia to hypoxia was significant ($p < 0.02$). Full results are shown in **Error! Reference source not found..** It should be noted that we described here normoxia imaging on day 1 and hypoxia imaging on day 2, but the order will be randomly scrambled across the group. The results indicated that our imaging of TMRE has shown promise for monitoring of changes in the abundance of oxidative phosphorylation in tissue. Our results were expected, as hypoxia has been shown to be effective for decreasing mitochondrial membrane potential, and in turn, TMRE uptake in HCT116 colorectal cancer [94].

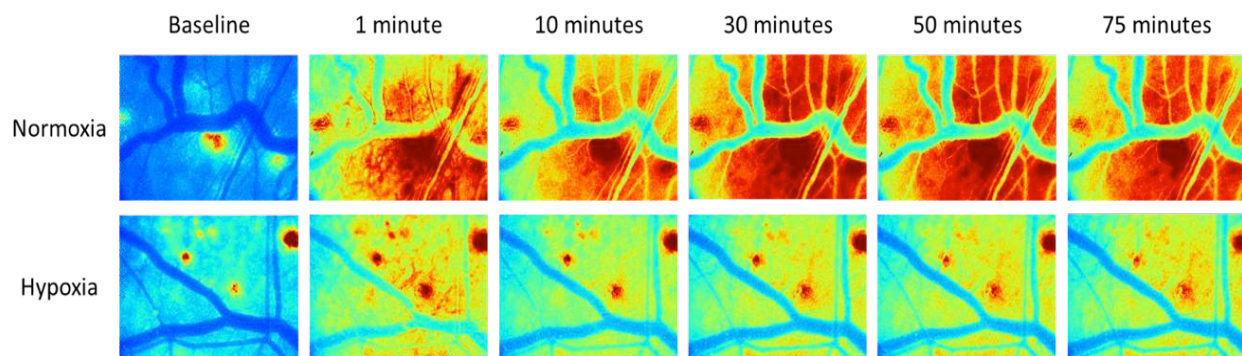


Figure 3.6. Representative images of TMRE uptake in a non-tumor dorsal window chamber. The mouse was allowed to breathe room air (top row) or 10% O_2 during imaging. TMRE uptake decreased significantly under hypoxic conditions.

Part B: Optical spectroscopy for clinical translation

Introduction:

Although high-resolution intra-vital microscopy provides a powerful pre-clinical tool to quantify the relationship between SO_2 and glucose uptake in the tumor microenvironment, it is not readily translatable to the characterization of solid tumors. To address this issue, we have developed a quantitative optical spectroscopy technique to measure the scattering, absorption and fluorescence of turbid media such as thick tissues [95, 96]. Specifically, we have developed a series of fast, scalable, Monte Carlo (MC) inverse models that model light-tissue interaction for the specific optical fiber-probe geometry used for measurement with the optical spectroscopy device. We have previously applied this technology to characterize the SO_2 and [THb] of pre-malignant and malignant tissue in both pre-clinical models [97, 98] and human subjects [99-101]. Measurements of SO_2 have been shown to be strongly associated with tissue pO_2 [102]. We have also quantified 2-NBDG concentrations in tissue-simulating phantoms that contained either single or multiple fluorophores and demonstrated that the MC fluorescence model effectively removes the non-linear effects of absorption and scattering on the fluorescence, thus yielding a linear relationship between 2-NBDG fluorescence intensity and concentration [103].

The objective of the current study was two-fold: 1. Demonstrate the ability of a fast and non-invasive method to simultaneously measure SO_2 and glucose uptake (using 2-NBDG) in normal tissues and in solid tumors in pre-clinical models *in vivo*, and 2. Characterize differences in the relationship between SO_2 and glucose uptake in 2 sibling murine breast cancer lines that differ in their metastatic potential as well as normal, non-tumor bearing tissue [104, 105]. This goal facilitates translation of findings from high resolution imaging of the tumor microenvironment to rapid, point of care technology.

Methods:

In vivo studies

8 to 10 weeks old female athymic nude mice (nu/nu, NCI, Frederic, Maryland) weighing between 20 and 25 g were used for these studies. All animals were housed in an on-site facility with *ad libitum* access to food and water and standard 12-hour light/dark cycles. Normal mice with no tumors were used for the fasting and dosage experiments. Groups of five mice were fasted for 6 hours and injected with 6, 12, 24, or 36 mM of 2-NBDG (2 – 16 mg/ml or 8-48 mg/kg of body weight). For the fasting experiments, spectroscopic measurements of reflectance and fluorescence were performed in the morning on non-fasted mice. 2 days later, mice were fasted overnight for 12 hours prior to spectroscopic measurements. Blood glucose levels were measured by a tail-vein prick using a commercially available blood glucose meter (Freestyle), prior to optical measurements. Mice were not anesthetized during measurement of blood glucose to avoid effects of isoflurane on initial blood glucose levels. During the 12-hour fasting period, animals were only provided water. A separate group of 10 mice received a subcutaneous injection of 4T1 (N=5) or 4T07 (N=5) cells (1 million cells in 0.1 ml) in the right flank. Once the tumor volume was approximately 100 mm³, mice were fasted for 6 hours,

anesthetized with isofluorane, and injected with a 6 mM dose of 2-NBDG. Mice in the normoxic group were exposed to isofluorane mixed with room air, and mice in the hypoxic group were exposed to isofluorane mixed with 10% Oxygen-90% Nitrogen.

Optical measurements

The optical spectroscopy instrument has been described previously [106] and consists of a 450 Watt Xenon lamp coupled to a monochromator (Jobin Yvon Horiba), a fiber-optic probe (designed in-house and custom built by RoMack Inc.), a spectrograph (Jobin Yvon Horiba), and a 2D CCD camera (Jobin Yvon Horiba). The fiber-optic probe consisted of 19 illumination fibers (diameter = 200 μm ; NA = 0.22) surrounded by 18 collection fibers (diameter = 200 μm ; NA = 0.22). The sensing depth of the probe was estimated from tissue-like phantoms to be approximately 1.5 mm.

The optical instrument was always allowed to warm up for at least 30 minutes before initiating measurements. The optical probe was stabilized to avoid probe bending--associated changes in lamp throughput and systematic errors [107]. Because changes in lamp throughput could affect optical measurements, reflectance and fluorescence spectra on each day were calibrated using a 20% reflectance standard (Spectralon, Labsphere) and a fluorescence reflectance standard (USF 210-010, Labsphere Inc.), respectively. Specifically, tissue reflectance spectra were divided, wavelength-by-wavelength, by the reflectance spectrum measured from the standard. The reflectance standard measurement also corrects the tissue reflectance spectra for the wavelength response of different system components. Fluorescence spectra were divided by the fluorescence intensity at 540 nm measured from the fluorescence standard. To correct the fluorescence spectra for wavelength response, the fluorescence spectrum from a NIST-approved tungsten calibration lamp (Optronic Laboratories Inc., Orlando, FL) was measured using the optical instrument and divided by the manufacturer-provided spectrum to obtain a correction factor. Tissue fluorescence spectra were multiplied by this correction factor to calibrate the wavelength-dependent response of the monochromators, fiber bundle and PMT. Because 1-3 mice were imaged on a given day for a total duration of 5 hours, standard measurements were performed prior to optical measurements on each mouse.

Mice were anesthetized using a mixture of isofluorane and room air (1.5% v/v) throughout the course of the optical measurements. Optical measurements were obtained by placing the fiber-optic probe on the skin covering the right flank of the mouse. Optical measurements on each mouse were acquired continuously for a period of 75 minutes. The probe was stabilized with a clamp and care was taken to ensure that pressure was not applied on tissue. Reflectance spectra were acquired from 390 – 650 nm (acquisition time: 0.05 s) and fluorescence emission spectra were acquired from 510 – 620 nm (acquisition time: 5 s) using excitation at 490 nm. Although 2-NBDG is maximally excited at ~ 475 nm, an excitation wavelength of 490 nm was used to minimize fluorescence excitation of endogenous FAD. Prior to 2-NBDG injection, baseline reflectance and fluorescence spectra were measured from the tissue site of interest. All measurements for both phantom and animal studies were acquired in a dark room.

Measurement of tissue optical properties and native fluorescence

A scalable inverse Monte Carlo model was used to extract tissue scattering, absorption and native fluorescence of 2-NBDG from *in vivo* optical measurements. The reflectance and fluorescence-based inverse Monte Carlo models have been described in detail previously [95, 96]. Further, the fluorescence model has been validated for both single and multiple fluorophores in the sampled medium [103]. A flowchart describing the entire process is presented in Figure 3.7. Because the Monte Carlo model operates on an absolute scale and the tissue measurements are relative to a reflectance standard, a reference phantom with known optical properties is necessary to accurately scale tissue optical properties. Based on a series of phantom studies using the optical instrument and fiber-optic probe described here, a reference phantom was selected based on low errors in extracting tissue absorption and scattering. The inverse model assumes oxygenated hemoglobin, deoxygenated hemoglobin, and overlying rat skin as absorbers, and utilizes the widely used extinction coefficients documented by Scott Prahl to calculate absorption coefficients (units of cm^{-1}). Tissue scattering is assumed to be primarily due to cells and its associated components and is calculated from scatterer size, density, and the refractive index of the scatterer and surrounding medium using Mie theory for spherical particles. The inverse model works by adaptively fitting the modeled diffuse reflectance to the measured tissue diffuse reflectance until the sum of squares error between the modeled and measured diffuse reflectance is minimized. We used the fluorescence intensity at 60 minutes – 2-NBDG₆₀ to indicate glycolytic demand by the tumor.

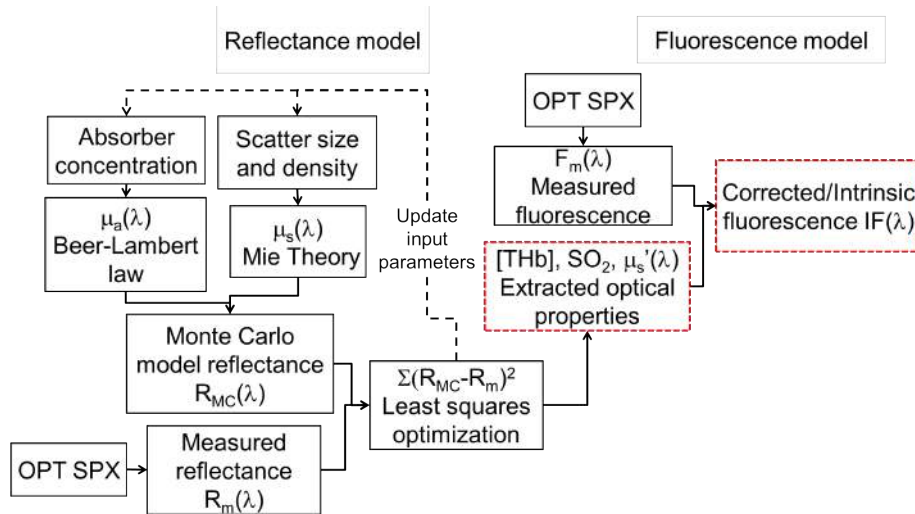


Figure 3.7. Monte Carlo modeling. Flowchart illustrating the working of the MC reflectance and fluorescence models to extract optical properties and distortion-free fluorescence from tissue.

Results:

Optical measures of SO_2 are significantly lower in tumors compared with normal tissue

Figure 3.8A shows representative reflectance spectra (normalized to 600 nm) measured from three different groups of mice – non-tumor bearing and 4T1 and 4T07 murine mammary tumor xenografts. These spectra were measured prior to tail-vein injection of a 6mM (2mg/ml) dose of

2-NBDG. Open circles represent the measured reflectance and the solid lines represent the MC reflectance model fits to the data. Based on these model fits, the extracted absorption spectrum for each reflectance measurement is presented in Fig. 3.8B. The absorption levels are significantly higher in the 4T1 tumor compared to that in normal tissue and the 4T07 tumors. SO_2 levels, calculated from the relative concentrations of oxygenated and deoxygenated hemoglobin, are significantly lower in the 4T1 and 4T07 tumors compared with normal tissue (Fig. 3.8C). Fig. 3.8D shows the effect of 2-NBDG injection on SO_2 within tissue and tumors. A small but insignificant increase in SO_2 was observed in normal tissue and the 4T1 tumors at 60 minutes relative to baseline (prior to injection), which is the time point at which 2-NBDG-fluorescence stabilizes from transient perfusion-mediated effects. A small but insignificant change in SO_2 was observed in the 4T07 tumors. The fold-increase in SO_2 was not significantly correlated with 2-NBDG-fluorescence at 60 minutes within normal tissue or tumors (data not shown; $r = 0.07$; $p = 0.78$). The oxygen consumption rates of both cell lines were calculated using a glycolysis stress test, and were found to be statistically similar (fig. 3.8E).

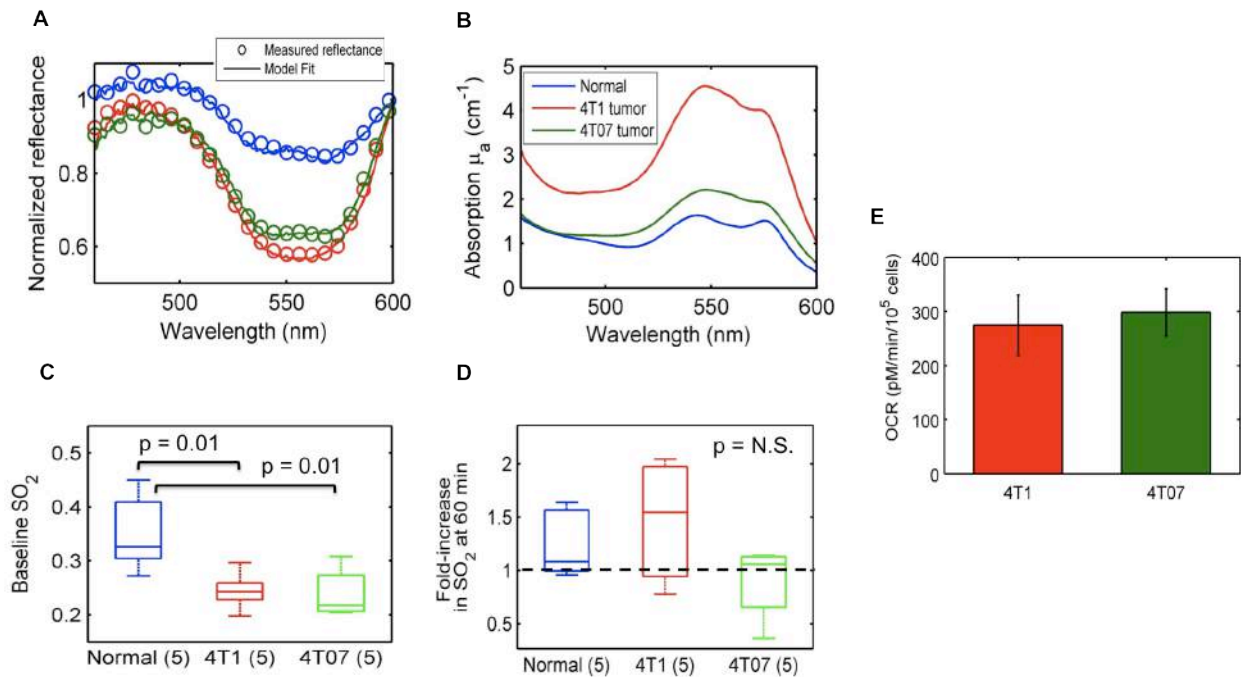


Figure 3.8. Optical measures of SO_2 are significantly lower in tumors compared with normal tissue. **A.** Representative reflectance spectra (open circles) from normal tissue (blue), 4T1 (red) and 4T07 (green) murine mammary tumors, and MC model fits (solid line). **B.** Extracted absorption spectra for the reflectance spectra shown in 3.8A illustrate higher absorption in the 4T1 tumor compared with the normal and 4T07 tumor. **C.** Baseline oxygenation levels are significantly lower in 4T1 and 4T07 tumors compared with normal tissue. **D.** The injection of 2-NBDG causes an insignificant increase in SO_2 in normal tissue and 4T1 tumors. **E.** Oxygen consumption rates (OCR) of 4T1 and 4T07 cells are statistically similar. Measurements were made using a Seahorse Glycolysis stress test. Data represent $n=12$ cell samples from 3 distinct assays. Error bars represent standard error of the mean.

Intrinsic tissue fluorescence corrected for absorption and scattering shows a significant increase in 2-NBDG₆₀ in 4T1 tumors relative to normal tissue

Measured 2-NBDG-fluorescence spectra at 60 minutes are shown in Fig. 3.9A. The fluorescence intensities from the three representative mice (normal, 4T1, and 4T07) are similar; however, there is a visible distortion of the fluorescence line shape measured from the 4T1 tumor in the wavelength range corresponding to hemoglobin absorption (560-600 nm). Normalized versions of the same spectra illustrate the effect of distortion in better detail (Fig. 3.9B). There are no significant differences in 2-NBDG₆₀ between the three groups (Fig. 3.9C). Correction with the MC model removes the distortion due to hemoglobin from the fluorescence line shape, and the recovered line shape is a closer representation of the actual 2-NBDG spectrum (Fig. 3.9E). Corrected 2-NBDG₆₀ is significantly higher in the 4T1 tumors compared with normal tissue (Fig. 3.9F). Although the median value of the 4T07 tumors was similar to that of the 4T1 tumors, there was no significant difference in 2-NBDG₆₀ between the 4T07 tumors and the other two groups. This was primarily due to the large variance in fluorescence intensity in the 4T07 group in both the measured and corrected forms. Analysis of the extracellular acidification rate (ECAR) using glycolysis stress tests showed no significant differences between 4T1 and 4T07 cells (fig. 3.9G).

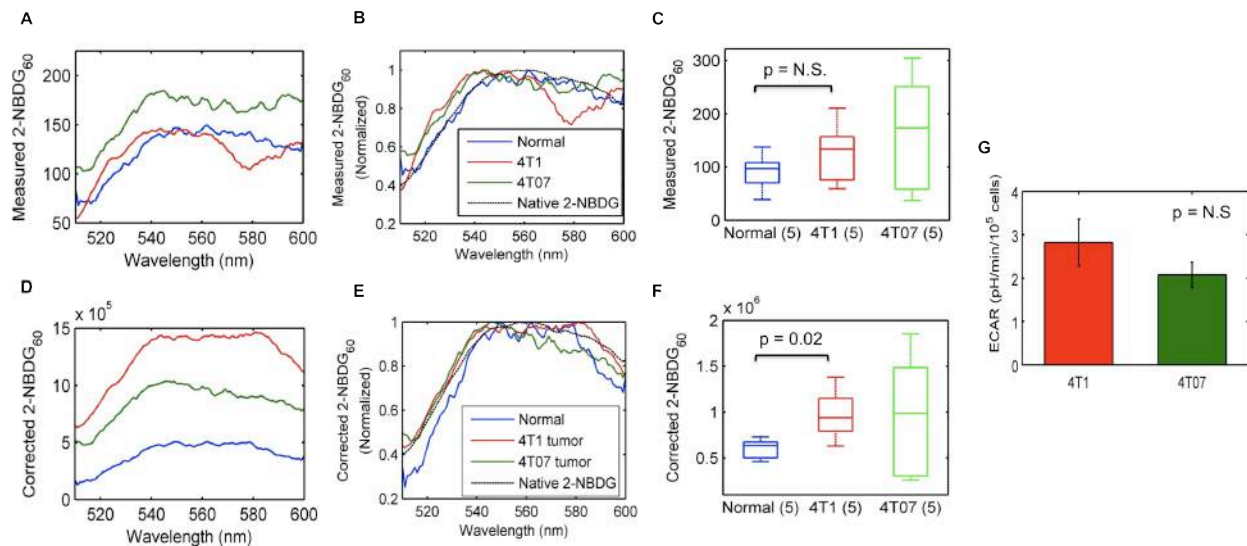


Figure 3.9. Intrinsic tissue fluorescence corrected for absorption and scattering improves 2-NBDG contrast between 4T1 tumors and normal tissue. **A.** Measured 2-NBDG₆₀ from the 4T1 and 4T07 tumors is distorted by hemoglobin absorption, and is on par with fluorescence from normal tissue. A normal tissue data-point and representative tumors with similar measured fluorescence values were selected to illustrate the effect of correction. **B.** Normalized spectra of measured 2-NBDG₆₀ illustrate the distortion in better detail. **C.** Measured 2-NBDG₆₀ is not significantly different between the different groups. **D.** Correction with the MC fluorescence model removes hemoglobin-induced distortions and improves contrast between normal and tumor. **E.** Corrected 2-NBDG₆₀ spectra from normal tissue, a 4T1 tumor, and a 4T07 tumor shown in 3.9D, normalized to their respective maxima are presented along with a true 2-NBDG

fluorescence measurement, illustrating good agreement between the extracted in vivo spectral line shapes and native 2-NBDG. **F.** Corrected 2-NBDG₆₀ is significantly higher in 4T1 tumors compared with normal tissue ($p = 0.02$). Although mean 2-NBDG₆₀ in 4T07 tumors is higher compared with normal tissue, this is not statistically significant. **G.** The extracellular acidification rate (ECAR) of 4T1 and 4T07 cells, as calculated with a Seahorse Glycolysis stress test, is not significantly different. Data represent $n=12$ cell samples from 3 distinct assays. Error bars represent standard error of the mean.

2-NBDG₆₀ increases with a decrease in blood glucose levels

Figure 3.10A presents representative kinetic profiles of 2-NBDG uptake for three different periods of food deprivation in mice – 0, 6, and 12 hours. All measurements were made on non-tumor-bearing mice that were injected with a 6 mM (2 mg/ml) dose of 2-NBDG. Maximum 2-NBDG-fluorescence is similar in all three fasting groups (0, 6, and 12 hours). 2-NBDG₆₀ is significantly higher in the 6-h and 12-h fasting groups compared with the 0-h fasting group (Fig. 3.10B; $p = 0.02$). However, there were no significant differences in fluorescence between the 6 and 12-h fasting groups. In a separate cohort of mice, we determined blood glucose levels for different fasting durations ranging from 0 – 12 hours. Mice fasted for 6 hours showed a statistically significant decrease in blood glucose levels relative to baseline blood glucose levels (Fig. 3.10C). Fasting for 12 hours did not lead to any further decrease in blood glucose levels. These data illustrate that changes in 2-NBDG₆₀ for the different fasting durations are consistent with blood glucose dynamics over a similar time period.

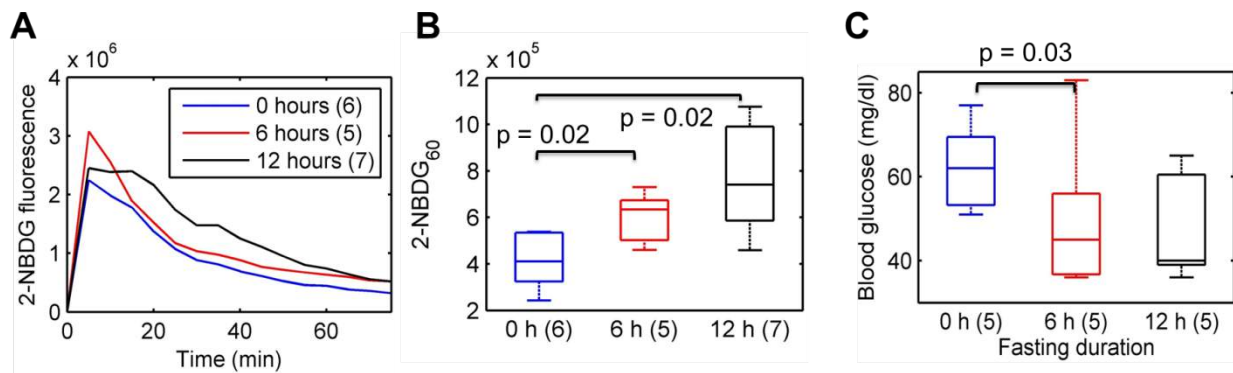


Figure 3.10. 2-NBDG₆₀ is sensitive to a decrease in blood glucose levels. A. Representative 2-NBDG kinetic profiles for 3 different fasting groups of mice after injection of a 6 mM (2mg/ml) dose via the tail-vein. There are no significant differences in maximum 2-NBDG-fluorescence between the different fasting groups, confirming that the delivery of 2-NBDG is similar across all animal groups. **B.** 2-NBDG₆₀ is significantly higher in mice fasted for 6 hours and 12 hours compared with mice that were not fasted ($p = 0.02$). There are no significant differences between the 6 and 12-hour fasting groups. **C.** Blood glucose measurements were performed using a Freestyle Lite monitor by drawing 3 μ l of blood from the tail of a separate cohort of mice ($n = 5$). Fasting for 6 hours led to a significant decrease in blood glucose levels. However, fasting for 12 hours did not lead to any further decrease in blood glucose levels. Statistical analysis was conducted using Wilcoxon rank sum tests.

2-NBDG₆₀ and SO₂ measurements reveal an inverse relationship between glucose uptake and oxygen saturation in 4T1 and 4T07 murine mammary tumors

Figures 3.11A and 3.11B present the SO₂ and 2-NBDG₆₀ for the three tissue and tumor types – normal tissue, 4T1 tumor-bearing mice that were breathing room air (or 21% O₂) and 4T1-tumor bearing mice that were breathing 10% O₂ (rest nitrogen). SO₂ is significantly higher in normal, non-tumor-bearing mice compared with all other groups. 2-NBDG₆₀ is significantly higher in the 4T1 tumors exposed to 21% O₂ and 10% O₂ compared with normal tissue. The median SO₂ of hypoxic 4T1 tumors was lower than their normoxic counterparts, but not statistically significant (Wilcoxon sign rank; $p = 0.43$). Figures 3.11C and 3.11D shows the results of a Seahorse Glycolytic Stress Test in 4T1 cells. After treatment with oligomycin, which prevents respiration, OCR decreased significantly in 4T1 cells ($p < 0.01$). *In vivo*, we observe a similar decrease in SO₂ after hypoxia. The decrease in OCR in 4T1 cells after treatment with oligomycin was accompanied by a small but insignificant increase in ECAR. Figure 3.11E illustrates the relationship between the two parameters for all tissue types. When the 4T1 tumors were exposed to hypoxia, the median 2-NBDG₆₀ increased for the hypoxic group; however, this increase was not statistically significant (Wilcoxon sign rank; $p = 0.43$). When the 4T1 tumors exposed to normoxia are considered along with the hypoxic group, 2-NBDG₆₀ is inversely related with SO₂ ($r = -0.73$; $p = 0.01$). An examination of 4T1 tumor volumes indicated a positive correlation between 2-NBDG₆₀ and tumor volume (fig. 3.12F; $r = 0.79$; $p = 0.07$).

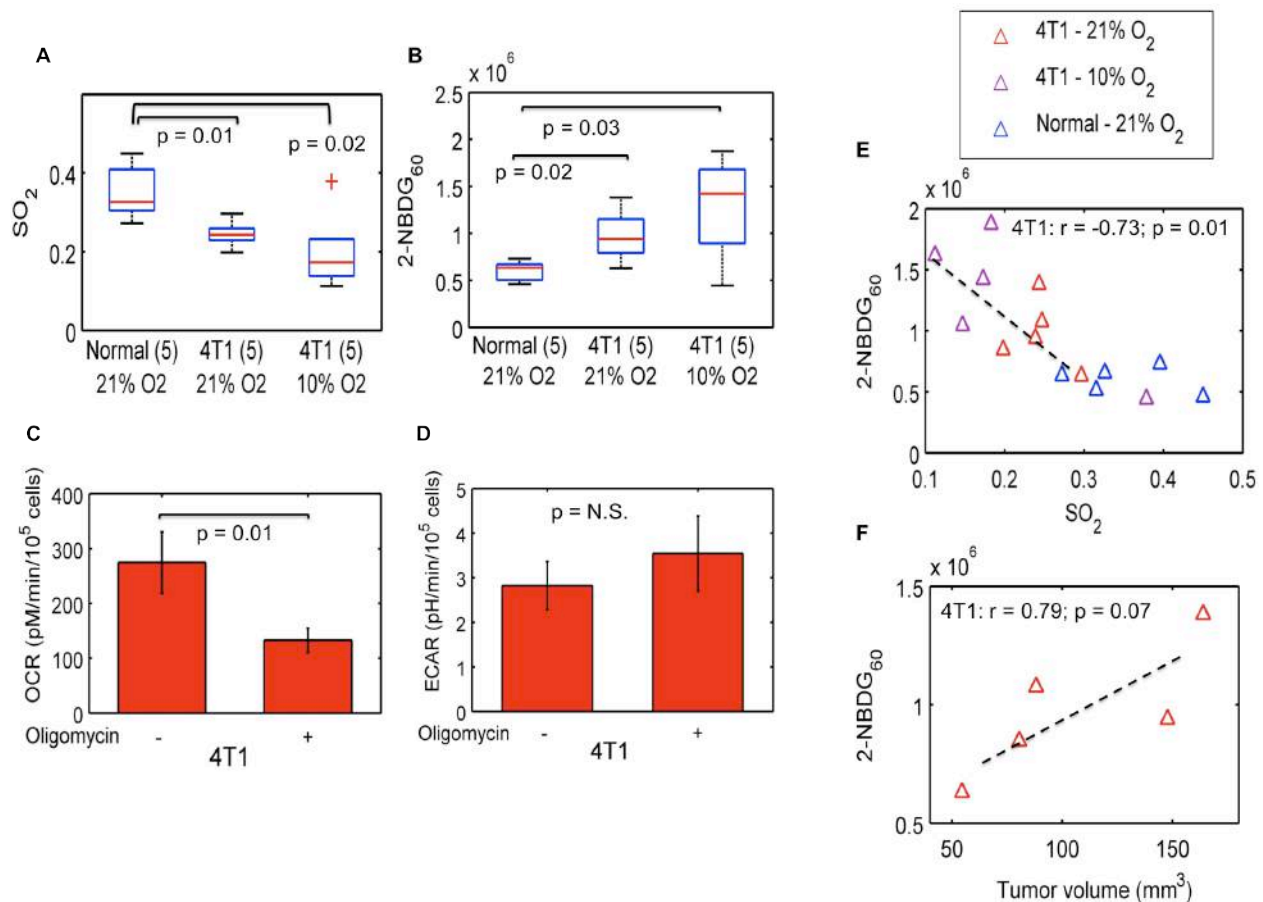


Figure 3.11. Optical spectroscopy reveals differences in glycolytic and vascular characteristics of 4T1 and 4T07 murine mammary tumors. **A.** SO_2 is significantly lower in 4T1 (both normoxia and hypoxia) tumors compared with normal tissue. **B.** $2-NBDG_{60}$ is significantly higher in 4T1 tumors exposed to normoxia and hypoxia compared with normal tissue ($p = 0.02$ and 0.03 , respectively). **C.** Blockade of respiration with oligomycin significantly reduces OCR in the 4T1 cells. **D.** However, there is only a small but insignificant increase in ECAR in response to oligomycin. Data represent $n=12$ cell samples from 3 distinct assays. **E.** $2-NBDG_{60}$ is inversely correlated with SO_2 for the 4T1 tumors that were exposed to 21% O_2 and 10% O_2 ($r = -0.73$; $p = 0.01$). Non-tumor-bearing mice, and 4T1 tumor-bearing mice that were breathing normoxia and hypoxia are shown here. 4T1 tumor-bearing mice were exposed to 10% oxygen (rest nitrogen) prior to $2-NBDG$ injection. **F.** $2-NBDG$ uptake in the 4T1 tumors is positively correlated with tumor volume. Error bars indicate standard error of the mean.

Plans for year 6:

In year 6, we plan to complete the optimization of TMRE as a marker of mitochondrial potential in metastatic (4T1) and non-metastatic (67NR) murine mammary tumor xenografts with dorsal window chamber imaging. We will next move to simultaneous optical spectroscopy of $2-NBDG$ and TMRE in a xenograft model. Our method will then be able to repeatedly measure glucose uptake, vascular oxygenation, and mitochondrial membrane potential *in vivo* in solid tumors.

With our optimized method, we look to monitor tumor response to tamoxifen in parental and tamoxifen-resistant MCF-7 tumors in an orthotopic breast cancer model. Spectroscopy will be repeated over the course of eight weeks to monitor changes in metabolism during treatment. Many studies indicate that glycolysis changes in response to both Akt pathway activation and estrogen stimulation, which may both contribute to tamoxifen resistance. Consistent with previous findings, a study by our group showed that treatment with tamoxifen significantly decreased 2-NBDG uptake by ER+ (tam-sensitive) cells, but not ER- cells, which are not sensitive to tam. We hypothesize that our “optical toolbox” of endogenous contrast, 2-NBDG, and TMRE will be suitable for identifying tamoxifen-resistant tumors during treatment.

4. KEY RESEARCH ACCOMPLISHMENTS:

AIM 1

- The hi-resolution 49-channel instrumentation has been optimized.
 - The light source was upgraded to a multi-channel LED source.
 - The imaging platform has been reduced in size and weight.
- Hi-resolution raster-scanned images were acquired for approximately 60 new lumpectomy patients; the initial 30 have been analyzed and corroborate our previous work.
- The spectral imaging software has been upgraded to provide hi-resolution parameter maps intra-operatively.
- The diagnostic quantitative analysis for the 49 channel patient data set has been developed.

AIM 2

Duke

- Continued to enroll patients in *ex vivo* biopsy study which demonstrates the potential of using HRME imaging to determine histology of samples during a core needle biopsy procedure (n = 71 patients total). We are planning to continue enrolling patients up to n = 75 in year 6.
- Applied sparse decomposition algorithm to all images of biopsy specimens and built initial classification model to distinguish between malignant and benign tissue.
- Currently optimizing our classification model to yield the best separation between positive and negative biopsies.

Rice

- We developed computerized algorithms to segment and quantitatively analyze DCIS lesions and benign ducts observed in confocal fluorescence images.

- Our quantitative analysis of adipocytes' physical characteristics shows that there are significant differences in cell morphology adjacent to neoplastic and non-neoplastic tissue margins.
- In our analysis of confocal images to evaluate CNB specimens, we show that grayscale confocal images have moderate agreement with histologic images on estimated invasive tumor cellularity.

AIM 3

- Demonstrated sensitivity of delivery-corrected glucose uptake to metabolic perturbations
- Demonstrated sensitivity of mitochondrial membrane potential probe to changes in oxygenation
- Optimized optical spectroscopy of vascular oxygen saturation and glucose uptake *in vivo*

5. CONCLUSIONS:

Aim 1

The work described herein details the performance and clinical suitability of an optimized version of our fiber-optic based clinical spectroscopy tool for intra-operative margin assessment. Optical property extraction accuracy using a single reference phantom was found to be less than 10% over the range of tissue optical properties typically seen in clinic and indicated by previous work by our lab[15, 108, 109]. The raster-scanning implementation has dramatically improved the spatial resolution and acquisition reproducibility relative to previous implementations of margin assessment tools developed by our lab. Analysis of the first set of patient data collected with device suggests that sampling resolution could improve the sensitivity and specificity relative to previous generations. In addition to the improved resolution, the raster-scanning imaging platform provides precise pressure control and placement of the probe relative to the specimen. The control of pressure is important in the context of a tool that makes physical contact with the specimen: the applied pressure must not compress the margin as it could result in a false positive. The newly developed LED light source has allowed us sample the margin 8 times over (64 images per margin) due to the reduced time needed to toggle the light source channels. These instrumentation advancements will augment the development of our diagnostic algorithm which can increasingly improve the accuracy in determining the margin landscape, ultimately allowing for the detection of small, easily missed regions of disease.

Aim 2

Duke

The *ex vivo* biopsy study demonstrates that high resolution fluorescence imaging of acriflavine stained tissue combined with an algorithm that leverages sparse decomposition analysis provides a rapid, non-destructive and automated strategy for quantitative pathology of thick

tissues with non-uniform background heterogeneity. During Year 6, we will finalize our diagnostic model to yield the optimal separation between positive and negative biopsies. This includes further identifying why biopsies are being incorrectly classified, and iterating on our model building in order to achieve optimal performance.

Rice

The goal of this proposal was to develop and apply imaging systems and molecular contrast agents which can be used in patients to 1) improve early detection and rapid assessment of breast cancer lesions, 2) aid in selection of targeted therapeutics, and 3) monitor the efficacy of these.

We developed computerized algorithms to segment and quantitatively analyze DCIS lesions and benign ducts observed in confocal fluorescence images. We demonstrated that two parameters, median duct wall width and number of lumens, classify DCIS from benign ducts in confocal fluorescence images with high sensitivity (88.5%) and specificity (92%). These parameters could potentially be used to develop a more objective method to distinguish between neoplastic and non-neoplastic ducts in breast tissue specimens. Our quantitative analysis of adipocytes' physical characteristics shows that there are significant differences in cell morphology adjacent to neoplastic and non-neoplastic tissue margins. We found that adipocyte area and diameter are lower when adjacent to neoplastic lesions than in tissue adjacent to normal collagen. These findings indicate that physical parameters of breast morphology could be used to rapidly assess breast lesions and to monitor disease progression and regression.

In our analysis of confocal images to evaluate CNB specimens, we show that grayscale confocal images have moderate agreement with histologic images on estimated invasive tumor cellularity. We also found that confocal images of CNB specimens could be acquired within an average of less than 2 minutes. Our findings suggest that confocal fluorescence microscopy could potentially be used to assess CNB specimen adequacy in a clinical setting and to indicate the need for a repeat biopsy.

Aim 3

Clinical tools for the measurement of tumor metabolism are invaluable, but current technologies are often expensive or require destructive tissue preparation. We have validated a new technique for monitoring tissue metabolism *in vivo* with high-resolution optical microscopy and repeatable, non-invasive optical spectroscopy. A combination of glucose uptake (2-NBDG), mitochondrial membrane potential (TMRE), and vascular oxygenation (SO₂) reported on tumor and non-tumor phenotype and response to perturbations *in vivo*.

Our findings with high-resolution intravital microscopy show that correcting for 2-NBDG delivery with a correction factor " R_D " helps account for experimental and physiological effects including blood velocity, variations in injected dose, and non-specific uptake. Delivery-corrected glucose uptake gave better separation between a non-metastatic mammary tumor line and a metastatic

mammary tumor line than glucose uptake alone. Further, the addition of a vascular information showed distinct relationships between delivery-corrected glucose uptake and oxygen saturation in the two cell lines, with the metastatic tumor line showed increased demand for glucose, even in the presence of abundant oxygen. With further testing on aggressive and non-aggressive tumor types, our imaging method shows promise as a tool for outcome prediction and therapy planning at the time of diagnosis.

We have also shown that optical spectroscopy is an effective method for simultaneous measurement of 2-NBDG and vascular oxygenation. Optical spectroscopy of 2-NBDG showed an inverse correlation with blood glucose concentration, indicating sensitivity to glucose demand. The strategy was effective for distinguishing non-tumor tissue from aggressive, glycolytic tumors *in vivo*; tumor showed lower oxygenation and higher glucose uptake than non-tumor. The next steps in this project are further validation of TMRE imaging and spectroscopy and combination of 2-NBDG and TMRE monitoring into a single, simultaneous measurement strategy. With our ability to measure metabolic and vascular endpoints, we hypothesize that we will then be able to differentiate tamoxifen resistant tumors from tamoxifen responders. Our future work focuses on determination of therapy response.

6. PUBLICATIONS, ABSTRACTS AND PRESENTATIONS:

AIM 1:

Journal publications – (published, in review and in progress)

1. Nichols, B.S., *A 49-Channel Wide-Field Spectral Imaging System for Quantitative Breast Tumor Margin Assessment*. PLoS one, In preparation.
2. Brown, J.Q., et al., *Optical Spectral Surveillance of Breast Tissue Landscapes for Detection of Residual Disease in Breast Tumor Margins*. PLoS one, 2013. 8(7): p. e69906.

AIM 2:

Journal publications – (published, in review and in progress)

1. Mueller J, Fu H, Mito J, Whitley M, Chitalia R, Dodd L, Willett R, Kirsch D, Ramanujam N. *A rapid microscopic approach toward predicting local recurrence of tumor margins in vivo*. Cancer Research, 2014. In progress.
2. Mueller J, Harmany Z, Mito K, Kennedy S, Kim Y, Dodd L, Geradts J, Kirsch D, Willett R, Brown Q, Ramanujam N. *Quantitative Segmentation of Fluorescence Microscopy Images of Heterogeneous Tissue: Application to the Detection of Residual Disease in Tumor Margins*. PLoS one, 2013, 8(6): e66198.
3. Fu H, Mueller J, Javid M, Mito J, Kirsch D, Ramanujam N, Brown Q. *Optimization of a Widefield Structured Illumination Microscope for Non-Destructive Assessment and Quantification of Nuclear Features in Tumor Margins of a Primary Mouse Model of Sarcoma*. PLoS one, 2013, 8(7): e68868.

4. Dobbs J, Mueller J, Shin D, Krishnamurthy S, Kuerer H, Yang W, Ramanujam N, Richards-Kortum R: *Quantitative Analysis of Breast Duct and Nuclear Features by Segmentation of Images Acquired with Confocal Fluorescence Microscopy*. (In preparation).
5. Dobbs J, Krishnamurthy S, Kyrish M, Benveniste A, Yang W, Richards-Kortum R: *Confocal Fluorescence Microscopy for Rapid Evaluation of Invasive Tumor Cellularity of Inflammatory Breast Carcinoma Core Needle Biopsies*. Breast Cancer Research and Treatment (Under review).
6. Dobbs J, Ding H, Benveniste A, Krishnamurthy S, Kuerer H, Yang W, Richards-Kortum R: *Feasibility of Confocal Fluorescence Microscopy for Real-Time Evaluation of Neoplasia in Fresh Human Breast Tissue*. Journal of Biomedical Optics 18 (10), 106016 (October 28, 2013); doi: 10.1117/1.JBO.18.10.106016

Conference abstracts and proceedings

1. Mueller J, Fu H, Javid M, Kirsch D, Willett R, Brown Q, Ramanujam N. *Structured Illumination Fluorescence Imaging and Analysis for Identification of Residual Disease during Cancer Surgery*. Biomedical Optics (BIOMED) Topical Meeting, Miami, FL, April 2014.
2. Mueller J, Fu H, Mito J, Javid M, Harmany Z, Dodd L, Willett R, Kirsch D, Brown Q, Ramanujam N. *Quantitative high-resolution fluorescence imaging for in vivo detection of residual disease during cancer surgery*. NCI-NIBIB Point of Care Technologies for Cancer Conference, Bethesda, MD, January 2014.
3. Mueller J, Oh A, Brown Q, Ramanujam N, Willett R. *Quantitative Tissue Characterization in Fluorescence Microscopy*. Forty-Seventh Asilomar Conference on Signals, Systems, and Computers. Pacific Grove, CA, November 2013.
4. Mueller J, Harmany Z, Mito K, Kennedy S, Kim Y, Dodd L, Geradts J, Kirsch D, Willett R, Brown Q, Ramanujam N. *Quantitative segmentation of fluorescence microscopy images of heterogeneous tissue: Application to the detection of residual disease in tumor margins*. SPIE Photonics West, San Francisco, CA, February 2013.
5. Mueller J, Harmany Z, Mito K, Kennedy S, Kim Y, Dodd L, Geradts J, Kirsch D, Willett R, Brown Q, Ramanujam N. *Quantitative segmentation of fluorescence microscopy images of heterogeneous tissue: Approach for tuning algorithm parameters*. Biomedical Spectroscopy, Microscopy, and Imaging, SPIE Photonics West Proceedings Vol. 8587, February 2013.
6. Dobbs J, Shin D, Krishnamurthy S, Kuerer H, Yang W, Richards-Kortum R: *Quantification of Adipocyte Area at Invasive Breast Tumor Margins and in Benign Stroma*. Talk: Frontiers in Optics, Optics Society of America, 2014. Oral presentation: October 21, 2014.

AIM 3:

Journal publications – (published, in review and in progress)

- 1) Frees, A.E., N. Rajaram, S.S. McCachren III, A.N. Fontanella, M.W. Dewhirst, and N. Ramanujam. "Delivery-corrected imaging of fluorescently-labeled glucose reveals distinct breast cancer phenotypes." Submitted to PLOS ONE 10/2014.

- 2) Rajaram, N., A. Reesor, C. Mulvey, A.E. Frees, and N. Ramanujam. "Non-invasive, simultaneous quantification of vascular oxygenation and glucose uptake in tissue." Submitted to PLOS ONE 9/2014.

Conference abstracts and proceedings

- 1) Frees, A.E., N. Rajaram, S.S. McCachren, A. Vaz, M.W. Dewhirst, and N. Ramanujam. "Optical monitoring of glucose demand and vascular delivery in a preclinical murine model." Proc. SPIE 8947, Imaging, Manipulation, and Analysis of Biomolecules, Cells, and Tissues XII, 894705 (2014).

7. PATENTS

IP	Status	Owners
System and methods for spectral analysis of a tissue using an instrument, optical probe and MC algorithm	PCT and US (granted)	Duke
DRS device for quantifying tissue absorption and scattering	PCT and US (application submitted)	Duke and WARF
Imaging platform	US (IDF submitted)	Duke

8. REPORTABLE OUTCOMES

- 1) Aim 1 - Design, fabrication and validation of hi-resolution wide-field optical spectroscopy system and software platform
- 2) Aim 2 – Built a diagnostic model to classify acriflavine stained biopsies imaged with high resolution fluorescence microscopy as either malignant or benign.
- 3) Aim 3 – Delivery corrected, optical imaging and spectroscopy of 2-NBDG and vascular oxygenation

9. OTHER ACHIEVEMENTS

Nothing to report

10. REFERENCES:

1. Jacobs, L., *Positive margins: the challenge continues for breast surgeons*. Ann Surgical Oncology, 2008. **15**(5): p. 1271-2.
2. Lee, M.C., et al., *Determinants of breast conservation rates: reasons for mastectomy at a comprehensive cancer center*. Breast J, 2009. **15**(1): p. 34-40.
3. Society, A.C. *Cancer Facts and Figures 2009*. 2009.

4. Sanchez, C., et al., *Factors associated with re-excision in patients with early-stage breast cancer treated with breast conservation therapy*. Am Surg, 2010. **76**(3): p. 331-4.
5. Mann, R.M., et al., *The impact of preoperative breast MRI on the re-excision rate in invasive lobular carcinoma of the breast*. Breast Cancer Res Treat, 2010. **119**(2): p. 415-22.
6. Balch, G.C., et al., *Accuracy of intraoperative gross examination of surgical margin status in women undergoing partial mastectomy for breast malignancy*. Am Surg, 2005. **71**(1): p. 22-7; discussion 27-8.
7. Mendez, J.E., et al., *Influence of breast cancer margin assessment method on the rates of positive margins and residual carcinoma*. Am J Surg, 2006. **192**(4): p. 538-40.
8. Huston, T.L., et al., *The influence of additional surgical margins on the total specimen volume excised and the reoperative rate after breast-conserving surgery*. Am J Surg, 2006. **192**(4): p. 509-12.
9. Kobbermann, A., et al., *Impact of Routine Cavity Shave Margins on Breast Cancer Re-excision Rates*. Ann Surg Oncol, 2010.
10. McCahill, L.E., et al., *Variability in reexcision following breast conservation surgery*. JAMA, 2012. **307**(5): p. 467-75.
11. Bender, J.E., et al., *A robust Monte Carlo model for the extraction of biological absorption and scattering in vivo*. IEEE Trans Biomed Eng, 2009. **56**(4): p. 960-8.
12. Palmer, G.M. and N. Ramanujam, *A Monte Carlo-based inverse model for calculating tissue optical properties. Part I: Theory and validation on synthetic phantoms*. Appl. Opt., 2006. **45**(5): p. 1062-71.
13. Palmer, G.M., et al., *A Monte Carlo-based inverse model for calculating tissue optical properties. Part II: Application to breast cancer diagnosis*. Appl. Opt., 2006. **45**(5): p. 1072-8.
14. Kennedy, S.A., et al., *Optical breast cancer margin assessment: an observational study of the effects of tissue heterogeneity on optical contrast*. breast Cancer Research, 2010. **12**(6).
15. Brown, J.Q., et al., *Optical Spectral Surveillance of Breast Tissue Landscapes for Detection of Residual Disease in Breast Tumor Margins*. PloS one, 2013. **8**(7): p. e69906.
16. Brown, J.Q., *Optical Assessment of Tumor Resection Margins in the Breast*. IEEE Journal of selected topics in Quantum Electronics, 2010. **16**(3): p. 530-544.
17. Gareau, D.S., et al., *Rapid screening of cancer margins in tissue with multimodal confocal microscopy*. J Surg Res, 2012. **178**(2): p. 533-538.
18. Drezek, R.A., et al., *Optical imaging of the cervix*. Cancer, 2003. **98**: p. 2015-27.
19. Muldoon, T.J., et al., *Evaluation of quantitative image analysis criteria for the high-resolution microendoscopic detection of neoplasia in Barrett's esophagus*. J Biomed Opt, 2010. **15**: p. 026027.
20. Balu, M., et al., *Distinguishing between benign and malignant melanocytic nevi by in vivo multiphoton microscopy*. Cancer Res, 2014. **74**(10): p. 2688-97.
21. Schlichenmeyer, T.C., et al., *Video-rate structured illumination microscopy for high-throughput imaging of large tissue areas*. Biomed Opt Express, 2014. **5**(2): p. 366-77.
22. Tanbakuchi, A.A., et al., *Clinical confocal microlaparoscope for real-time in vivo optical biopsies*. J Biomed Opt, 2009. **14**: p. 044030.
23. Tanbakuchi, A.A., et al., *In vivo imaging of ovarian tissue using a novel confocal microlaparoscope*. Am J Obstet Gynecol, 2010. **202**(1): p. 90.e1-9.
24. Dobbs, J.L., et al., *Feasibility of confocal fluorescence microscopy for real-time evaluation of neoplasia in fresh human breast tissue*. J Biomed Opt, 2013. **18**(10): p. 106016.

25. Clark, A.L., et al., *Confocal microscopy for real-time detection of oral cavity neoplasia*. Clin Cancer Res, 2003. **9**: p. 4714-21.
26. Karen, J.K., et al., *Detection of basal cell carcinomas in Mohs excisions with fluorescence confocal mosaicing microscopy*. Br J Dermatol, 2009. **160**: p. 1242-50.
27. Boppart, S.A., et al., *Optical coherence tomography: feasibility for basic research and image-guided surgery of breast cancer*. Breast Cancer Res Treat, 2004. **84**(2): p. 85-97.
28. Sun, J.G., et al., *Segmentation and correlation of optical coherence tomography and x-ray images for breast cancer diagnostics*. J Innov Opt Health Sci, 2013. **6**(2): p. 1350015.
29. Nguyen, F.T., et al., *Intraoperative evaluation of breast tumor margins with optical coherence tomography*. Cancer Res, 2009. **69**: p. 8790-6.
30. Hsiung, P.L., et al., *Benign and malignant lesions in the human breast depicted with ultrahigh resolution and three-dimensional optical coherence tomography*. Radiology, 2007. **244**(3): p. 865-74.
31. Zysk, A.M., et al., *Optical coherence tomography: a review of clinical development from bench to bedside*. J Biomed Opt, 2007. **12**(5): p. 051403.
32. Clark, A.L., et al., *Detection and diagnosis of oral neoplasia with an optical coherence microscope*. J Biomed Opt, 2004. **9**: p. 1271-80.
33. Mueller, J.L., et al., *Quantitative Segmentation of Fluorescence Microscopy Images of Heterogeneous Tissue: Application to the Detection of Residual Disease in Tumor Margins*. PLoS One, 2013. **8**(6): p. e66198.
34. Kirsch, D.G., et al., *A spatially and temporally restricted mouse model of soft tissue sarcoma*. Nat Med, 2007. **13**: p. 992-7.
35. Mito, J.K., et al., *Oncogene-dependent control of miRNA biogenesis and metastatic progression in a model of undifferentiated pleomorphic sarcoma*. J Pathol, 2013. **229**(1): p. 132-40.
36. Muldoon, T.J., et al., *Subcellular-resolution molecular imaging within living tissue by fiber microendoscopy*. Opt Express, 2007. **15**: p. 16413-23.
37. Ferguson, L.R. and W.A. Denny, *The genetic toxicology of acridines*. Mutat Res, 1991. **258**: p. 123-60.
38. Krolenko, S.A., et al., *Acridine orange accumulation in acid organelles of normal and vacuolated frog skeletal muscle fibres*. Cell Biol Int, 2006. **30**(11): p. 933-9.
39. Candès, E.J. and D.L. Donoho, *New tight frames of curvelets and optimal representations of objects with piecewise C2 singularities*. Communications on Pure and Applied Mathematics, 2004. **57**: p. 219-266.
40. Ballard, D., *Generalizing the Hough Transform to Detect Arbitrary Shapes*. 1981, Pattern Recognition. p. 111-122.
41. Cohen, C., *Image cytometric analysis in pathology*. Hum Pathol, 1996. **27**: p. 482-93.
42. Millot, C. and J. Dufer, *Clinical applications of image cytometry to human tumour analysis*. Histol Histopathol, 2000. **15**: p. 1185-200.
43. Jemal, A., et al., *Global Cancer Statistics*. Ca-a Cancer Journal for Clinicians, 2011. **61**(2): p. 69-90.
44. Siegel, R., D. Naishadham, and A. Jemal, *Cancer Statistics, 2012*. Ca-a Cancer Journal for Clinicians, 2012. **62**(1): p. 10-29.
45. DeSantis, C., et al., *Breast cancer statistics, 2011*. Ca-a Cancer Journal for Clinicians, 2011. **61**(6): p. 409-418.
46. Kaufman, C.S., et al., *Intraoperative ultrasound facilitates surgery for early breast cancer*. Annals of Surgical Oncology, 2002. **9**(10): p. 988-993.
47. Kuhl, C.K., et al., *Mammography, breast ultrasound, and magnetic resonance imaging for surveillance of women at high familial risk for breast cancer*. J Clin Oncol, 2005. **23**(33): p. 8469-76.

48. Ngo, C., et al., *Intraoperative ultrasound localization of nonpalpable breast cancers*. Annals of Surgical Oncology, 2007. **14**(9): p. 2485-2489.
49. Sarvazyan, A., et al., *Cost-effective screening for breast cancer worldwide: current state and future directions*. Breast Cancer (Auckl), 2008. **1**: p. 91-9.
50. Warner, E., et al., *Comparison of breast magnetic resonance imaging, mammography, and ultrasound for surveillance of women at high risk for hereditary breast cancer*. J Clin Oncol, 2001. **19**(15): p. 3524-31.
51. Warner, E., et al., *Surveillance of BRCA1 and BRCA2 mutation carriers with magnetic resonance imaging, ultrasound, mammography, and clinical breast examination*. JAMA, 2004. **292**(11): p. 1317-25.
52. Bobo, J.K., N.C. Lee, and S.F. Thames, *Findings from 752,081 clinical breast examinations reported to a national screening program from 1995 through 1998*. J Natl Cancer Inst, 2000. **92**(12): p. 971-6.
53. Cerussi, A., et al., *In vivo absorption, scattering, and physiologic properties of 58 malignant breast tumors determined by broadband diffuse optical spectroscopy*. Journal of Biomedical Optics, 2006. **11**(4).
54. Muldoon, T.J., et al., *Subcellular-resolution molecular imaging within living tissue by fiber microendoscopy*. Opt Express, 2007. **15**(25): p. 16413-23.
55. Rosbach, K.J., et al., *High-resolution fiber optic microscopy with fluorescent contrast enhancement for the identification of axillary lymph node metastases in breast cancer: a pilot study*. Biomed Opt Express, 2010. **1**(3): p. 911-922.
56. Tanamai, W., et al., *Diffuse optical spectroscopy measurements of healing in breast tissue after core biopsy: case study*. Journal of Biomedical Optics, 2009. **14**(1).
57. Jain, M., et al., *Modified full-field optical coherence tomography: A novel tool for rapid histology of tissues*. Journal of pathology informatics, 2011. **2**: p. 28.
58. McLaughlin, R.A., et al., *Imaging of Human Lymph Nodes Using Optical Coherence Tomography: Potential for Staging Cancer*. Cancer Research, 2010. **70**(7): p. 2579-2584.
59. Nguyen, F.T., et al., *Intraoperative Evaluation of Breast Tumor Margins with Optical Coherence Tomography*. Cancer Research, 2009. **69**(22): p. 8790-8796.
60. Nguyen, F.T., et al., *Optical Coherence Tomography The Intraoperative Assessment of Lymph Nodes in Breast Cancer*. IEEE Engineering in Medicine and Biology Magazine, 2010. **29**(2): p. 63-70.
61. Parrish, A., et al., *Reflectance confocal microscopy for characterization of mammary ductal structures and development of neoplasia in genetically engineered mouse models of breast cancer*. Journal of Biomedical Optics, 2005. **10**(5).
62. Schiffhauer, L.M., et al., *Confocal Microscopy of Unfixed Breast Needle Core Biopsies: A Comparison to Fixed and Stained Sections*. BMC Cancer, 2009. **9**.
63. Tilli, M.T., et al., *Real-time imaging and characterization of human breast tissue by reflectance confocal microscopy*. Journal of biomedical optics, 2007. **12**(5): p. 051901.
64. Muldoon, T.J., et al., *High-resolution imaging in Barrett's esophagus: a novel, low-cost endoscopic microscope*. Gastrointestinal Endoscopy, 2008. **68**(4): p. 737-744.
65. Nitin, N., et al., *Optical molecular imaging of epidermal growth factor receptor expression to improve detection of oral neoplasia*. Neoplasia, 2009. **11**(6): p. 542-51.
66. Allred, D.C., et al., *Ductal carcinoma in situ and the emergence of diversity during breast cancer evolution*. Clin Cancer Res, 2008. **14**(2): p. 370-8.
67. Anderson, N.H., et al., *Computerized scene segmentation for the discrimination of architectural features in ductal proliferative lesions of the breast*. J Pathol, 1997. **181**(4): p. 374-80.
68. Campo-Ruiz, V., et al., *Evaluation of hepatic histology by near-infrared confocal microscopy: A pilot study*. Human Pathology, 2002. **33**(10): p. 975-982.

69. Pierce, M., D. Yu, and R. Richards-Kortum, *High-resolution fiber-optic microendoscopy for in situ cellular imaging*. J Vis Exp, 2011(47).
70. Tan, J., et al., *Adipocyte is a non-trivial, dynamic partner of breast cancer cells*. International Journal of Developmental Biology, 2011. **55**(7-9): p. 851-859.
71. Basset, P., et al., *A novel metalloproteinase gene specifically expressed in stromal cells of breast carcinomas*. Nature, 1990. **348**(6303): p. 699-704.
72. Jodele, S., et al., *Modifying the soil to affect the seed: role of stromal-derived matrix metalloproteinases in cancer progression*. Cancer Metastasis Rev, 2006. **25**(1): p. 35-43.
73. Wiseman, B.S. and Z. Werb, *Stromal effects on mammary gland development and breast cancer*. Science, 2002. **296**(5570): p. 1046-9.
74. Yamauchi, H., et al., *Inflammatory breast cancer: what we know and what we need to learn*. Oncologist, 2012. **17**(7): p. 891-9.
75. Shah, V.I., et al., *False-negative core needle biopsies of the breast: an analysis of clinical, radiologic, and pathologic findings in 27 consecutive cases of missed breast cancer*. Cancer, 2003. **97**(8): p. 1824-31.
76. Gareau, D.S., *Feasibility of digitally stained multimodal confocal mosaics to simulate histopathology*. Journal of Biomedical Optics, 2009. **14**(3).
77. Landis, J.R. and G.G. Koch, *The measurement of observer agreement for categorical data*. Biometrics, 1977. **33**(1): p. 159-74.
78. Bild, A.H., et al., *Oncogenic pathway signatures in human cancers as a guide to targeted therapies*. Nature, 2006. **439**(7074): p. 353-7.
79. Bild, A.H., A. Potti, and J.R. Nevins, *Linking oncogenic pathways with therapeutic opportunities*. Nat Rev Cancer, 2006. **6**(9): p. 735-41.
80. Vivanco, I. and C.L. Sawyers, *The phosphatidylinositol 3-Kinase AKT pathway in human cancer*. Nat Rev Cancer, 2002. **2**(7): p. 489-501.
81. Maira, S.M., et al., *Identification and characterization of NVP-BEZ235, a new orally available dual phosphatidylinositol 3-kinase/mammalian target of rapamycin inhibitor with potent in vivo antitumor activity*. Mol Cancer Ther, 2008. **7**(7): p. 1851-63.
82. Yuan, T.L. and L.C. Cantley, *PI3K pathway alterations in cancer: variations on a theme*. Oncogene, 2008. **27**(41): p. 5497-510.
83. Ohwada, J., et al., *Discovery and biological activity of a novel class I PI3K inhibitor, CH5132799*. Bioorganic & medicinal chemistry letters, 2011. **21**(6): p. 1767-1772.
84. Schnell, C.R., et al., *Effects of the dual phosphatidylinositol 3-kinase/mammalian target of rapamycin inhibitor NVP-BEZ235 on the tumor vasculature: implications for clinical imaging*. Cancer Res, 2008. **68**(16): p. 6598-607.
85. Pries, A.R., et al., *The shunt problem: control of functional shunting in normal and tumour vasculature*. Nature Reviews Cancer, 2010. **10**(8): p. 587-593.
86. Manka, D., Z. Spicer, and D.E. Millhorn, *Bcl-2/adenovirus E1B 19 kDa interacting protein-3 knockdown enables growth of breast cancer metastases in the lung, liver, and bone*. Cancer Res, 2005. **65**(24): p. 11689-93.
87. Maher, J.C., et al., *Hypoxia-inducible factor-1 confers resistance to the glycolytic inhibitor 2-deoxy-D-glucose*. Molecular Cancer Therapeutics, 2007. **6**(2): p. 732-741.
88. Palmer, G.M., et al., *In vivo optical molecular imaging and analysis in mice using dorsal window chamber models applied to hypoxia, vasculature and fluorescent reporters*. Nat Protoc, 2011. **6**(9): p. 1355-66.
89. Gill, E.M., et al., *Relationship between collagen autofluorescence of the human cervix and menopausal status*. Photochemistry and Photobiology, 2003. **77**(6): p. 653-658.
90. Rajaram, N., et al., *Delivery rate affects uptake of a fluorescent glucose analog in murine metastatic breast cancer*. PLoS One, 2013. **8**(10): p. e76524.

91. Fontanella, A.N., et al., *Quantitative mapping of hemodynamics in the lung, brain, and dorsal window chamber-grown tumors using a novel, automated algorithm*. Microcirculation, 2013. **20**(8): p. 724-35.
92. Vaupel, P.W. and D.K. Kelleher, *Pathophysiological and vascular characteristics of tumours and their importance for hyperthermia: heterogeneity is the key issue*. Int J Hyperthermia, 2010. **26**(3): p. 211-23.
93. Goel, S., et al., *Normalization of the vasculature for treatment of cancer and other diseases*. Physiol Rev, 2011. **91**(3): p. 1071-121.
94. Frezza, C., et al., *Metabolic Profiling of Hypoxic Cells Revealed a Catabolic Signature Required for Cell Survival*. Plos One, 2011. **6**(9).
95. Palmer, G.M. and N. Ramanujam, *Monte Carlo-based inverse model for calculating tissue optical properties. Part I: Theory and validation on synthetic phantoms*. Applied optics, 2006. **45**(5): p. 1062-1071.
96. Palmer, G.M. and N. Ramanujam, *Monte-Carlo-based model for the extraction of intrinsic fluorescence from turbid media*. Journal of biomedical optics, 2008. **13**(2): p. 024017-024017-9.
97. Vishwanath, K., et al., *Quantitative optical spectroscopy can identify long-term local tumor control in irradiated murine head and neck xenografts*. J Biomed Opt, 2009. **14**(5): p. 054051.
98. Vishwanath, K., et al., *Using Optical Spectroscopy to Longitudinally Monitor Physiological Changes within Solid Tumors*. Neoplasia, 2009. **11**(9): p. 889-900.
99. Rajaram, N., et al., *Pilot Clinical Study for Quantitative Spectral Diagnosis of Non-Melanoma Skin Cancer*. Lasers in Surgery and Medicine, 2010. **42**(10): p. 716-727.
100. Brown, J.Q., et al., *Quantitative optical spectroscopy: a robust tool for direct measurement of breast cancer vascular oxygenation and total hemoglobin content in vivo*. Cancer research, 2009. **69**(7): p. 2919-2926.
101. Lim, L., et al., *Probe pressure effects on human skin diffuse reflectance and fluorescence spectroscopy measurements*. Journal of Biomedical Optics, 2011. **16**(1).
102. Palmer, G.M., et al., *Optical imaging of tumor hypoxia dynamics*. J Biomed Opt, 2010. **15**(6): p. 066021.
103. Liu, C., et al., *Experimental validation of an inverse fluorescence Monte Carlo model to extract concentrations of metabolically relevant fluorophores from turbid phantoms and a murine tumor model*. Journal of Biomedical Optics, 2012. **17**(7): p. 77012.
104. Heppner, G.H., F.R. Miller, and P.V.M. Shekhar, *Nontransgenic models of breast cancer*. Breast Cancer Res, 2000. **2**(5): p. 331-334.
105. Lu, X., et al., *Metabolomic changes accompanying transformation and acquisition of metastatic potential in a syngeneic mouse mammary tumor model*. Journal of Biological Chemistry, 2010. **285**(13): p. 9317.
106. Bydlon, T.M., et al., *Performance metrics of an optical spectral imaging system for intra-operative assessment of breast tumor margins*. Optics express, 2010. **18**(8): p. 8058-8076.
107. Yu, B., H.L. Fu, and N. Ramanujam, *Instrument independent diffuse reflectance spectroscopy*. Journal of Biomedical Optics, 2011. **16**(1): p. 011010-011010-12.
108. Brown, J., et al., *Optical assessment of tumor resection margins in the breast*. IEEE Journal on Selected Topics in Quantum Electronics, 2010(): p. accepted.
109. Bydlon, T.M., et al., *Performance metrics of an optical spectral imaging system for intra-operative assessment of breast tumor margins*. Opt. Express, 2010. **18**(8): p. 8058-8076.